On Computed Tomography in Talbot-Lau X-Ray Interferometry

Master's Thesis in Advanced Optical Technologies

Presented by
Florian Schiffers
13.06.2017

Erlangen Centre for Astroparticle Physics
and
Pattern Recognition Lab

Friedrich-Alexander-Universität Erlangen-Nürnberg

Supervisor
Prof. Dr. Gisela Anton
Dr.-Ing. Christian Riess
Sebastian Käppler M. Sc.

Statutory Declaration

I confirm that I have written this thesis without any external help and not using sources other than those I have listed in the thesis. I confirm also that this thesis or a similar version of it has not been submitted to any other examination board and has not been previously accepted as part of a exam for a qualification. Each direct quotation or paraphrase of an author is clearly referenced.

Erlangen, 13th June, 2017

Eidesstattliche Erklärung

Ich versichere, dass ich die Arbeit ohne fremde Hilfe und ohne Benutzung anderer als der angegebenen Quellen angefertigt habe und dass die Arbeit in gleicher oder ähnlicher Form noch keiner anderen Prüfungsbehörde vorgelegen hat und von dieser als Teil einer Prüfungsleistung angenommen wurde. Alle Ausführungen, die wörtlich oder sinngemä übernommen wurden, sind also solche gekennzeichnet.

Erlangen, 13.06.2017

Florian Schiffers

Abstract

Talbot-Lau X-ray grating interferometry applied within a polychromatic setup suffers from additional artifacts compared to conventional attenuation imaging. Among those are beam hardening and dispersion effects due to the complex coupling of different physical effects involved in the image formation process. In computed tomography these effects lead to image degradation, such as cupping and streak artifacts, hampering diagnostic use.

This thesis seeks to reduce these artifacts in an iterative reconstruction framework. To this purpose, we define a model of the polychromatic forward projection that includes prior knowledge about the physical setup. Using this model we derive a maximum likelihood algorithm for simultaneous reconstruction of the attenuation, phase and scatter images.

In our experiments on a synthetic ground-truth phantom, we compare filtered back projection reconstruction with the proposed approach. The proposed method considerably reduces strong beam hardening artifacts in the phase images, and almost completely removes these artifacts in the absorption and scatter images. Reconstruction with real data has not been successful because the proposed model does not reproduce the measured reality. Further research is required to resolve this discrepancy.

Furthermore, an optimized iterative reconstruction algorithm for grating based tomography is proposed. Last, an in-depth analysis of an iterative reconstruction framework for Talbot-Lau imaging data is provided.

Contents

1 Introduction 3

2 Physical fundamentals 7
- 2.1 Generation of X-rays . . . 7
- 2.2 Interactions of X-rays with Matter . . . 9
- 2.3 Propagation of X-rays . . . 12

3 Grating Based X-Ray Imaging 15
- 3.1 Talbot-Effect . . . 15
- 3.2 Lau-Effect . . . 16
- 3.3 Talbot-Lau Interferometer . . . 17
- 3.4 Image Modalities . . . 18

4 Computed Tomography 23
- 4.1 Analytic Reconstruction . . . 24
- 4.2 Iterative Reconstruction . . . 26
- 4.3 Gradient Reconstruction . . . 27
- 4.4 Statistical Reconstruction . . . 28
- 4.5 X-ray Grating-Based Tomography . . . 30

5 Reconstruction Framework 39
- 5.1 Design Considerations . . . 39
- 5.2 Implementation of Forward- and Back Projector . . . 40
- 5.3 Kaiser-Bessel Functions . . . 41
- 5.4 Implementation of the System Matrix . . . 44
- 5.5 Choice of Parameters . . . 45

6 Methods 47
- 6.1 Reference Measurement . . . 47
- 6.2 Estimation of X-ray Center of Rotation . . . 48
- 6.3 Error Metrics . . . 51

7 Materials 53
- 7.1 Setup Parameters . . . 53
- 7.2 Specimen . . . 54
- 7.3 Wave Propagation Simulation . . . 55

7.4 Phantom Data using Forward Model 57

8 Contributions 61

8.1 State-of-the-Art 61
8.2 Polychromatic Forward-Projection and Reconstruction 63
8.3 Second Derivative 70

9 Experiments and Results 75

9.1 Case Studies 75
9.2 Reconstruction Properties 80
9.3 Reconstruction with Second Derivative 87
9.4 Polychromatic Reconstruction 88

10 Conclusion and Outlook 97

List of Figures 99

Chapter 1

Introduction

Over the last decades, a great effort was made to understand imaging modalities exploiting the wave properties of X-rays [70, 121, 131]. Among those is Talbot-Lau grating-based phase-contrast X-ray imaging, which allows for simultaneous measurement of attenuation, the phase shift that occurs while traversing the material, and the specimen's small-angle scattering properties. Beneficial contrast for medical application was reported for the differential phase-contrast signal when differences in soft-tissue are of importance [28, 98]. Additionally, the dark-field contrast introduced by Pfeiffer *et al.* [83] yields complementary information if the specimen provides highly varying structures on the subpixel scale, such as lung tissue [7, 110] or porous media like calcifications in mammography [65, 112]. The technique offers great prospects for future clinical applications, since the setup has proven to work well when embedded in a conventional X-ray attenuation setup [84, 107]. Figure 1.1 exemplary shows Talbot-Lau images of a human hand measured at ECAP [42]. Here, soft tissue structures such as quadriceps tendon, patellar ligament or muscle fibers are better visible than in the attenuation image. Tomographic reconstructions of an ex-vivo mouse sample are shown for the attenuation and scatter image in Fig. 1.2. On the one hand, the attenuation image provides good contrast between soft tissue and bone. On the other hand, the scatter image is sensitive to small-angle scattering and thus delivers complementary image information. Indeed, the scatter image shows a clear image of the lungs, whereas this is not visible in the attenuation image.

However, tomographic reconstructions of data from a polychromatic setup suffer from artifacts due to two energy-dependent factors. The first factor are the energy-dependent material coefficients [14, 23, 80, 126], an issue which is the analog to conventional attenuation X-ray imaging. For attenuation X-ray imaging, this is a long-standing, much-researched problem [41, 5, 62]. The second factor, that is specific to Talbot-Lau interferometers, is the energy-dependence of the interferometer visibility. This leads to beam hardening and dispersion effects in both phase [23, 14] and dark-field signals [50, 80]. We propose an iterative tomographic reconstruction which addresses both factors in the proposed method to reduce polychromatic artifacts.

Bevins *et al.* and Chabior *et al.* presented first experimental evidence of beam hardening in phase-contrast tomography [14, 23]. Chabior *et al.* and Koehler *et al.* adapted linearization techniques known from conventional CT [52] to Talbot-Lau imaging [23, 54], but performed no evaluation on tomographic data. We are unaware of any beam-hardening correction that is specifically tailored to Talbot-Lau interferometers.

For tomographic reconstruction of Talbot-Lau data, Brendel *et al.* and Ritter *et al.* investigated a maximum-likelihood algorithm to simultaneously reconstruct attenuation, phase and scatter images without requiring phase retrieval [92, 19, 94]. However, this method can not cope with polychromatic data, because

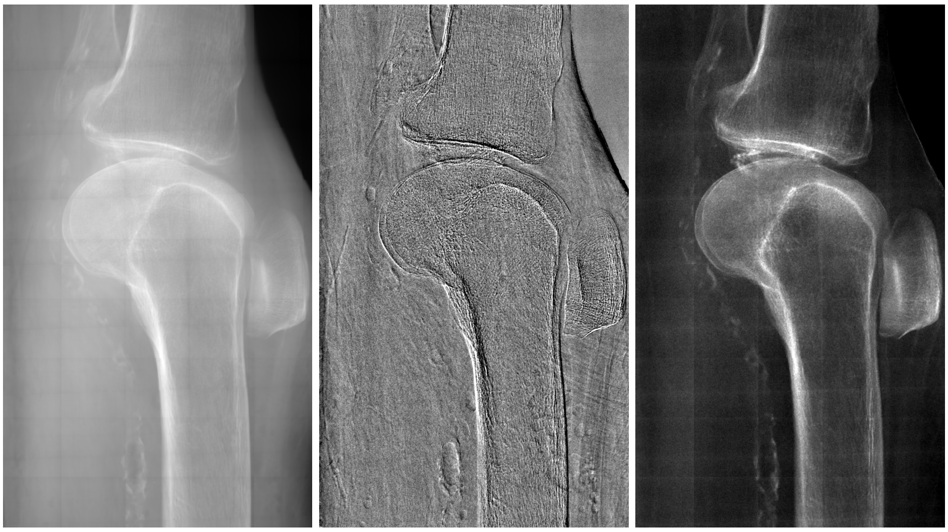

(a) Attenuation (b) Differential phase (c) Dark-Field

Figure 1.1: Example images of Grating Based X-Ray inteferometry measured by Horn *et a.l* [42].

a monochromatic source was used to model the forward projection.

Our key contribution is to extend the monochromatic forward model [94, 19] to polychromatic data. The main benefit of the extended model is that beam-hardening artifacts are implicitly dampened or even completely removed. We show how prior knowledge can be used to approximate the energy dependence of materials. Furthermore, we use this model to propose an iterative reconstruction algorithm for polychromatic CT based on maximum-likelihood techniques [29]. To our knowledge, this is the first work that addresses polychromaticity-induced artifacts in an iterative reconstruction framework for Talbot-Lau tomography.

We first validate the reconstruction algorithm with synthetic projection data of a well-defined phantom. The data reconstructed by the proposed algorithm are compared to results obtained through standard filtered back projection techniques, achieving a considerable reduction of beam-hardening artifacts. Subsequently, the polychromatic reconstruction is applied on Talbot-Lau data where polychromaticity-induced artifacts are observed. However, it turns out that the proposed algorithm can not fully model the physical reality and requires further adjustment. Thus, polychromatic artifacts, particularly in the scatter image, are not removed or dampened.

Contribution

The main contributions of this thesis are

- Development of an easy-to-use and fast X-ray grating-based tomographic reconstruction framework (written in Java)
- Development of a framework (written in Matlab) for preprocessing of tomographic Talbot-Lau data
- Derivation and implementation of a method to cope with data corrupted by polychromatic artifacts
- Derivation and implementation of an optimization algorithms to improve the convergence speed of the reconstruction algorithm

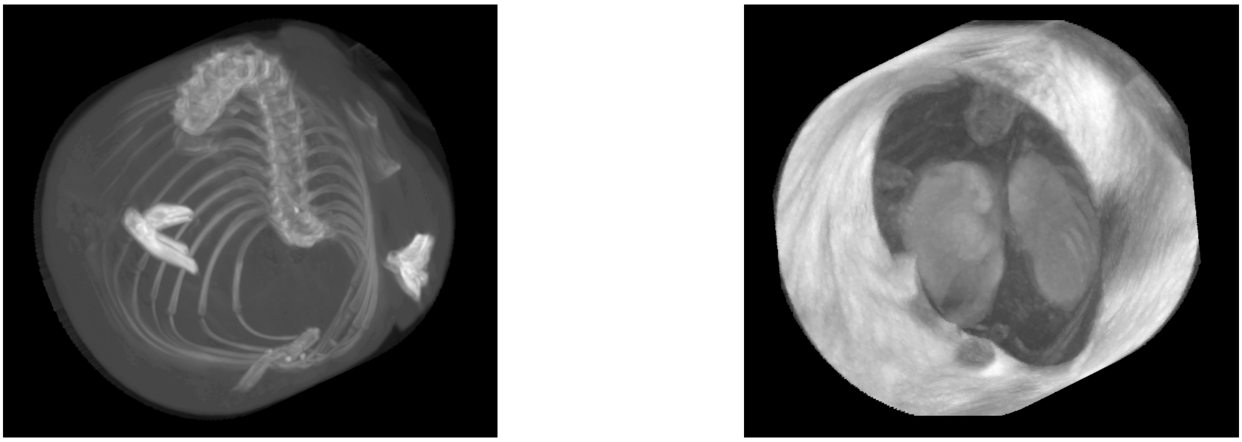

(a) Attenuation CT

(b) Scatter CT

Figure 1.2: Ex-vivo Talbot-Lau tomography of a mouse. The lungs are not seen in the attenuation CT. In the tomographic reconstruction of the dark-field image, the lungs are clearly visible.

- Thorough analysis of simultaneous grating-based reconstruction in respect to dominant setup parameters like noise, visibility of the interferometer, and number of phase-steps
- Planning and conduction of tomographic measurements at ECAP in order to evaluate the proposed algorithms

Outline

This thesis is structured in the following way. Chapter 2 introduces the central theoretical concepts. These include the generation of X-rays, basic interactions of X-rays with matter and their propagation. After that, chapter 3 reviews the principles of grating-based phase-contrast imaging, followed by an introduction to computed tomography in chapter 4. Here, we discuss the analytic and iterative reconstruction techniques for conventional tomography, and how these methods are adapted for Talbot-Lau tomography. An important aspect will be the presentation of an algorithm for simultaneous reconstruction of Talbot-Lau data without prior phase retrieval.

Chapter 5 is dedicated to the reconstruction framework developed in this thesis. First, we discuss general design considerations, then we will present a detailed overview of the implementation employing Kaiser-Bessel functions. An executive summary of the methods and materials used can be found in chapter 6 and 7. We get to the heart of the matter in Chapter 8, which contains the main contributions of this thesis. After reviewing the current state-of-the-art, we propose an iterative reconstruction algorithm to deal with polychromatic Talbot-Lau data. Finally, we derive an enhanced numerical optimization algorithm.

Chapter 9 demonstrates the reconstruction algorithm on typical imaging problems.It starts out with a reconstruction based on the monochromatic model for several case studies, followed by a detailed analysis of the reconstruction properties. The third part deals with the polychromatic forward model, working with simulated data first to prove self-consistency of the algorithm, and only later applying it to real data measurements. The final chapter 10 summarizes the findings of our investigation and offer an outlook for further research.

Chapter 2

Physical fundamentals

The main objective of this chapter is to introduce the fundamental physics required to understand grating-based X-ray imaging. First, the generation of X-rays is discussed. Subsequently, we shortly review the propagation of X-rays. Last, the interaction processes of X-rays with matter are described.

2.1 Generation of X-rays

X-rays were discovered by Wilhelm-Conrad Röntgen in Würzburg in November 1895. He noticed in experimentation with cathode-ray tubes that when enough voltage is applied, a fluorescent screen is lightened even when shielded by other objects [95]. The discovery of this phenomenon was a major breakthrough in physics history and spread around the world in a speed that has barely been seen before [21].

In the following decades X-rays found their way into numerous physical applications, such as crystallography or spectroscopy [113, 1]. However, for the common world, X-rays are undoubtedly best known for its revolutionary impact in the medical sciences [66].

2.1.1 Basics of X-radiation

X-radiation is a form of high frequency electromagnetic radiation. X-rays typically have energies ranging from 100 eV up to 200 keV [20]. Nowadays their main applications are in X-ray crystallography, radiography and medical CT imaging, as well as security scans that use high energy photons above 100 keV [3]. An overview of the electromagnetic spectrum is given in Fig. 2.1.

Their generation is described by several physical processes [21]. For one, deceleration of an electron beam in the atomic field produces electromagnetic waves. This is called bremsstrahlung. Secondly, relaxation processes of an atom excited emit the so-called characteristic radiation.

There are several ways to produce X-radiation. On clinical practice X-rays are mainly generated using X-ray tubes. They emit an ensemble of X-rays at different energies in form of a broad spectrum; see Fig. 2.4. The continuous part is due to bremsstrahlung whereas the characteristic radiation causes the peaks. The following section describes both in more detail.

2.1.2 Bremsstrahlung

Bremsstrahlung is emitted, whenever an electron of kinetic energy E_1 enters the Coulomb-field of an atom nucleus. The electron decelerates due to the inelastic interaction with the Coulomb-field and has then an

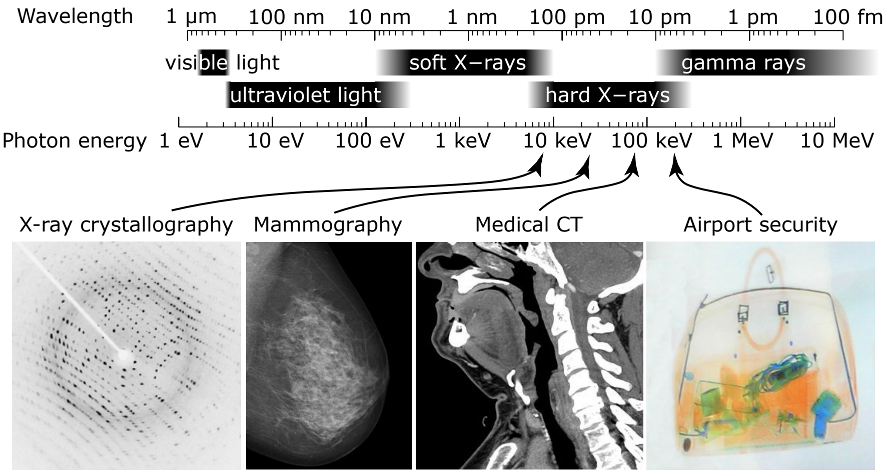
Wavelength
1 μm
100 nm
10 nm
1 nm
100 pm
10 pm
1 pm
100 fm
visible light
soft X−rays
gamma rays
ultraviolet light
hard X−rays
Photon energy
1 eV
10 eV
100 eV
1 keV
10 keV
100 keV
1 MeV
10 MeV
X-ray crystallography
Mammography
Medical CT
Airport security

Figure 2.1: The electromagnetic spectrum with a focus on the X-ray range [119] and corresponding applications indicated.

energy E_2 . The energy loss leads to emission of a photon of energy $E_{ph} = E_1 - E_2 = hf$ [20]. h is Planck's constant and f the photon's frequency. This process is shown in Fig. 2.2.

2.1.3 Characteristic Radiation

Besides bremsstrahlung there is a second possibility of the electron producing X-radiation. It happens when the incoming electron exceeds the binding energy of an orbital electron of the target material. Here the orbital electrons of an inner atomic shell are removed, by, for example, an incoming electron which scatters in the interaction process. The emerging hole is then replaced by an electron of a higher shell. Hereby a photon is released with the energy difference of both orbits. This process is sketched in Fig. 2.3.

According to historic notation, the energy transitions are labeled with the letter of the inner orbit the electron is moving to. The small Greek letters starting with α, β and so on describe the number of orbits the electron is moving. For example, K_α describes the transition where an orbital electron is removed from the K-orbit and the hole is then filled by an electron of the L-orbit. Due to the discrete energy states inside the atoms one observes a discrete X-ray spectrum. This is called characteristic spectrum, because the difference of the energy states inside the atom are characteristic for the target material. This phenomena is also referred to as X-ray fluorescence [9].

2.1.4 X-ray Generating using an X-ray Tube

Three steps are required to produce X-rays by an X-ray tube:

- Generation of electrons
- Acceleration of electrons
- Interaction of electrons with the target material

In early days these steps have been realized e.g. with a an anode and a cathode placed in an evacuated glass tube . Until now X-ray tubes have experienced constant development, but the basic principles of an X-ray tube, schematically shown in Fig. 2.5, have remained the same. Electrons are generated by heating

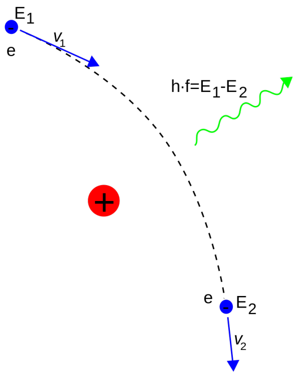

Figure 2.2: An electron decelerates due to the interaction with the Coulomb-field of the atomic nucleus. The energy loss is emitted as a photon, called the bremsstrahlung. From [120].

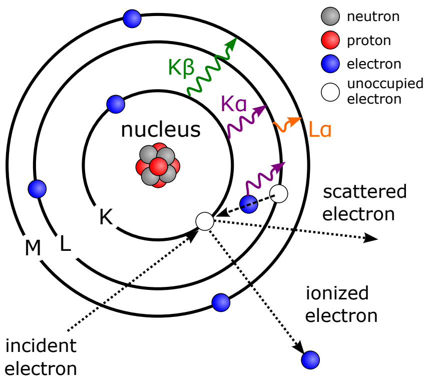

Figure 2.3: An incident electron removes an electron from an inner shell due to a scatter process. Another electron relaxes and emits a photon, called characteristic radiation. From [119].

a filament that emits electrons due to the thermoelectric effect. The electrons are accelerated from the cathode towards a target material. The target material is required to yield a high atomic number. Typically a tungsten anode (stand-alone or as an alloy) is used. When striking the target, electrons interact with matter and photons are produced due to the two effects explained above. However, only about 1 % of the electron's kinetic energy is transformed into radiation. The majority of the energy is discharged in the form of heat. For this reason the whole anode is built as a turning disk, such that more material can be exposed to the electrons and the heat is well distributed around the anode [10].

2.2 Interactions of X-rays with Matter

When electromagnetic waves, such as X-rays, penetrate matter, not only the amplitude of the wave but also the phase is affected [22]. Both can potentially be used as a contrast mechanism for imaging. Unfortunately, while only information on the waves intensity is directly accessible in conventional imaging systems, the phase can only be accessed indirectly using interference effects.

In this section, fundamental principles of phase contrast imaging will be given. Electromagnetic waves interact in a variety of different ways while traversing material. In a microscopic picture these interactions are described in a semi-classical picture by scattering around the atoms due to their electric charge distribution.

The total number of scattered photons per solid angle Ω is given by the differential cross-section $\frac{d\sigma}{d\Omega}$. The scattered signal at a distance R from the point of interested can then be written as

$$\left(\frac{d\sigma}{d\Omega}\right) = \left(\frac{|\mathscr{E}_{out}|}{|\mathscr{E}_{in}|}\right)^2 \cdot R^2 \quad , \tag{2.1}$$

where $\mathscr{E}_{out}$ and $\mathscr{E}_{in}$ denote the outgoing and incoming field, respectively [2]. The incoming photon produces an oscillating electromagnetic field and enforces harmonic oscillations on the shell electrons. These oscillations lead to emission of a spherical electromagnetic wave $\mathscr{E}_{out} \sim e^{ikR}/R$. The ratio between incoming and out-coming field is

$$\frac{|\mathscr{E}_{out}|}{|\mathscr{E}_{in}|} = -r_e \cdot f(\mathbf{q}, E) \cdot P \cdot \frac{e^{ikR}}{R} \quad , \tag{2.2}$$

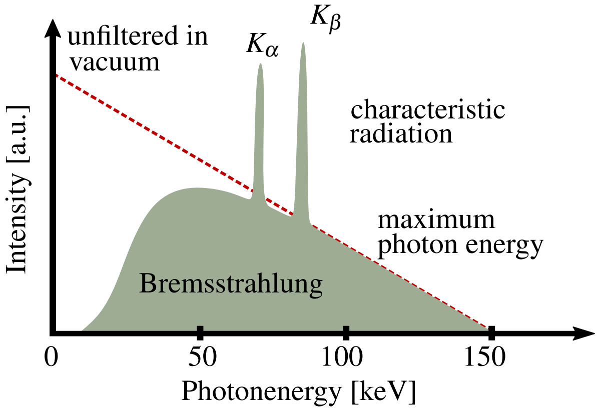

Figure 2.4: The X-ray energy spectrum generated by an X-ray tube.

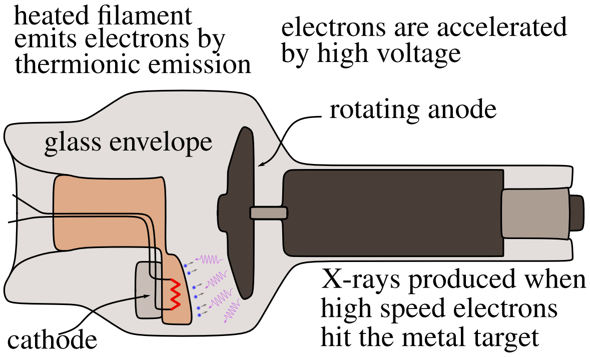
heated filament emits electrons by thermionic emission
electrons are accelerated by high voltage
rotating anode
glass envelope
X-rays produced when high speed electrons hit the metal target
cathode

Figure 2.5: The functional components of an X-ray tube.

with r_e denoting the classical electron radius and P a scalar to account for the radiation's polarization. The wave's amplitude $f(\mathbf{q},E)$ is called the atomic scattering factor. All information regarding the interaction of the photon with the bound electrons of the material is contained in this factor. E denotes the photon's energy and $\mathbf{q} = \mathbf{k}' - \mathbf{k}$ the scattering vector, given by the difference between wave vectors $\mathbf{k}'$, $\mathbf{k}$ of the incoming and outgoing wave. The scattering factor is expressed as

$$f(\mathbf{q},E) = f_0(\mathbf{q}) + f_1(E) + i \cdot f_2(E) \quad , \tag{2.3}$$

where f_0 is the form factor, and f_1 and f_2 the dispersion corrections [108]. Using this model, the differential scattering cross-section can be rewritten as

$$\left(\frac{d\sigma}{d\Omega}\right) = {r_e}^2 \cdot \left|f(\mathbf{q},E)^2\right| \cdot P^2 \quad . \tag{2.4}$$

From this, the scattering cross-section σ_{total} is obtained by integrating over the solid angle Ω. The cross-section is a measure for the probability to observe an interaction event, such as scattering or absorption, between an incoming particle with another. In the X-ray range it can be decomposed into three distinct physical effects contributing to the interaction of photons with matter:

$$\sigma_{total} = \sigma_{Photo} + \sigma_{Compton} + \sigma_{Rayleigh} \quad . \tag{2.5}$$

Here σ_{Photo}, $\sigma_{Compton}$ and $\sigma_{Rayleigh}$ are the photo-electric, the Compton- and the Rayleigh cross-sections, respectively. The total cross-section and its constituents as a function of the energy are exemplary given for water and iodine in Fig. 2.6.

Rayleigh scattering is a coherent and elastic scattering. Hereby the photon barely exchanges energy. While its contribution to attenuation of X-rays is negligible, it generates a phase-shift relative to the incoming photon. On the contrary, the remaining two cross-sections are indeed inelastic scatter processes and change the energy of the incoming photon. Thus, they are responsible for the attenuation. At lower energies attenuation is mainly due to the photo-electric effect, while for increasing energies, attenuation is dominated by the incoherent Compton scattering.

The photo-electric cross-section σ_{Photo} measures the probability of the photo-electric effect to occur. At lower photon energies a characteristic structure appears as explained in Sec. 2.1.3. Their location in the energy range depends on the material of interest. As shown in Fig 2.6 the photo-electric cross-section for

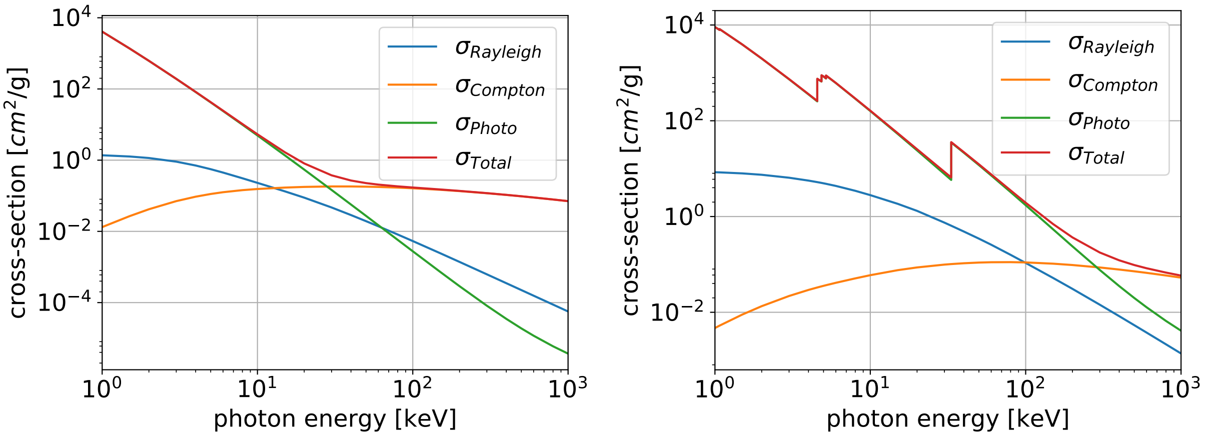

(a) Cross-section for water.

(b) Cross-section for iodine.

Figure 2.6: Cross-sections for water and iodine. Cross-section data from [13].

water is steady in the X-ray energy range, while the photo-electric cross-section for iodine shows K-edges. Above the material's K-Edges the photoelectric cross-section is estimated by

$$\sigma_{Photo}(Z,E) \approx C_1 \cdot \frac{Z^{C_2}}{E^3} \quad , \tag{2.6}$$

where C_1 depends only on natural constants, $C_2 \approx 4$, Z is the atomic number and E the energy [31].

The Compton effect denotes the energy decrease of a photon when scattered inelastically e.g. at electrons. The probability to observe the Compton effect is given by its cross-section $\sigma_{Compton}$

$$\sigma_{Compton}(Z,E) = Z \cdot \sigma_{KN}(E) \quad , \tag{2.7}$$

where $\sigma_{KN}(E)$ is the the relativistic Klein-Nishina cross-section for the scattering of a photon on a single free electron [53].

It is often favorable to describe microscopic interactions in a particle image. In optics this is used in the semi-classical wave formalism [40, 17]. Within this approach the interaction and propagation of an electronic-magnetic wave can be described conveniently by the complex index of refraction n. It is defined by the ratio of the wavenumber k in a material relative to the one in vacuum. Moreover, this can be further related to the atomic scattering factor $f(0,E)$ [108]:

$$n = \frac{k_{mat}}{k_{vav}} = 1 - \frac{r_e}{2\pi} \cdot \lambda^2 \cdot \rho_N \cdot f(0,E) \quad , \tag{2.8}$$

where r_e is the classic electron radius, λ the wavelength, and ρ_N the particle number density. The number density ρ_N is given by the number of atoms per unit volume and depends on the specimens material. It may be expressed by

$$\rho_N = \frac{\rho_M N_A}{M} \quad , \tag{2.9}$$

where ρ_M is the mass density, N_A Avogadro's number and M the molar mass. Combining Eqns. 2.3 and 2.8 leads to the representation of the complex refractive index

$$n(\mathbf{r}) = 1 - \delta(\mathbf{r}) + i\beta(\mathbf{r}) \quad , \tag{2.10}$$

where δ is the refractive decrement defined by

$$\delta = \frac{r_e}{2\pi}\lambda^2 \rho_N \cdot (f_0 + f_1) \ , \tag{2.11}$$

and β is the attenuation decrement given by

$$\beta = \frac{r_e}{2\pi}\lambda^2 \rho_N \cdot f_2 \ . \tag{2.12}$$

It can be shown that the form factor f_0 is dominant in forward direction and approaches $f_0 = Z$, whereas the dispersion correction f_1 is approximately 0, except near to the absorption edges [22]. Thus, the functional dependence of the refractive decrement can be approximated away from the K-Edges in terms of the electron density $\rho_Z = \rho_N \cdot Z$ to

$$\delta = \frac{r_e}{2\pi}\lambda^2 \rho_Z \ . \tag{2.13}$$

In X-ray attenuation imaging one prefers to use the linear attenuation coefficient μ over the attenuation decrement β. Both can be related to the total cross-section σ_{total} by definition as

$$\mu = 2k\beta = 2r_e\lambda\rho_N f_2 = \rho_N\sigma_{Tot} = \frac{\rho_M N_A}{M} \cdot \sigma_{Tot} \ . \tag{2.14}$$

Inserting Eqns. 2.6 and 2.7 we get for the attenuation coefficient

$$\mu = \rho_Z \cdot \left(C_1 \frac{Z^{C_2 - 1}}{E^3} + \sigma_{KN} \right) = \rho_N \cdot \left(C_1 \frac{Z^{C_2}}{E^3} + Z\sigma_{KN} \right) \ . \tag{2.15}$$

2.3 Propagation of X-rays

It can be seen from the previous section that the interaction of X-rays with matter can be described with the complex index of refraction. The following provides a description of the propagation of X-rays through vacuum and matter. A major result is that X-rays do not only lose energy, but experience a phase-shift. This is fundamental to understand how contrast is generated in phase-sensitive X-ray imaging [17, 40, 34].

Classically, X-radiation as electro-magnetic radiation is described by the maxwell equations. In vacuum this will lead to the wave equation

$$\left(\frac{1}{c^2}\frac{\partial^2}{\partial t^2} - \nabla^2 \right) \psi(\mathbf{r}, t) = 0 \ , \tag{2.16}$$

with c being the speed of light. It can be shown that a complex, scalar valued wave function Ψ is sufficient to describe the electromagnetic field at any three dimensional point $\mathbf{r} = (x, y, z)$ at any time t [34, 77]. Decomposed in the spectral components, that is

$$\psi(\mathbf{r}, t) = \frac{1}{2\pi} \int \psi_\omega(\mathbf{r}) \exp[-i\omega t] \, \mathrm{d}\omega \ , \tag{2.17}$$

and inserted into Eq. 2.16 one obtains the so-called Helmholtz equation for each spectral component $\psi_\omega(\mathbf{r})$.

$$\left(\nabla^2 + k^2 \right) \psi_\omega(\mathbf{r}) = 0 \ . \tag{2.18}$$

Here k is the wave number given by $k = \omega/c$ and ω the angular frequency [77].

However, in presence of matter the equations above are no longer valid, because the components of the electrical and magnetic fields are coupled via the Maxwell equations. These decouple under two conditions:

First, a vanishing current and charge density. Second, a static and spatially slowly varying permittivity and permeability. Under these assumptions their solution can be written as a complex, scalar field [77]. As in the vacuum case, the spectral components can now be described by the inhomogeneous Helmholtz equation

$$\left(\nabla^2 + k^2 n_\omega^2(\mathbf{r})\right) \psi_\omega(\mathbf{r}) = 0 \ . \tag{2.19}$$

Effects like attenuation and refraction are inherently encoded in this equation via the complex index of refraction introduced in Eqn. 2.10. Note that a general solution of the maxwell equations can always be expressed as the linear combination of the monochromatic solutions [34]. Thus, we will consider only one spectral component and skip from now on the index ω for the sake of clarity.

In order to solve Eqn. 2.18, we first consider the simple case of a homogeneous medium with $n(\mathbf{r}) = n$. A simple ansatz of a plane-wave propagating in z-direction is sufficient:

$$\begin{aligned} \psi(z) &= \psi(0) \cdot \exp(ink_z z) \\ &= \psi_0 \cdot \exp(ik_z z) \cdot \exp(-i\delta k_z z) \cdot \exp(-\beta k_z z) \ . \end{aligned} \tag{2.20}$$

Here, $\psi_0 := \psi(0)$ is the amplitude at $z = 0$ and k_z the z-component of the wave vector. In the second step we have inserted the definition of the refractive index - see Eqn. 2.10. In a physical experiment one can access only the intensity $I(z)$, given by the amplitude squared:

$$I(z) = |\psi(z)|^2 = |\psi_0|^2 \cdot \exp(-2\beta k_z z) = I_0 \exp(-\mu z) \ . \tag{2.21}$$

Note that the Beer-Lambert law for attenuation follows from this approach [21].

Now, let us consider arbitrary inhomogeneous media. In this case the complete spatial distribution of the complex refractive index needs to be considered. An approximated solution of Eq. 2.19 is given by the projection approximation [77]. Here, one assumes that the refractive index differs only from one between $z = 0$ and $z = \Delta$. Given an initial solution $\Psi_0 = \Psi(x, y, z = 0)$ one has following equation for the propagation along the z-direction:

$$\Psi(x, y, z = \Delta) = \Psi_0 \cdot \exp(ik_z\Delta) \cdot \exp\left[-ik_z \int_0^\Delta \delta(\mathbf{r}) - i\beta(\mathbf{r}) dz\right] \ . \tag{2.22}$$

If the absolute value squared is taken, one obtains again the Beer-Lambert law[1]. It is then given in its general form as the integration over the attenuation coefficient. Thus the imaginary part of the refractive index vanishes if we are interested in the intensity

$$I(x, y, z = \Delta) = I_0 \cdot \exp\left[\int_0^\Delta \mu(\mathbf{r}) dz\right] \ . \tag{2.23}$$

A similar integral over the refractive increment δ, thus the imaginary part of the wave function, yields the phase shift a wave experiences compared to propagation through vacuum:

$$\varphi(x, y, z = \Delta) = -k_z \int_0^\Delta \delta(\mathbf{r}) dz \ . \tag{2.24}$$

Let us now assume a variation of the phase shift φ perpendicular to the direction of propagation, e.g. along the x-axis as visualized in Fig. 2.7. According to Hahn *et al.* [37] this leads to refraction of the wavefront by the angle α. One has

$$\tan(\alpha) = \lim_{\Delta x \to 0} \frac{\varphi(x + \Delta x) - \varphi(x)}{\Delta x \cdot k_z} = \frac{1}{k_z} \frac{\partial \varphi}{\partial x} \ . \tag{2.25}$$

---

[1] Here we used the fact that the absolute value of a complex value a is given by $|a|^2 = a^* \cdot a$. For the complex exponential function $f(x) = e^{ix}$ we thus have $|f(x)|^2 = e^{-ix} \cdot e^{ix} = 1$.

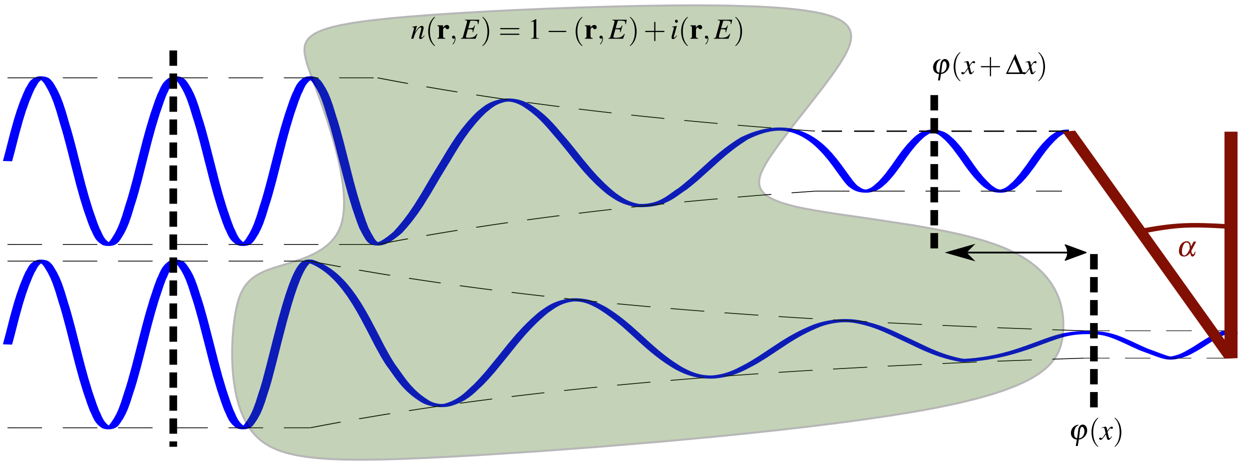
$n(\mathbf{r},E) = 1 - (\mathbf{r},E) + i(\mathbf{r},E)$
$\varphi(x+\Delta x)$
α
$\varphi(x)$

Figure 2.7: Two waves impinge at different locations on an object. The imaginary part of the the refractive index attenuates their amplitudes. The real part causes a change of phase velocity inside the object. Due to the different object sizes one observes different amplitudes and phases. The refraction angle α is determined by the difference of the phase shift of the upper wave at $x_2 = x + \Delta x$ and the lower wave at $x_1 = x$.

Chapter 3

Grating Based X-Ray Imaging

Measurement of the phase shift promises for some materials, such as biological soft tissue, a higher contrast than attenuation. This is due to the high ratio of the local phase shift $k\delta$ and the attenuation coefficient μ [70]. Unfortunately, in most cases the refraction angles occurring in the medical X-ray regime are too small to be directly resolved by a conventional X-ray detector. Thus different methods to measure the phase-shift were proposed in the last century. These are mainly edge-based illumination techniques [76, 27], propagation based [121, 102], analyzer-based [132] or interferometric [16, 69] methods.

In this section a variation of the latter is introduced: X-ray imaging using a grating interferometer exploiting the Talbot-Lau effect [84, 71]. Illumination of a periodic grating produces a self-image at distinct distances downstream. Sampling of this allows the measurement of three complementary image signals in Talbot-Lau interferometer: The attenuation, the differential phase and the dark-field. Firstly, the Talbot-effect is discussed as the theoretical foundation of the contrast mechanism. Secondly, the Lau-effect is introduced which is necessary when a large focal spot is used. Subsequently, a review of how a conventional X-ray setup is augmented to provide the desired image information will be carried out. Last, the three image modalities will be examined.

3.1 Talbot-Effect

Foundation of grating-based X-ray imaging is the Talbot-effect [59], named after its discoverer William Henry Fox Talbot [105]. He was the first to observe self-images of absorbing and periodic structures at discrete distance downstream of illumination with a monochromatic coherent light source. The Talbot-Effect is visualized in Fig. 3.1. Application of Fresnel propagation reveals that these distances are given by integer multiples of the Talbot-distances z_T [77]

$$z_T = \frac{2g^2}{\lambda} \quad . \tag{3.1}$$

Here g denotes the structure's period and λ the applied wavelength. Moreover, it was shown that the Talbot-effect also appears when periodic structures are used, which do not absorb, but instead modulate the phase of the incident electromagnetic waves. An overview for different configurations is given in [104]. If we constrain ourselves to gratings with a duty cycle of 0.5 with a phase modulation of π and $\pi/2$, one has for the distances of the self-images

$$z_T(m_T) = \frac{1}{\eta^2}\frac{m_T g^2}{2\lambda} \qquad \forall m_T \quad \text{odd} \quad , \tag{3.2}$$

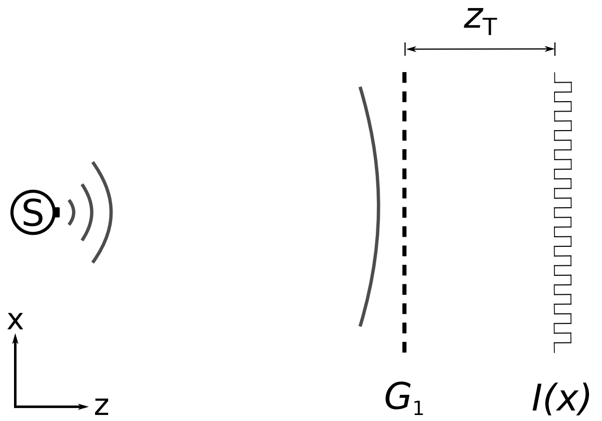

Figure 3.1: Schematic example for the Talbot effect. A coherent source S illuminates a periodic grating G_1. At a distance z_T downstream of G_1 a periodic intensity distribution is observed according to the Talbot effect.

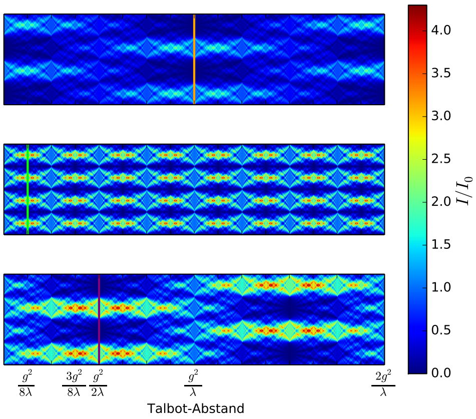

Figure 3.2: Numerical calculation of the intensity downstream of a periodic structure. The topmost image shows an absorbing grating, the middle image a π shifting phase-grating and the lowermost image a $\pi/2$ phase-grating. Taken from [123].

where m_T is an odd integer. For η we differentiate $\eta = 1$ for a $\pi/2$ shifting grating and $\eta = 2$ for a π shifting grating.

Figure 3.2 shows the simulated intensity distribution obtained by numerical simulation downstream of an absorption grating and two phase gratings. The wave propagates from left to right and has an incoming intensity I_0. For the absorption grating one observes the self image at the Talbot distance and a lateral translated image at half of the Talbot distance, denoted by the orange line. The first fractional Talbot distances are denoted in green and violet for the two phase gratings. In case of the π shifting grating one observes frequency doubling of the diffraction pattern.

3.2 Lau-Effect

As mentioned above, a requirement for formation of the Talbot effect is sufficient spatial and lateral coherence of a monochromatic wave. This is only provided for synchrotron radiation or micro-focus X-ray tubes. Conventional X-ray tubes have a finite focal size and thus a small spatial coherence [84].

This constraint is overcome by exploiting the Lau-effect named after its discoverer E. Lau [57]: By adding an additional grating, the source grating G_0, in front of the X-ray source, the Talbot-effect is still observed for spatially incoherent polychromatic radiation. This was first shown for white light by Jahns *et al.* [45] and then adapted by Pfeiffer *et al.* [84] for X-ray illumination.

The source grating is illuminated with conventional radiation from an X-ray tube. Downstream of each slit, the radiation can be assumed to be spatially coherent. Thus, each slit will generate Talbot images of the phase grating G_1 for its own. Each Talbot patterns is now arranged to interfere constructively with the other Talbot patterns. To achieve this g_0, the source grating period, has to be chosen accurately to match g_2, the period of the Talbot pattern. This relation is calculated using the intercept theorem by

$$\frac{g_0}{g_2} = \frac{l_{01}}{l_{12}} , \tag{3.3}$$

where l_{01} denotes - as illustrated Fig. 3.3 - the distance between source and phase grating, and l_{12} the distance between phase and the Talbot distance of interest.

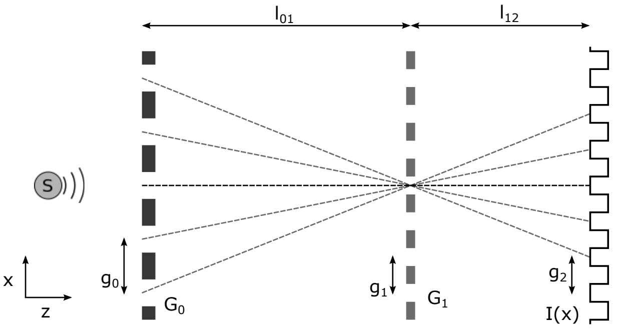

Figure 3.3: Schematic example of the Lau-Effect. The X-ray source illuminates the source grating G_0 with incoherent polychromatic radiation. Each slit can be seen as a coherent source leading to a Talbot pattern of G_1. To observe maximum contrast the Talbot pattern imposed by each single slit should interfere constructively. The intercept theorem has to be fulfilled.

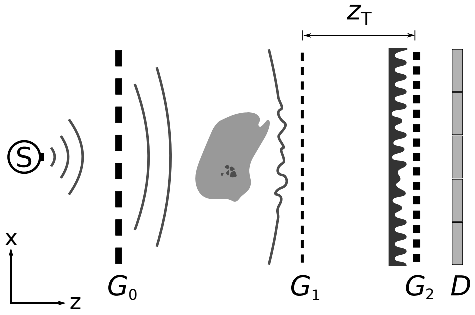

Figure 3.4: Schematic illustration of a Talbot-Lau interferometer with an object inserted. Each slit in G_0 produces sufficiently coherent light generated by a conventional X-ray tube S. The wavefront is then deformed by the object. Downstream of the phase-grating G_1, Talbot images are observed at distance z_T. Image information is retrieved in each detector element by sampling of the Talbot pattern via phase stepping of G_2. The images are recorded by the detector D.

3.3 Talbot-Lau Interferometer

The Talbot-Lau effect introduced above imprints a periodic intensity modulation downstream of a diffraction grating. If a phase-shifting object is inserted into the beam's path, it will distort this intensity modulation. This can then be used to detect the specimen's phase-shift by comparing it to a reference obtained by a prior free-field measurement. If a detector with a pixel pitch much smaller than the period of the fringes were available, one could build a phase-measuring interferometer by simply adding a diffraction grating into the beams path. One would then usually choose a phase-shifting grating for two reasons. First, the loss in intensity during transmission is negligible, thus no additional dose is required. Second, the propagation distances to the first self-images are much shorter than for absorption gratings, allowing for a more compact setup.

However, in case of X-rays the period of these fringes are small compared to the size of a conventional detector pixel[1]. For this reason the fringe pattern cannot be resolved by conventional detectors. This problem is overcome if an additional grating G_2 is added directly in front of the detector. This so-called analyzer grating has highly absorbing bars and has the same period as the diffraction pattern induced by the Talbot-Effect. The intensity modulation is then sampled by lateral shifting of the analyzer grating perpendicular to the grating bars in fractional amounts of its period [117]. At each so-called phase-step, an exposure is taken. This results in a periodic intensity modulation measured in each detector pixel. This modulation is also called phase-stepping curve and is generated by convolution of the transmission function of the analyzer grating with the intensity distribution of the Talbot pattern.

In the ideal case with a monochromatic point source and a truly rectangle intensity modulations of the gratings, this would result in triangular shaped phase-stepping curves. However, in reality this signal is blurred by effects like a finite X-ray source, polychromatic effects and grating imperfections. Eventually,

---

[1] One could build the G_1 to produce fringes large enough to be resolved by a conventional detector. However, the interferometer's sensitivity would approach 0. No image information could be retrieved.

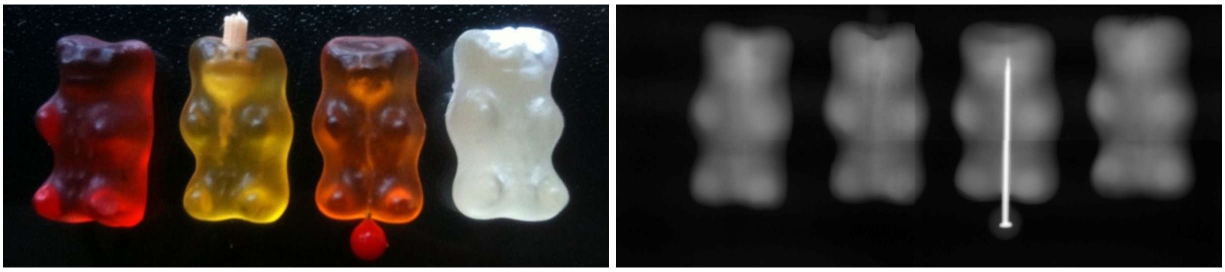

(a) Optical image of specimen

(b) Attenuation

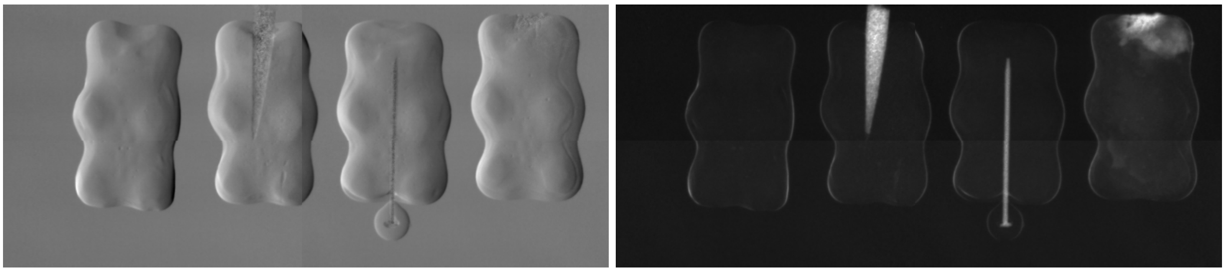

(c) Differential Phase

(d) Dark-Field

Figure 3.5: Example images to demonstrate Grating Based X-Ray interferometry and the different information it provides. The specimen is made of 4 gummy bears. The first (red) was imaged without any preparation. The second (yellow) has a splinter of wood inserted on its top. The third (red) one contains a pin made of metal and a plastic head. The last (white) is filled with small PMMA-beads on its top with a diameter of 6 µm. Images from ECAP [128].

an almost sinusoidal phase-stepping curve will be measured [118].

3.4 Image Modalities

In grating-interferometry the object information is encoded in the deformation of the Talbot pattern. This can be measured by comparing the object measurement with the reference measurement. Three types of image information can be retrieved: Absorption, differential phase-shift and the loss of contrast. Example images are shown in Fig. 3.5. The following section discusses first how this image information is retrieved from the phase-stepping data. This follows a detailed discussion of the three image modalities.

Phase-Retrieval

The phase stepping curves of both, reference and object, can be parameterized by

$$N(x_s) = N + A\cos(\phi + \phi(x_s)), \tag{3.4}$$

where $N(x_s)$ are the measured photon counts at G_2 position x_s. N is the mean photon count, A the amplitude, ϕ the phase of the stepping curve and $\phi(x_s) = 2\pi \cdot \frac{x_s}{p_2}$ the relative phase. p_2 denotes the period of the analyzer grating. Note that a photon counting detector was assumed. For an energy integrating detector one would exchange the photon counts with mean intensity I.

Using this parameterization, one can fit the three unknowns N, ϕ, and A to the measured data as demonstrated in Fig. 3.6. Common phase-retrieval methods employ Least-Squares-Fitting [115], the discrete Fourier transform [117, 83] or deconvolution techniques [68].

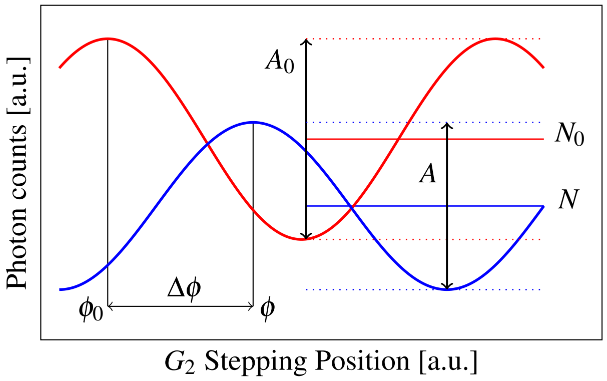

Figure 3.6: Red: Reference stepping curve without object, Blue: Object stepping curve. Each curve is described by three parameters: The offset N, the phase ϕ, and amplitude A. The visibility is then given by $V := \frac{A}{N}$.

If the fitted data for object and reference are compared, one obtains a set of three independent, projective images: Attenuation, differential phase and the dark-field. In the following these three types of information are introduced.

Attenuation

The transmission T of the object in a detector element is calculated by the ratio of the mean photon counts of the reference and object phase stepping curve by

$$T = \frac{N}{N_0} \ . \tag{3.5}$$

The Beer-Lambert law can be applied to solve for the line integral over the attenuation coefficient. However, note that this is only an approximative model. A more realistic model would for instance include the polychromatic character of the attenuation coefficient and scattering effects. The image information corresponds to the one of the conventional attenuation image:

$$\int \mu \, \mathrm{d}z = -\ln(T) = -\ln\left(\frac{N}{N_0}\right) \ . \tag{3.6}$$

The attenuation coefficient depends on the energy, atomic number and density of the matter. For this reason there are high contrast differences between materials with low and high atomic numbers. In medicine, this property is used to image the large differences between hard-tissue like bone (consists mainly of densely packed calcium) and soft-tissue (consists mainly of water). Thus, the attenuation image is a formidable modality to diagnose bone fractures, but delivers low contrast for soft-tissue, e.g. ligaments and tendons.

An example for the attenuation image is given in Fig. 3.5b. The metal pin provides much higher contrast compared to the gummy bears with low attenuation coefficient. The wood splinter inside the second gummy bear yields similar attenuation properties and is barely differentiated from its surrounding. The gummy bear prepared with micro-sized PMMA beads can not be distinguished from the one without any preparation.

Differential Phase-Contrast

The differential phase-shift $\Delta\phi$ through the specimen provides information complementary to the attenuation contrast. It is calculated by taking the difference between the phases of both stepping curves

$$\Delta\Phi = \Phi_0 - \Phi \ . \tag{3.7}$$

It is called differential phase-shift because the image signal is of differential nature. If a wavefront impinges on a phase-shifting object, it will experience a phase-shift caused by different wave velocities in different matter. The wavefront is refracted by angle α compared to the incident wave. The absolute shift of the Talbot fringes is simply given by

$$t = \tan(\alpha) \cdot l_{12} \ , \tag{3.8}$$

where l_{12} is the distance between G_1 and G_2, see Fig. 3.1. Likewise, for the differential phase we have

$$\Delta\Phi = \frac{2\pi}{g_2} \cdot t \ , \tag{3.9}$$

where g_2 is the period of the analyzer grating. Inserting equations 2.24, 2.25, and 3.8 into Eqn. 3.9 we find an expression for the differential phase shift:

$$\Delta\Phi = \frac{2\pi}{g_2} \cdot t = \frac{2\pi z_T}{g_2} \cdot \tan(\alpha) = \frac{2\pi z_T}{g_2} \cdot \frac{\partial}{\partial x} \int \delta(\mathbf{r}) dz \ . \tag{3.10}$$

Equation 3.10 reveals that the image $\Delta\Phi$ is proportional to the phase-shift differentiated in direction of G_2 stepping. Note that this assumes the wave field downstream of an object to be validly approximated by a plane wave with a specific refraction angle. Additionally, the co-domain of the values for the phase difference is $[-\pi, \pi]$. If a value of differential phase shift exceeded the co-domain, it would be mapped again into it. This phenomena is called phase-wrapping and leads to ambiguities, prohibiting a unique determination of $\partial\phi/\partial x$.

An example for the differential image is given in Fig. 3.5c. Due to the differential nature the edges are enhanced. The low absorbing, but the phase shifting plastic head is well imaged. The splinter of wood is also visible.

Dark-Field

The last imaging modality that can be obtained with a Talbot-Lau interferometer is the so-called dark-field [83]. It is linked to the visibility, as a measure of the interference pattern's contrast, given by

$$V = \frac{A}{N} \ . \tag{3.11}$$

The dark-field signal is then retrieved by taking the ratio of object and reference visibility, i.e

$$D = \frac{V}{V_0} \ . \tag{3.12}$$

It is therefore sensitive to the loss of visibility caused by the specimen. A simple way to grasp the dark-field is as follows: Imagine a deformation of the wave-front that is not constant over the detector pixel. This could e.g. happen for an object smaller than the resolution of the detector. The observed intensity distribution no longer matches the analyzer grating: A smaller visibility is measured [93].

In contrary to the attenuation and differential phase image, there are currently no extensive analytic models to describe the origin and information content based on physical processes. However, small-angle scattering, edge-effects and beam hardening have been found to produce a dark-field signal [124, 93, 83].

Yashiro *et al.* [126] investigated both theoretically and experimentally the effects of micron-sized structures on the dark-field. They propose that the dark-field is sensitive to ultra-small-angle X-ray scattering. Michel *et al.* [65] showed possible applications in mammography, where micro calcifications are clearly visible in the dark-field. Another source of loss of visibility are effects at object edges. Yashiro *et al.* have investigated the effect of unresolvable edges [125].

However, a loss of visibility is not only generated due to structural components of the specimen. It is also due to polychromatic artifacts, such as beam hardening or dispersion [80]. A Talbot-Lau interferometer is built to have an optimal visibility at a given photon energy, the so-called design energy. A different reference visibility is measured for X-ray quanta with energies differing to the design energy. Among others, this is because the Talbot distances depend on the energy according to Eqn. 3.1.

This has several consequences for dark-field imaging with polychromatic sources. First, the attenuation coefficient is dependent on the energy as illustrated Eqn. 2.15. Strongly absorbing objects shift the spectral barycenter to higher energies and thus away from the design energy. This may lead to either a a drop-off or increase in visibility. Second, the refractive decrement δ depends on the energy as well. Consequently, the refraction angles experienced by a photon and thus the transversal shift of the intensity fringes depend on the energy. The fringes measured at the detector are the superposition of all spectral components. The measured fringes are hence smeared out and lead to a decrease in visibility.

Figure 3.5d shows an example of the dark-field image. First, a dark-field signal is observed at the edges of each object. Second - and this is most probable more interesting for medical applications - one obtains a high dark-signal for the splinter of wood and the the PMMA-beads due to small-angle-scattering.

Chapter 4

Computed Tomography

Tomography, in its most general definition, refers to imaging by sections exploiting the properties of any kind of penetrating waves [52]. Besides medical imaging techniques, such as CT [21, 129], MRI [72], PET [85] or OCT [43], tomographic methods find applications in numerous scientific areas such as geophysics [74], oceanography [73], astrophysics [49] or even quantum optics [26, 89]. In many cases tomographic information is retrieved by applying mathematical procedures on some sort of input data. These techniques are then referred to as tomographic reconstruction methods.

From now on, we will consider only tomographic techniques where line-integrals are used to form the image contrast, e.g. X-ray attenuation image. Here one seeks to recover the two-dimensional spatial distribution of a scalar, physical property, e.g. the attenuation coefficient, from a tomographic set of projective images. Each of these yield the line integrals over the distribution of the coefficient to be imaged at different angles of projections.

Even though the first tomographic techniques were developed by physicists[1], it is - and by it we mean image reconstruction and not detector or X-ray technology - nowadays arguably more a discipline of computer science, particularly optimization theory.

This is because the imaging process in tomographic systems can be modeled by huge equation systems, often denoted as the system matrix [21, 129]. This is true for almost all (medical) imaging systems, such as PET [78], SPECT, attenuation tomography [33], electron tomography [35] or even novel modalities like photo-acoustic tomography [81]. Unfortunately, in modern systems, these equations are of such large dimensions that a direct inversion is infeasible. This inversion can be avoided by analytical solutions such as filtered back projection. However, analytic solutions may suffer from artifices under certain conditions. Among those are bad photon statistics or polychromatic induced effects. Thus, one often uses iterative reconstruction techniques to find solutions of the tomographic problem. Due to their high computational complexity the development of fast and effective implementations, such as the transfer of computation from CPU to massive, parallel computing on a GPU, is nowadays a vivid field of research [96, 11].

However, besides efficient implementation, iterative reconstruction techniques demand also for novel and complex optimization algorithms [33, 75]. Many of these are formulated in a complex mathematical framework and require deep knowledge of modern optimization theory [101, 30]. With these methods, problems such as motion compensation, region-of-interest-CT, short scans, low-dose CT or 4D-CT can be solved. An overview over those techniques is far beyond the scope of this thesis, but a list of interesting literature shall be given to the interested reader [39, 36, 44, 11, 33, 122].

---

[1] The fundamentals of computed tomography date back to the original paper of Johann Radon in 1917 [86]. Albeit, this was published in a journal for mathematics, his methods regained interest when the first tomographic scanners were built in 1972 [21].

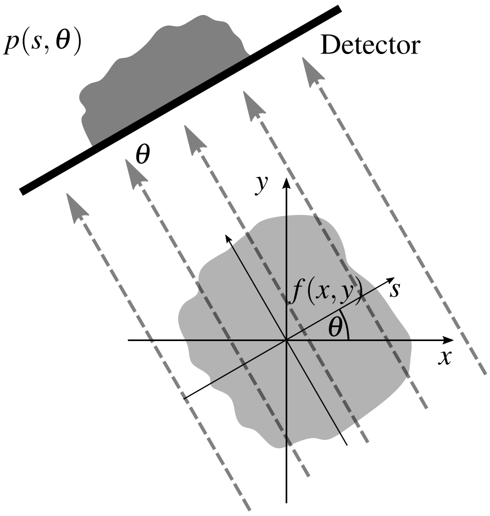

Figure 4.1: Parallel beam projection geometry. Redrawn after [129].

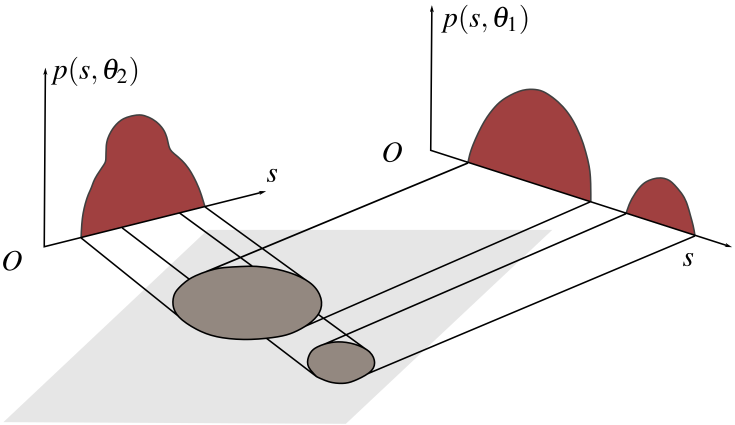

Figure 4.2: Tomographic images from different angles of projection. Redrawn after [129].

In this chapter, we will give an overview over common CT reconstruction methods, which serve as an inevitable tool throughout this thesis. We shall start with the radon transform as a mathematical description of the image formation process. Second, the Fourier-Slice-Theorem as a basis for analytic reconstruction is introduced. Subsequently, we discuss iterative, in particular statistical, reconstruction techniques. In the last part, we adapt the earlier introduced reconstruction techniques to data obtained by a Talbot-Lau interferometer. There are many textbooks about the fundamentals of tomography, such as [52, 21, 129], which are recommended for the interested reader.

4.1 Analytic Reconstruction

For the sake of simplicity, all derivations are given only for a two dimensional parallel beam imaging geometry which is indicated in Fig. 4.1. The adaption to fan-beam or the three dimensional cone-beam geometry is straight forward and intensively discussed in literature [21, 129].

A projection p is mathematically described by the line integral over a object function f. This can be expressed by

$$p(s,\theta) = \int_{\mathbb{R}^2} f(x,y) \cdot \delta(\mathbf{x} \cdot \boldsymbol{\theta} - s)\,\mathrm{d}x\,\mathrm{d}y \ , \tag{4.1}$$

where $\mathbf{x} = (x,y) \in \mathbb{R}^2$ and $\boldsymbol{\theta} = (\cos\theta, \sin\theta) \in \mathbb{R}^2$. θ indicates the projection angle as demonstrated in Fig. 4.1. The scalar s is the distance of the straight line in the 2D object from the origin $(0,0)$ and δ describes the Dirac delta function [129]. An example for projections at two different angles is given in Fig. 4.2.

The projection $p(s,\theta)$ of the object function $f(x,y)$ is the integral transform from spatial coordinates (x,y) to projective coordinates (s,θ). Radon has been the first to propose a mathematical framework to recover the object function from a set of projective line integrals [86]. The transformation is therefore often referred to as Radon transform and its inverse is then the tomographic reconstruction. In case of infinite projection angles and a continuous, noise-free detector signal Radon showed that a unique reconstruction is possible.

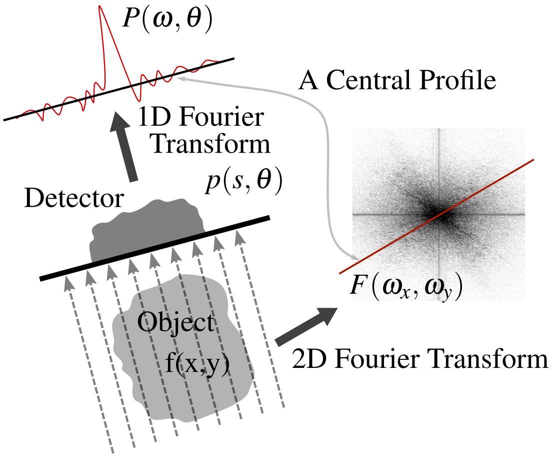

Figure 4.3: Fourier slice theorem. Redrawn after [129].

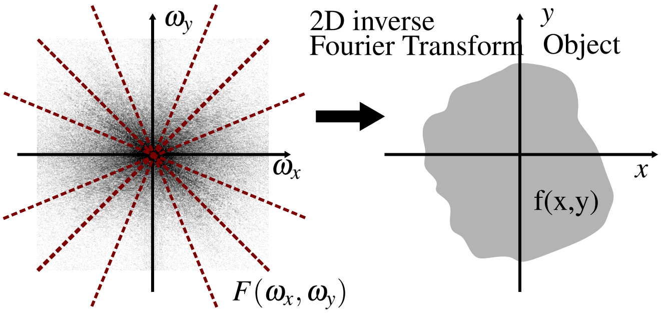

Figure 4.4: 2D inverse Fourier transform to retrieve the object function. Redrawn after [129].

An important finding of his work is the central slice theorem, visualized in Fig. 4.3. It states that the 1D Fourier transform of the projection of a 2D function equals a 1D subspace in the 2D Fourier transform of the object function. This can be written as

$$P(\omega,\theta) = \int_{-\infty}^{\infty} p(s,\theta)\cdot e^{-2\pi i s\omega}\,\mathrm{d}s = F_{polar}(\omega,\theta) \tag{4.2}$$

where $P(\omega,\theta)$ is the 1D Fourier transform of $p(s,\theta)$ at fixed angle θ and $F_{polar}(\omega,\theta)$ is the 2D Fourier transform of the object function $f(x,y)$ given in polar coordinates. The object function can now be restored from a set of projective images by three steps. First, calculation of the 1D Fourier transform to fill up the 2D Fourier space of the object function in polar coordinates. Second, a coordinate transform of the 2D Fourier transform from polar coordinates into cartesian coordinates. Last, application of the inverse Fourier transform - illustrated in Fig. 4.4 - to retrieve the object function in spatial coordinates.

In the following we will discuss these steps in more detail to derive the filtered back projection algorithm. First we write the definition of the Fourier transform in polar coordinates

$$f(x,y) = \int_0^{2\pi}\int_0^{\infty} F_{polar}(\omega,\theta)\cdot e^{2\pi i\omega(x\cos\theta+y\sin\theta)}\,\omega\,\mathrm{d}\omega\,\mathrm{d}\theta \quad . \tag{4.3}$$

Note here the multiplicative term ω appearing in the integral. The spatial frequency ω results as the determinant of the Jacobian matrix of the coordinate transform. Making use of the Fourier property $F_{polar}(\omega,\theta) = F_{polar}(-\omega,\theta+\pi)$ we have

$$f(x,y) = \int_0^{\pi}\int_{-\infty}^{\infty} F_{polar}(\omega,\theta)\cdot|\omega|\cdot e^{2\pi i\omega(x\cos\theta+y\sin\theta)}\,\mathrm{d}\omega\,\mathrm{d}\theta \quad . \tag{4.4}$$

Now inserting the Fourier-Slice theorem $P(\omega,\theta) = F_{polar}(\omega,\theta)$ reveals the connection to the Radon transform:

$$f(x,y) = \int_0^{\pi}\int_{-\infty}^{\infty} P(\omega,\theta)\cdot|\omega|\cdot e^{2\pi i\omega(x\cos\theta+y\sin\theta)}\,\mathrm{d}\omega\,\mathrm{d}\theta \quad , \tag{4.5}$$

where $|\omega|$ acts as the so-called Ramp filter. Let $P(\omega,\theta)\,|\omega| = Q(\omega,\theta)$; then

$$f(x,y) = \int_0^{\pi}\int_{-\infty}^{\infty} Q(\omega,\theta)\cdot e^{2\pi i\omega(x\cos\theta+y\sin\theta)}\,\mathrm{d}\omega\,\mathrm{d}\theta \tag{4.6}$$

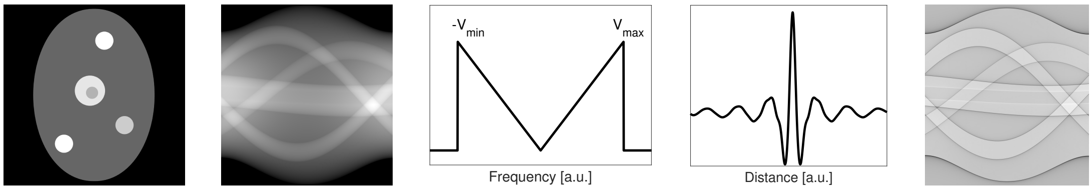

(a) Ground Truth (b) Radon transform (c) Ram-Lak frequency domain (d) Ram-Lak spatial domain (e) Radon filtered

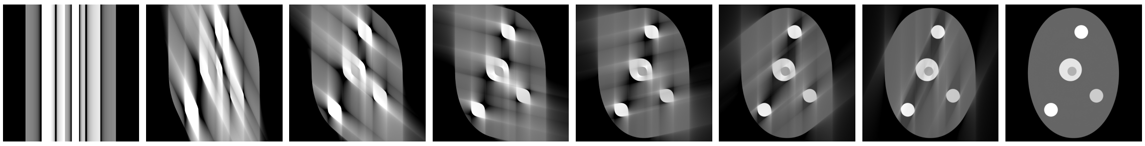

(f) (g) (h) (i) (j) (k) (l) (m)

Figure 4.5: Visualization of the filtered back projection algorithm. For each projection angle the Ramp filtered detector signal is subsequently smeared back into the reconstruction volume. Figures f-m illustrate how the image gradually evolves. Only a scan over the full range of 180° is sufficient for correct reconstruction. The images have been created using the reconstruction framework developed in this thesis.

is split into two independent integration. Remembering the definition of the inverse 1D Fourier transform, we recognize the latter in the inner part of the integration and write

$$f(x,y) = \int_0^{\pi} q\left(x\cos\theta + y\sin\theta, \theta\right) \mathrm{d}\theta \quad , \tag{4.7}$$

where q is the ramp filtered signal of one projection at fixed angle θ.

Equation 4.7 contains the framework of the filtered back projection algorithm visualized in Fig. 4.5. The measured Radon transform, or in other words sinogram [129], is hereby convoluted in each detector line by a spatial transform of the Ramp filter. The convolved sinogram is subsequently back-projected and the desired image is directly retrieved.

4.2 Iterative Reconstruction

Filtered back projection is classified as an analytic image reconstruction method, since an exact solution of the inverse Radon transform can be derived for the ideal, continuous case. However, in reality, there is only a finite set of projections and a discretized image due to the finite detector element size. Thus, filtered back projection inherently provides only an approximate solution. For most clinical applications, this is sufficient and often the method of choice due to the low computational effort. However, filtered back projection has several major disadvantages. Among these are:

- There is no exact solution for the case of the three dimensional cone-beam geometry.
- No assumption about the noise in the data is made.
- Objects with large attenuation coefficients, e.g. bone or metal, introduce severe artifacts.
- Region-of-interest scans, such as heart imaging, are cumbersome since FBP requires non-truncated images.

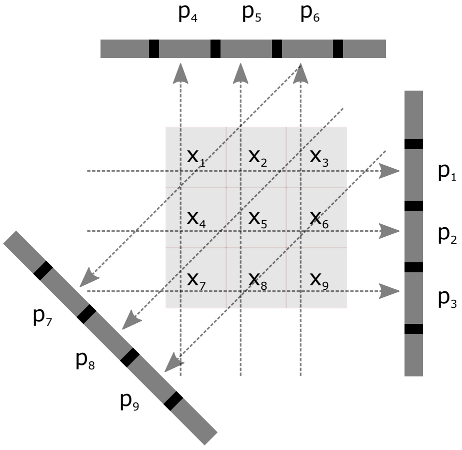

Figure 4.6: Example for a tomographic projection with 9 unknowns and 9 measurements.

- For a minimal dose, one tries to minimize the number of required projections. Highly under-sampled data lead to severe streak artifacts.

So-called iterative reconstruction algorithms can compensate this limitations with an enhanced physical modeling and the possibility to include prior information. In iterative reconstruction, the imaging problem is described by a system of equations. Its inversion is the tomographic reconstruction problem and can be reformulated as an iterative minimization process of an objective function.

System of Linear Equations

In contrary to analytic algorithms, image reconstruction can be performed by solving a system of linear equations. In doing so, the image is discretized into a set of basis functions, e.g. rectangular pixels or radial symmetric functions. In the following, the image coefficients $x_j (j = 1, 2, ...)$ and all projections $p_i (i = 1, 2, ...)$ are labeled in a 1D sequential order as illustrated in Fig. 4.6.

For this simple example, we relate the image and their projections by a set of equations. Here we assume that each beam is infinitely small and hits the center of a detector pixel. The image basis functions are here chosen to be rectangle pixels. In general we can express the tomographic image process as

$$\mathbf{p} = \mathbf{M} \cdot \mathbf{x} \ . \tag{4.8}$$

The projections $\mathbf{p}$ are the measurement data, the system matrix elements of $\mathbf{M} = (M_{ij})$ are given by the system's geometry and the choice of basis functions, and $\mathbf{x}$ are the unknown image coefficients. This matrix is large and cannot be inverted simply. Over the last decades, many algorithms have been dedicated computing $\mathbf{x}$ using iterative reconstruction [33, 29, 21, 129].

In the following, we will first introduce the gradient descent as a method for obtaining $\mathbf{x}$. Its adaption leads to statistical reconstruction which is the basis of the algorithms used throughout this thesis.

4.3 Gradient Reconstruction

Since direct inversion of Eqn. 4.8 is cumbersome, iterative methods are applied for solving for $\mathbf{x}$. A standard method is to rewrite the equation system to form a quadratic cost function

$$f(\mathbf{x}) = \frac{1}{2} \cdot ||\mathbf{M} \cdot \mathbf{x} - \mathbf{p}||_2^2 \ . \tag{4.9}$$

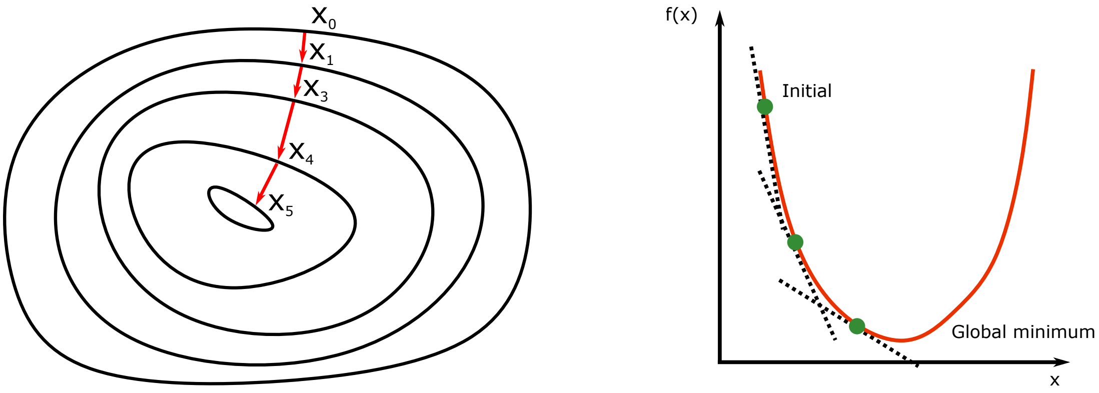

(a) Gradient descent in 2D.

(b) Gradient descent in 1D.

Figure 4.7: Illustration of gradient descent in 2D and 1D.

The objective is now to find a solution $\mathbf{x}$ that minimizes this cost function. We want to remark that due to system noise, these equations can be inconsistent. The cost function will therefore always have positive values.

The most simple optimization technique is the so-called gradient descent. Here, one calculates the gradient of the cost function in respect to all parameters to be optimized and descents along this direction. This is visualized in Fig. 4.7. This procedure will end up in a local minimum. Convergence to a global minimum is guaranteed for convex functions. The general form of a gradient descent is then

$$\mathbf{x}_{t+1} = \mathbf{x}_t - s_t \cdot \nabla_{\mathbf{x}} f(\mathbf{x}_t) \ , \tag{4.10}$$

where $\mathbf{x}_t$ denotes the reconstruction result at iteration t, $\nabla_{\mathbf{x}} f(\mathbf{x_t})$ denotes the current gradient in respect to $\mathbf{x}$ and $s_t \in \mathbb{R}$ the step size. The exact length of step size is not further specified and the optimal (or a least a sufficiently good) value must be calculated in each iteration step to guarantee convergence. This procedure is called step search and requires, especially in high-dimensional optimization, a huge computational effort due to the multiple evaluation of the cost function [103]. The gradient for this cost function is given by

$$\begin{aligned} \nabla_{\mathbf{x}} f(\mathbf{x}) &= \nabla_{\mathbf{x}} \frac{1}{2} \cdot ||\mathbf{M} \cdot \mathbf{x} - \mathbf{p}||^2 && (4.11) \\ &= \mathbf{M}^T (\mathbf{M} \cdot \mathbf{x} - \mathbf{p}) \ . && (4.12) \end{aligned}$$

It involves a forward projection step $\mathbf{M} \cdot \mathbf{x}$ and a subsequent back projection of the difference of estimation and measurement by the transpose $\mathbf{M}^T$.

4.4 Statistical Reconstruction

The objective function in section 4.3 is a simple least-square function. However more complex objective functions are possible. One of them is the so called likelihood. This is the joint probability density function assuming a particular noise behavior, such as Gaussian or Poisson noise. It thus captures the probability to observe a signal given a set of parameters. In fact, the objective function in section 4.3 describes also a likelihood. It assumes a Gaussian distributed data with the same variance for all measurements.

For photon counting detectors, the signal is Poisson distributed [21]. Energy integrating detectors suffer from electron noise, and thus the Poisson model is no longer appropriate. This can be accounted for by e.g. using a shifted Poisson approximation [64]. For many applications the electron noise is negligible. In those cases the Poisson model is sufficient. The Poisson distribution is given by

$$P_\lambda(k) = \frac{\lambda^k}{k!} e^{-\lambda} \quad , \tag{4.13}$$

where λ is the distribution's mean and k the random variable.

In tomographic imaging we seek to reconstruct the spatial distribution of the attenuation coefficient. Employing a forward model, e.g. the Beer-Lambert-Law, one estimates the radiographic images from a set of parameters Θ. For attenuation imaging, Θ is the discretized image of the attenuation coefficient. In the Poisson distribution the mean λ is the expected photon count $n(\Theta)$, whereas k is the actual measured number of photons N.

$$P_n(N) = \frac{n^N}{N!} e^{-n} \quad , \tag{4.14}$$

Note that the expected photon count $n(\Theta)$ is a function of Θ. For better readability we have and will drop Θ, thus $n = n(\Theta)$.

The likelihood L is then given by multiplication of all individual probabilities of all measured pixels according to probability theory

$$\begin{aligned} L(\Theta \mid \mathbf{N}) &= \prod_i P_{n_i}(N_i) \\ &= \prod_i \frac{{n_i}^{N_i}}{N_i!} e^{-n_i} \quad , \end{aligned} \tag{4.15}$$

where $\mathbf{N} = (N_i)$ is the measurement vector. N_i denotes the measured photon count and n_i the expected photon count in pixel i. It is favorable to optimize the Log-Likelihood function instead of the pure Likelihood due to numerical stability:

$$l'(\Theta \mid \mathbf{N}) = \ln L(\Theta \mid \mathbf{N}) = \sum_i \log P_{n_i}(N_i) \quad . \tag{4.16}$$

The position of the maximum will not change due to the strict monotonicity of the logarithm. Furthermore, to obtain a minimization problem, one simply calculates the negative Log-Likelihood function. This is eventually given for the Poisson distribution by

$$l'_P(\Theta \mid \mathbf{N}) = \sum_i -N_i \ln(n_i) + \ln N_i! + n_i \quad . \tag{4.17}$$

The term $\ln N_i!$ is independent of the parameter set and introduces only a constant offset to the function. Thus it is usually dropped from the log-likelihood leading to

$$l(\Theta \mid \mathbf{N}) = \sum_i -N_i \ln(n_i) + n_i \quad . \tag{4.18}$$

This cost function provides a very general framework for inverse problems with Poisson distributed random numbers. Similar statistical cost functions with different noise models, e.g. Gaussian or Rician noise [90], can derived in a similar manner. The reconstruction result is then given by the maximum likelihood estimator obtained by following optimization problem

$$\hat{\Theta} = \underset{\Theta}{\arg\min}\, l(\Theta \mid \mathbf{N}) \quad . \tag{4.19}$$

An essential part in this minimization problem is the so-called forward model. This models the imaging physics how radiographic data $n_i(\Theta)$ are generated from a tomographic image. By minimization of the likelihood we find the parameter set that gives the prediction closest to the actual measurement. For conventional X-ray tomography this forward-model is the Beer-Lambert Law. However, arbitrarily complex models can be defined to account for a more realistic physical modeling. This could include for example a finite beam source, scatter phenomena, detector crosstalk or the polychromatic character of the X-ray source [75].

A simple optimization approach is the gradient descent algorithm, while having the drawback of a slow convergence. For this reason, more advanced optimization algorithms have been proposed in the last decades to efficiently solve the minimization problem of Eq. 4.19 [33, 129, 21, 11]. Since none of these advanced algorithms have been used in this thesis, we refer only to literature at this point. However, adaption of these algorithms to grating-based tomography leaves many open question for future research.

4.5 X-ray Grating-Based Tomography

In the following we will adapt the reconstruction techniques discussed above for X-ray grating-based tomography. It will turn out that analytic reconstruction techniques can directly be applied to all three image modalities. However, phase-retrieval leads to non-uniform noise statistics, which are not accounted for by filtered back projection [115].

An alternative approach was proposed by Ritter *et. al* [92]. It models the Talbot-Lau imaging process and does not require phase-retrieval. However, due to the significantly more complex imaging model no analytic solution can be derived. For this reason the method can only work within an iterative reconstruction framework. Neglecting higher computational effort, this has two major advantages. First, it can account for noise by modeling the photon statistics. Second, this approach does not include phase-retrieval. It allows for reconstruction of data acquired with a continuous, rotating gantry. Time-intensive phase-stepping at each projection angle is no longer required.

4.5.1 Image Model

The three image modalities in grating-based X-ray imaging are the transmission T , the dark-field D and the differential phase $\Delta\phi$. Each quantity is assumed to be tied to a specific object property [92]. The transmission is given as a function over the attenuation coefficient $\mu(\mathbf{r})$. Equally, the differential-phase and the dark-field are a function of the refractive increment $\delta(\mathbf{r})$ and the so called scatter coefficient $\sigma(\mathbf{r})$, respectively.

The transmission T_i which is seen by pixel i is given via the Beer-Lambert Law

$$T_i = \exp\left(- \int_{ray_i} \mu\left(\mathbf{r}\right) \mathrm{d}s \right) \quad . \tag{4.20}$$

The dark-field is a particularly complex property and the physics behind its image creation process are not yet fully understood [124]. Following Bech *et. al* [7] we model the dark-field with the scatter coefficient analogously to the attenuation coefficient by

$$D_i = \exp\left(- \int_{ray_i} \sigma\left(\mathbf{r}\right) \mathrm{d}s \right) \quad . \tag{4.21}$$

We want to stress that previous research has shown that the dark-field is sensitive to the direction of the incoming beam [46, 6, 61]. Therefore, it seems more reasonable to model the dark-field by a vectorial or tensorial entity [6, 61]. However, this is still subject of ongoing research. In order to keep our models as simple as possible, we stick with the model of Eqn. 4.21. Hereby we inherently assume isotropic scattering of our specimen.

According to Eqn. 3.10, the differential phase does not follow the Beer-Lambert law. It is given by the derivative perpendicular to the grating bars of the integrated refractive increment

$$\Delta\phi_i = \frac{2\pi z_T}{g_2} \cdot \frac{\partial}{\partial x} \int_{ray_i} \delta(\mathbf{r})\,\mathrm{d}s \ , \tag{4.22}$$

Given the projected values in each pixel i for transmission T_i, dark-field D_i, and differential phase $\Delta\phi_i$ we expect the observed photon counts $n_{i,s}$ at stepping position s to be

$$n_{i,s} = N_i\left(1 + V_i \cdot \cos\left(\phi_{i,s}\right)\right) \ , \tag{4.23}$$

with the expected mean photon count[2] N_i

$$N_i = N_i^0 \cdot T_i \ , \tag{4.24}$$

the expected visibility

$$V_i = V_i^0 \cdot D_i \ , \tag{4.25}$$

and the expected phase

$$\phi_{i,s} = \phi_i^0 + \phi_s + \Delta\phi_i \ . \tag{4.26}$$

The relative phase $\phi_s = 2\pi\frac{s}{p_2}$ depends on the stepping distance s of G_2 and the grating period p_2. N_i^0, V_i^0, and ϕ_i^0 denote free-field reference measurements for pixel i .

4.5.2 Analytic Reconstruction

In the following we show how filtered back projection can be used in grating-based tomography. If the full information of phase-stepping curves are available in each pixel, one has access to the three images attenuation, dark-field and differential phase.

Talbot-Lau Sinograms and Reconstructed Sinograms

Example phase-stepping sinograms from a tomographic scan performed at ECAP sample are shown in Fig. 4.8. Application of phase-retrieval techniques leads to the three sinograms for attenuation, differential phase and dark-field as shown in Fig. 4.9.

Filtered Back Projection

As shown in Sec. 4.5.1, the attenuation follows the Beer-Lambert Law from conventional X-ray imaging. The filtered back projection as shown in Eqn. 4.5 can therefore directly be applied to calculate the attenuation coefficient $\mu(\mathbf{r})$.

The dark-field was modeled in Eqn. 4.21 by a scalar function with the same structure as the Beer-Lambert for attenuation imaging. In the same manner, filtered back projection with the Ramp filter directly provides the spatial distribution of the scatter coefficient $\sigma(\mathbf{r})$ [7]. One simply replaces the transmission T with the dark-field D and the attenuation coefficient μ with the scatter coefficient σ. As mentioned above, this is only valid for isotropic scattering. If highly anisotropic data are present, more complex image models must be considered, which do not allow for an analytic reconstruction framework [6, 61].

---

[2] The expected mean photon count N_i is not be confused with the measured photon count N_i used in statistical reconstruction for attenuation imaging which has the same notation - see Eqn. 4.15.

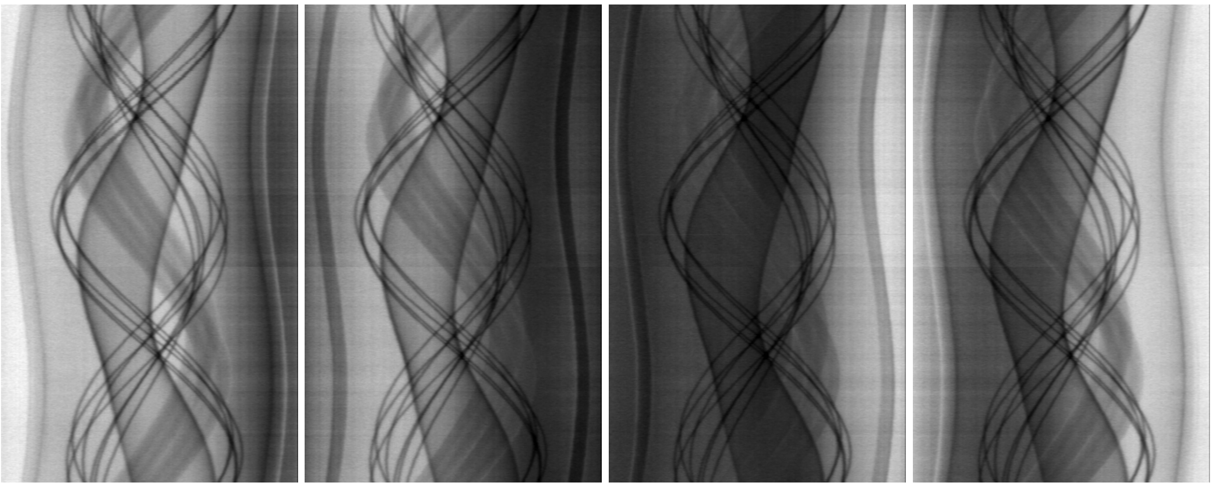

(a) Phase step 1 (b) Phase step 2. (c) Phase step 3. (d) Phase step 4.

Figure 4.8: Examples of raw tomographic Talbot-Lau image data of the specimen shown in Fig. 7.5g. Four phase-steps per projection angle are performed. Note the moving moire pattern on the sinogram.

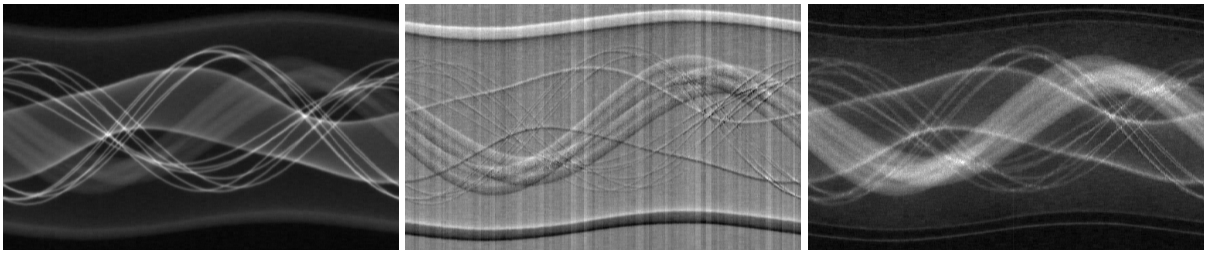

(a) Absorption. (b) Differential phase. (c) Dark-field.

Figure 4.9: Examples of tomographic Talbot-Lau image data obtained by phase-retrieval techniques. Each sinogram can be used to reconstruct a tomographic image using the filtered back projection technique. For the differential image one replaces the Ramp filter with Hilbert filter.

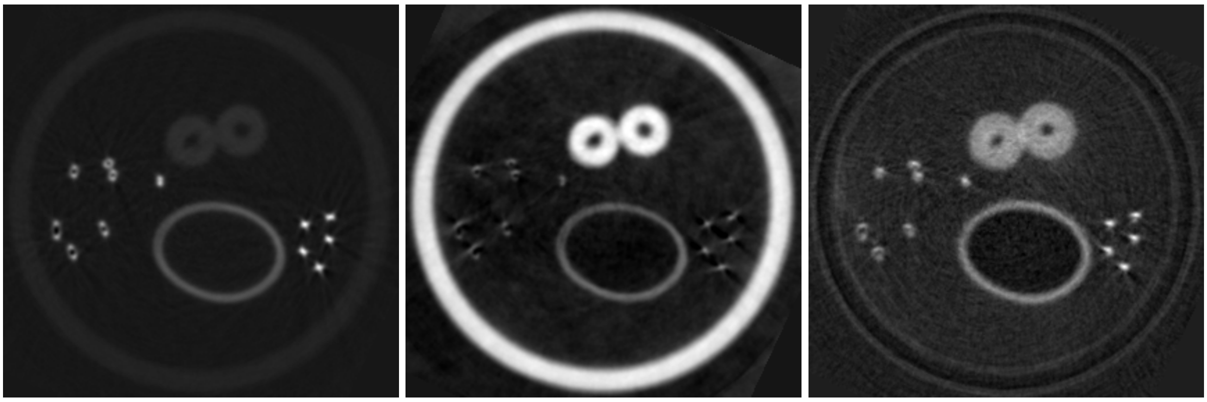

(a) Attenuation. (b) Refractive decrement. (c) Scatter.

Figure 4.10: Examples of tomographic reconstruction of Talbot-Lau data shown in Fig. 4.9 . Reconstruction was done using filtered back projection.

For the refractive decrement, a direct application of filtered back projection is not possible due to the differential nature of the measured projections

$$\frac{\partial}{\partial x}\varphi(s,\theta) = \frac{\partial}{\partial x}\int_{\mathbb{R}^2}\delta(x,y)\cdot\delta_{Dirac}(\mathbf{x}\cdot\theta - s)\,\mathrm{d}x\mathrm{d}y \quad . \tag{4.27}$$

The refractive decrement is denoted by $\delta(x,y)$ and the Dirac function by $\delta_{Dirac}(\mathbf{x}\cdot\theta - s)$. To apply filtered projection directly one would need to measure the Radon transform of the refractive decrement

$$\varphi(s,\theta) = \int_{\mathbb{R}^2}\delta(x,y)\cdot\delta(\mathbf{x}\cdot\theta - s)\,\mathrm{d}x\mathrm{d}y \quad . \tag{4.28}$$

This can theoretically be calculated by integration of the differential phase image. A more elegant way was proposed by [82] to utilize the derivative property of the Fourier transform

$$\mathscr{F}\left[\frac{\partial f}{\partial x}(x)\right] = 2\pi\mathrm{i}u_x\mathscr{F}\left[f(x)\right] \quad , \tag{4.29}$$

where u_x denotes the spatial frequency in x and $\mathscr{F}$ the Fourier transform. Applied for phase-contrast we can write

$$P(\omega,\theta) = \mathscr{F}\left[\varphi(s,\theta)\right] = \frac{\mathscr{F}\left[\frac{\partial\varphi}{\partial x}(x)\right]}{2\pi i\omega} \quad , \tag{4.30}$$

where $P(\omega,\theta)$ denotes the 1D-Fourier transformed radon transform of the refractive decrement. ω is the spatial detector frequency. Writing down the inverse radon transform we then have

$$\begin{aligned}
\delta(x,y) &= \int_0^{\pi}\int_{-\infty}^{\infty} P(\omega,\theta)\,|\omega|\,e^{2\pi i\omega(x\cos\theta + y\sin\theta)}\,\mathrm{d}\omega\,\mathrm{d}\theta \\
&= \int_0^{\pi}\int_{-\infty}^{\infty} \frac{\mathscr{F}\left[\frac{\partial\varphi}{\partial x}(x)\right]}{2\pi i\omega}\,|\omega|\,e^{2\pi i\omega(x\cos\theta + y\sin\theta)}\,\mathrm{d}\omega\,\mathrm{d}\theta \\
&= \int_0^{\pi}\int_{-\infty}^{\infty} \mathscr{F}\left[\frac{\partial\varphi}{\partial x}(x)\right]\frac{-\mathrm{i}}{2\pi}\cdot\mathrm{sgn}(\omega)e^{2\pi i\omega(x\cos\theta + y\sin\theta)}\,\mathrm{d}\omega\,\mathrm{d}\theta \\
&= \int_0^{\pi}\int_{-\infty}^{\infty} \mathscr{F}\left[\frac{\partial\varphi}{\partial x}(x)\right]\cdot W_{hilbert}(\omega)e^{2\pi i\omega(x\cos\theta + y\sin\theta)}\,\mathrm{d}\omega\,\mathrm{d}\theta \\
&= \int_0^{\pi}\frac{\partial\varphi}{\partial x}(x) * w_{hilbert}(x)\,\mathrm{d}\theta \quad ,
\end{aligned} \tag{4.31}$$

where we have introduced the Hilbert filter in the frequency domain

$$W_{hilbert}(\omega) = \frac{-\mathrm{i}}{2\pi}\cdot\mathrm{sgn}(\omega) \quad , \tag{4.32}$$

and in spatial domain as its inverse Fourier transform

$$w_{hilbert}(x) = \mathscr{F}^{-1}\left[W_{hilbert}\right] \quad . \tag{4.33}$$

In the last step, the differential phase image is convolved with the Hilbert filter ($*$ denotes the convolution operator). It follows that the same implementation as for the attenuation reconstruction can be used when the Ramp filter is replaced with the Hilbert filter. Note that the Hilbert filter inherently performs the phase integration in Fourier domain. Example reconstruction done with filtered back projection are visualized in Fig. 4.10 for the sinograms shown above.

4.5.3 Statistical Reconstruction without Phase Retrieval

Analytic tomographic reconstruction techniques have major drawbacks in Talbot-Lau interferometry. At each projection angle, phase stepping data with at least three sampling points must be acquired. Phase-wrapping may occur for highly refractive objects. What is more, the retrieved phase may become arbitrary for non sufficient photon statistics. Both artifacts can introduce severe artifacts in the tomographic reconstruction.

To circumvent these drawbacks, Ritter *et al.* and Brendel *et al.* investigated an adaption of the maximum-likelihood algorithm, to simultaneously reconstruct attenuation, phase and scatter images without requiring phase retrieval [92, 19, 94].

Their basic idea is to use the model of the Talbot-Lau imaging process to provide the expected photon counts $n_{i,s}$ at phase step s measured at pixel i given in Eqn. 4.23. The expected photon counts $n_{i,s}$ depend on a set of parameters Θ which are composed of the attenuation coefficient $\mu(\mathbf{r})$, refractive decrement $\delta(\mathbf{r})$, and the scatter coefficient $\sigma(\mathbf{r})$. Calculating $n_{i,s}$ via Eqn. 4.23 requires estimation of the object's expected transmission T_i, differential phase $\Delta\phi_i$, and dark-field D_i . Following equations 4.20, 4.21, 4.22 we assume that the three image modalities can be modeled by integration along the line-of-sight over the attenuation coefficient, refractive decrement and scatter coefficient[3].

For numerical means, the continuous objects distributions are discretized as described in section 4.2. Each volume element j has an associated attenuation coefficient μ_j, refractive decrement δ_j and scatter coefficient σ_j.

Equations 4.20 and 4.21 are then expressed as linear equations.

$$T_i = \exp\left(-\sum_j M_{ij} \cdot \mu_j\right) \quad , \tag{4.34}$$

and

$$D_i = \exp\left(-\sum_j M_{ij} \cdot \sigma_j\right) \quad , \tag{4.35}$$

where M_{ij} denotes the conventional system matrix element from computed tomography. i denotes the pixel index and j the index of the reconstructed volume element. Equation 4.22 cannot be expressed using the conventional system elements M_{ij} due to the inherent differential character of the image. However, it can still be written with the system matrix approach

$$\Delta\phi_i = \sum_j M^{\delta}_{ij} \cdot \delta_j \quad , \tag{4.36}$$

where the differential character, usually expressed by the partial derivative $\frac{\partial}{\partial x}$ in phase stepping direction of G_2, is taken into account by the differential matrix element M^{δ}_{ij}. Chapter 5 is dedicated to the actual calculation and implementations of the system matrix elements.

Having implemented the image model we adapt the likelihood function of attenuation imaging Eqn. 4.18 to grating-based interferometry. One simply exchanges the measured and expected photon count N_i and n_i with the photon count at stepping position s, thus $N_{i,s}$ and n_{is}

---

[3] This integration could be done by an arbitrary implementation of a forward projector. However, if a standard projector is used, the differential character of the phase image would require numerical differentiation, possibly introducing numeric artifacts. Koehler *et al.* proposed to use Kaiser-Bessel functions as basis functions to phase-contrast reconstruction [55]. The main advantage is that Kaiser-Bessel functions (also known as blobs) provide analytical expressions of the Radon transform and its derivative [58]. More information on this issue is found in chapter 5.

Let $\Theta := (\mu_j, \delta_j, \sigma_j)$ be the parameter set describing the object and $\mathbf{N} := (N_{i,s})$ the set of intensities measured by the detector. Assuming negligible electronic noise leads to the negative log-likelihood for Poisson distributed noise l,

$$l(\Theta \mid \mathbf{N}) = \sum_i -N_{i,s} \ln(n_{i,s}) + n_{i,s} \quad . \tag{4.37}$$

Reconstruction of Θ is then - as in the case of conventional tomography - done by minimization of the likelihood function. Ritter *et al.* proposed to use conjugated gradient [92, 94]. Brendel *et al.* [19] on the contrary argued that the latter performs inefficient and proposed an adaption of the steepest descent by alternatively optimizing each image [19].

Both methods require analytic expression of the gradient of the likelihood function in respect to all voxels of the three images to be reconstructed. For the likelihood in Eqn. 4.37 this is given by

$$\frac{\partial}{\partial \theta_j} l = \sum_{i,s} \left(1 - \frac{N_{i,s}}{n_{i,s}}\right) \cdot \frac{\partial}{\partial \theta_j} n_{i,s} \quad . \tag{4.38}$$

Here θ denotes the specific image, i.e. attenuation, refractive decrement or the scatter image, and j is the voxel we are interested in. Evaluation of Eqn. 4.38 requires calculation of the partial derivative $\frac{\partial}{\partial \theta_j} n_{i,s}$ in respect to each image voxel. For the image discretization as given in Eqns. 4.34, 4.35, 4.36 the partial derivatives are given by:

$$\frac{\partial}{\partial \mu_j} T_i = \frac{\partial}{\partial \mu_j} e^{-\sum_{j'} M_{ij'} \mu_{j'}} = -M_{ij} T_i \quad . \tag{4.39}$$

$$\frac{\partial}{\partial \delta_j} \Delta\phi_i = \frac{\partial}{\partial \delta_j} \sum_{j'} M^{\delta}_{ij'} \delta_{j'} = M^{\delta}_{ij} \quad . \tag{4.40}$$

$$\frac{\partial}{\partial \sigma_j} D_i = \frac{\partial}{\partial \sigma_j} e^{-\sum_{j'} M_{ij'} \sigma_{j'}} = -M_{ij} D_i \quad . \tag{4.41}$$

With this we can calculate the derivatives of the image model $\frac{\partial}{\partial \theta_j} n_{i,s}$ with respect to the three images:

$$\begin{aligned} \frac{\partial}{\partial \mu_j} n_{i,s} &= \frac{\partial}{\partial \mu_j} N_i \cdot (1 + V_i \cdot \cos(\phi_{i,s})) \qquad (4.42) \\ &= -M_{ij} \cdot N_i \cdot (1 + V_i \cdot \cos(\phi_{i,s})) \\ &= -M_{ij} \cdot n_{i,s} \quad . \end{aligned}$$

$$\begin{aligned} \frac{\partial}{\partial \delta_j} n_{i,s} &= \frac{\partial}{\partial \delta_j} N_i \cdot (1 + V_i \cdot \cos(\phi_{i,s})) \qquad (4.43) \\ &= N_i \cdot V_i \cdot (-1) \sin(\phi_{i,s}) \frac{\partial}{\partial \delta_j} \Delta\phi_i \\ &= -N_i \cdot V_i \cdot \sin(\phi_{i,s}) M^{\delta}_{ij} \quad . \end{aligned}$$

$$\begin{aligned} \frac{\partial}{\partial \sigma_j} n_{i,s} &= \frac{\partial}{\partial \sigma_j} N_i \cdot (1 + V_i \cdot \cos(\phi_{i,s})) \qquad (4.44) \\ &= N_i \cdot V_i \frac{\partial}{\partial \sigma_j} D_i \cdot \cos(\phi_{i,s}) \\ &= -N_i \cdot V_i \cdot \cos(\phi_{i,s}) \cdot M_{ij} \quad . \end{aligned}$$

Here N_i, $\phi_{i,s}$, and V_i are the same as in Eqns. 4.24,4.26, and 4.25.

Inserting these into Eqn. 4.38 leads to following gradient for each image type:

$$\frac{\partial}{\partial \mu_j} l = \sum_{i,s} \left(1 - \frac{N_{i,s}}{n_{i,s}}\right) \cdot (-M_{ij} \cdot n_{i,s}) = \sum_{i,s} (N_{i,s} - n_{i,s}) \cdot M_{ij} \quad . \tag{4.45}$$

$$\frac{\partial}{\partial \delta_j} l = \sum_{i,s} \left(\frac{N_{i,s}}{n_{i,s}} - 1\right) \cdot N_i \cdot V_i \cdot \sin(\phi_{i,s}) M_{ij}^{\delta} \quad . \tag{4.46}$$

$$\frac{\partial}{\partial \sigma_j} l = \sum_{i,s} \left(\frac{N_{i,s}}{n_{i,s}} - 1\right) \cdot N_i \cdot V_i \cdot \cos(\phi_{i,s}) M_{ij} \quad . \tag{4.47}$$

A few remarks on the properties of this gradient. The sum in each equation runs over all measured phase-stepping positions in every detector pixel of the sinogram. A closer look reveals that the summation can be split into an outer sum over the pixels and inner sum over the phase-stepping data. Moreover, except of the matrix elements M_{ij} and M_{ij}^{δ}, the sum is independent of the voxel of interest j. Thus the inner sum can be precalculated for each pixel i. Each gradient element denoted as g_j is then calculated by a formula of following structure

$$g_j = \sum_i p_i \cdot m_{ij} \quad , \tag{4.48}$$

where p_i is the inner sum and m_{ij} the system matrix element of the specific image. Note the data from phase step position s is inherently included in this formula. The summation over the Radon space in Eqn 4.48 actually defines a back projection operation for voxel element j.

The calculation of the gradient can be expressed in a simple, non mathematic language: First, estimate the radiographic images using the forward model to calculate the phase-stepping data. Subsequently, the estimated phase-stepping data are compared to the actual measured data. This leaves us with a - let us call it - error sinogram. Last, subsequent back projection of the error sinogram contains the gradient for each voxel element j. Example images of the error sinograms and the gradient for each image (μ, δ, and σ) are given in Fig. 4.11.

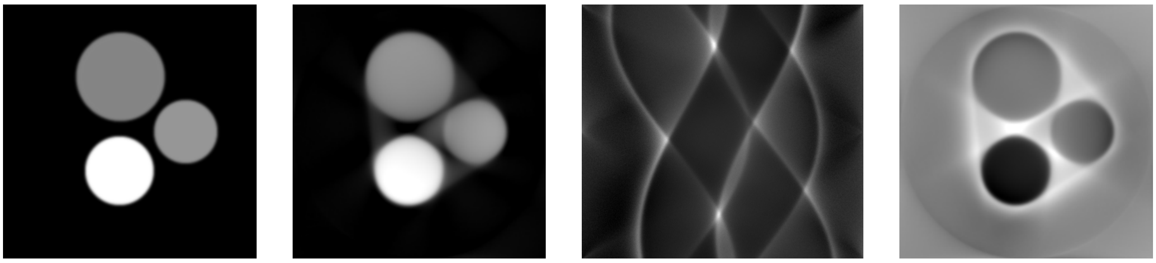

(a) Ground truth μ (b) Reconstruction μ (c) Error sinogram μ (d) Gradient μ

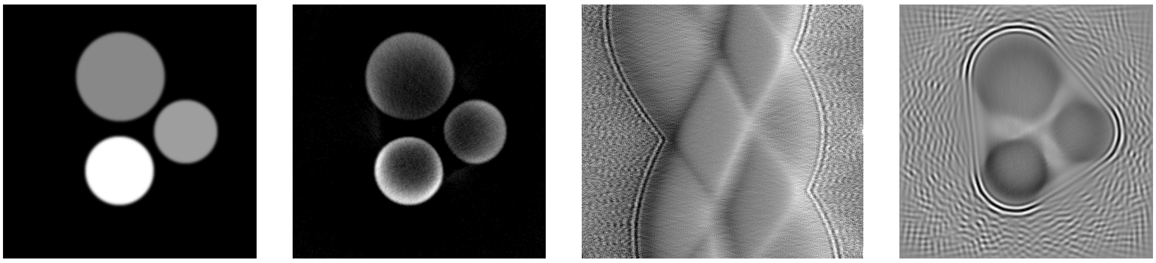

(e) Ground truth δ (f) Reconstruction δ (g) Error sinogram δ (h) Gradient δ

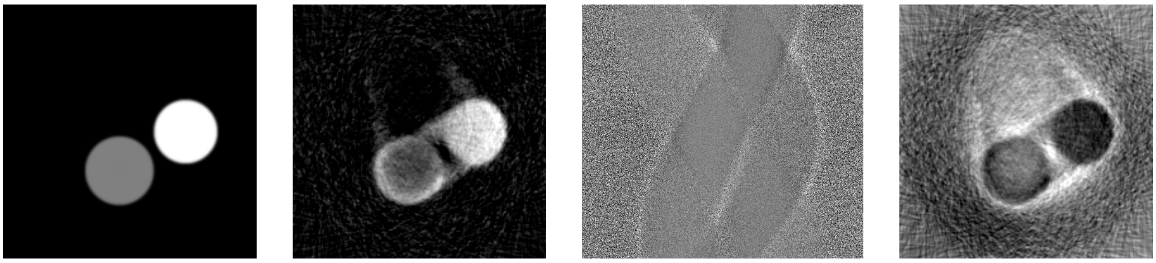

(i) Ground truth σ (j) Reconstruction σ (k) Error sinogram σ (l) Gradient σ

Figure 4.11: Example how the gradient images are calculated. From the current reconstruction (b, f, j) the phase-stepping curves are estimated and compared to the measured data. This results in the so-called error sinograms (c, g, k). Each error sinogram is subsequently back projected to form the gradient in each image voxel (d, h, l). The images were generated using the reconstruction framework developed in this thesis. Simulated phantom data (a, e, i) without any physical meaning were generated. Note that they should be seen as an instructive example. Poor photon statistics were simulated, to show that refractive index δ and scatter σ are more difficult to reconstruct than the attenuation image μ.

Chapter 5

Reconstruction Framework

A major part of this thesis has been the development of a tomographic reconstruction framework for grating based tomography. In this chapter, I will focus on several obstacles that had to be overcome to realize the implementation of the algorithms discussed in chapter 4 and 8.

5.1 Design Considerations

Optimization algorithms in high dimensional space often require a high computation effort. Especially in iterative tomographic reconstruction, the evaluation and optimization of the cost function require time consuming forward and back projection operators. An efficient implementation is crucial to obtain results in a reasonable time.

Furthermore, earlier research has addressed that having a so-called matched forward and backward projector pair can be beneficial for the reconstruction results [129]. By a projector / back projector pair we mean the matrices $\mathbf{A}$ and $\mathbf{A}^T$, as used in Eqn. 4.12. A pair is called matched if the back projection matrix is the actual transpose of the projection $\mathbf{A}$. Otherwise it is called unmatched with a back projection operator $\mathbf{B}$. In many cases the projector / back projector pair can be implemented computationally more efficient using an unmatched pair. This might be disadvantageous for the reconstruction result in form of additional artifacts. However, this is a controversial topic in the tomographic research community [130, 63, 67, 38].

We argue that a matched pair is beneficial if the cost function takes a more complex form than in conventional tomography. This is the case in grating based tomography, where among others a differential forward projection is required [55]. In this case an unmatched operator pair, e.g. using numeric differentiation, could introduce artifacts. A straight-forward way to implement a matched projector/ back projector pair is using the Kaiser-Bessel-Function, henceforth called blob [58, 25].

An effective implementation of blobs turns out to be more complex when translated to GPU computing, which is nowadays state-of-the-art in conventional CT research [111, 15]. For this reason no open source frameworks employing blobs have been available at time of this thesis. Several other open source reconstruction frameworks known to us have been investigated during the begin of this thesis [60, 109, 91, 79]. These frameworks have not been chosen since we believed them to be not suitable for grating based tomography. Moreover, these frameworks require a graphic processing unit for an efficient computation. Unfortunately, the computing resources at ECAP using the high performance cluster did not allow for an easy translation of these algorithms on their system.

In future work on grating based interferometry above mentioned reconstruction frameworks should be considered. CONRAD [60] by Maier *et al.* and the ASTRA toolbox proposed by Aarle *et al.* [109] seem

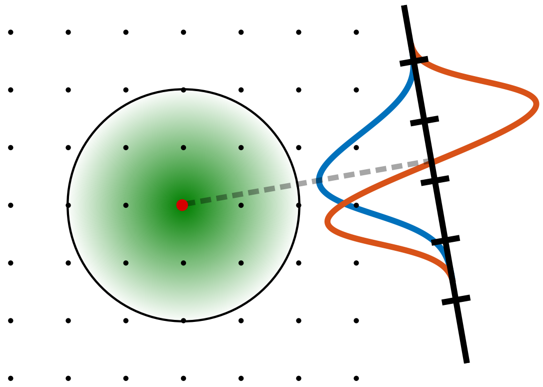

Figure 5.1: Kaiser-Bessel Function and its (differential) footprint on the detector. The blue and orange curves denote the conventional and differential footprint respectively.

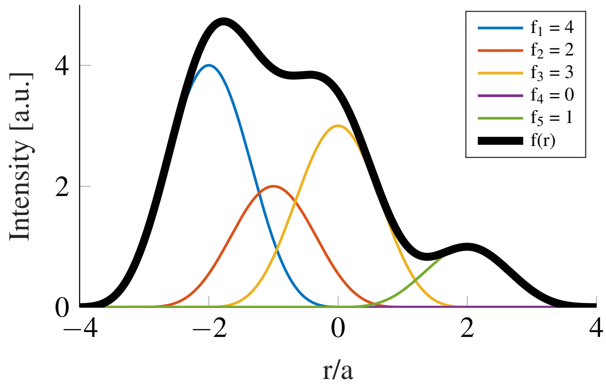

Figure 5.2: Composition of several blobs provide a smooth object function $f(r)$. The strength of each blob i is denoted by f_i.

to provide the required functionality if some minor adaption are made.

In prior work at ECAP performed by Andreas Wolf iterative reconstruction for grating based tomography has been investigated for different basis functions [123]. He has shown that using blobs indeed provides better reconstruction than standard methods like Joseph's interpolation method [48], Siddon's method [100] or distance driven projectors [63]. The major advantage is that a direct access to system matrix elements is herein possible. This enables an easy implementation of well defined differential projectors. It also allows usage of advanced optimization methods as proposed in Sec. 8.3.

The reconstruction framework developed by Wolf is a very prototypic software written in *Python*. Reconstructions with resolutions higher than 60×60 have not been feasible in reasonable time due to an inefficient implementation. As a result of his findings, we decided to re-implement a reconstruction framework from scratch. It is also based on blob functions and is written in the programming language *Java*. The largest problem with using blobs is that they require storing of the system matrix entries in the computer's shared memory. The implementation of the reconstruction framework and concomitant problems are discussed in the subsequent sections.

5.2 Implementation of Forward- and Back Projector

The reconstruction framework developed in this thesis can support an arbitrary forward and back projector operator. Any implementation performing a (differential) forward and back projection can be used within this framework. External implementations, e.g. using GPU, can be added to the framework by adapting their functionality to work with the abstract projector and back projector classes with minimal programming effort.

For this thesis, forward and back projector operators have been implemented from scratch employing Kaiser-Bessel functions [58]. They have been first used in the phase-contrast imaging community by Koehler *et al.* for iterative reconstruction of the refractive decrement [55]. For the phase image, differential system matrix elements are required. In the following we will discuss the Kaiser-Bessel functions and their properties in more detail.

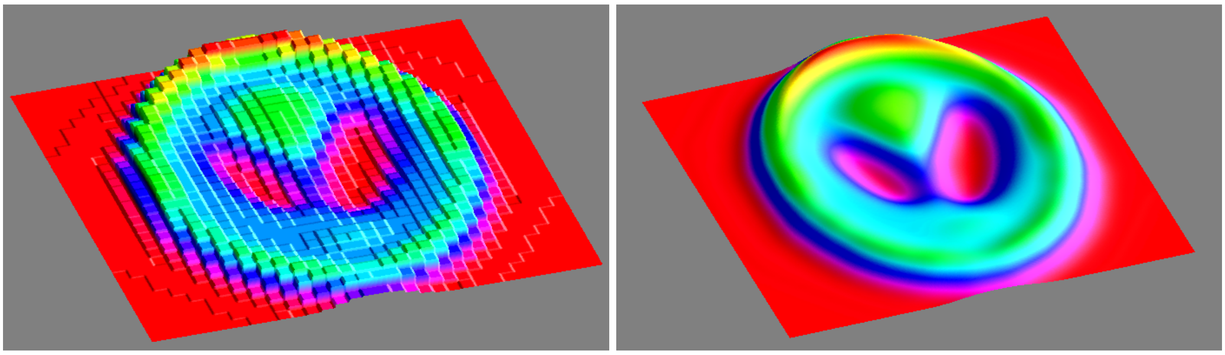

(a) Voxel discretization (32 x 32 pixel).

(b) Blob discretization (32 x 32 pixel).

Figure 5.3: Exemplary visualization of a rectangular and a blob-based discretization. Even though the same number of image coefficients is used, the blob discretized image is smooth. On the contrary, the image using rectangular pixels shows sharp edges.

5.3 Kaiser-Bessel Functions

The blob function is a generalization of the symmetric Kaiser-Bessel function and was first proposed for image representation by Lewitt [58]. It has an almost Gaussian-bell like and always radial symmetric shape. Its radial profile is given by

$$b_{m,a,\alpha}(r) = \begin{cases} \frac{\left(1-(r/a)^2\right)^{m/2} \cdot I_m\left(\alpha \cdot \sqrt{1-(r/a)^2}\right)}{I_m(\alpha)} & \text{for } r \leq a \\ 0 & \text{for } > a \end{cases} \quad . \tag{5.1}$$

Here I_m denotes the modified Bessel function,

$$I_m(z) = \left(\frac{1}{2}z\right)^m \sum_{k=0}^{\infty} \frac{\left(\frac{1}{4}z^2\right)^k}{k!\Gamma(m+k+1)} \quad , \tag{5.2}$$

of integer order m and $\Gamma(n)$ is the Gamma function given for integer numbers by

$$\Gamma(n) = (n-1)! \quad . \tag{5.3}$$

The parameter m controls the continuity of the function at $r = a$. For $m = 0$ the function is not continuous. For $m > 0$ the function is $m-1$ times differentiable. The support is denoted as a. This allows to calculate the object function f, its radon transform and its derivative in reasonable time. Note that with a larger support the number of pixels affected by one blob function increases accordingly. This results in a less sparse system matrix $\mathbf{M}$. The parameter α tapers the blob. It changes the curvature of the blob at its barycenter. The higher α, the higher the curvature. Figure 5.4 shows a radial profile for different parameters varying in m and α.

In the following we will discuss several properties of the blob function regarding tomographic reconstruction. If differentiability is given for one basis function, the same counts for an ensemble of basis functions due to linearity. It follows that the discretized representation of the object function $f(\mathbf{r})$ in blob basis f_i is likewise continuous and differentiable. This is consistent with the structure of most biological specimen, which usually do not show sharp edges. Figure 5.3 demonstrates this property in an exaggerated example using a low resolution of 32×32 pixels.

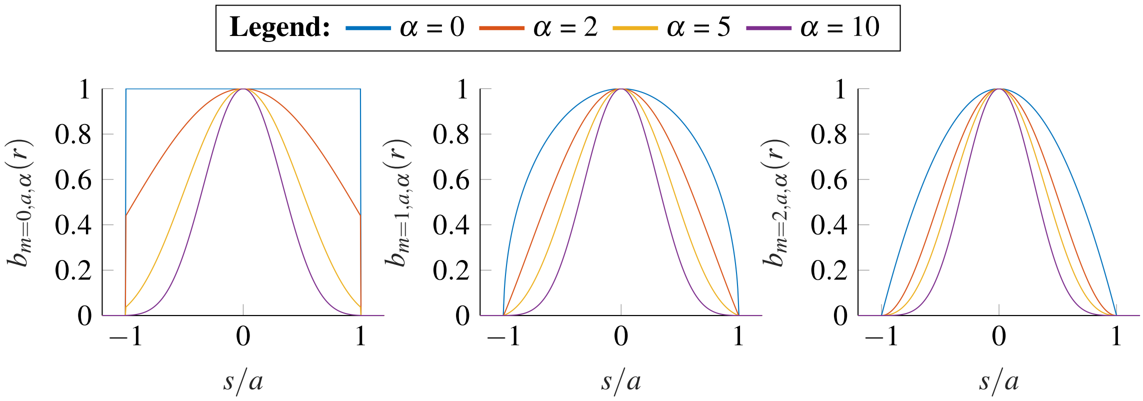

(a) $m = 0$ (b) $m = 1$ (c) $m = 2$

Figure 5.4: Images (a,b,c) show the the radial profiles of the Kaiser-Bessel function for the blob parameter $m = 0$, $m = 1$, and $m = 2$, respectively. Each subfigure comprises plots where the second blob parameter α takes the values 0, 2, 5, and 10.

5.3.1 Footprint

A major advantage of blobs is their rotation symmetry. The projection of a blob on the detector is therefore not dependent on the projection angle, but only on the distance between its center point and the ray of interest. Moreover, analytic expressions for the footprint, its derivative and the Fourier transform can be derived analytically. For Talbot-Lau imaging this is advantageous, since the derivative of the phase-shift can be calculated component wise for each blob due to its linearity [55].

The conventional footprint is given for $\alpha \neq 0$ by

$$p_{m,a,\alpha}(s) = \frac{a}{I_m(\alpha)} \cdot \sqrt{2\pi/\alpha} \cdot \left(1 - s^2/a^2\right)^{m/2+1/4} \cdot I_{m+1/2}\left(\alpha\sqrt{1 - s^2/a^2}\right) \quad , \tag{5.4}$$

and for $\alpha = 0$ by

$$p_{m,a,\alpha=0}(s) = 2a \cdot [2^m m!/(1 \times 3 \times 5 \times \cdots \times (2m+1))] \cdot \left[1 - s^2/a^2\right]^{m+1/2} \quad . \tag{5.5}$$

Likewise, the differential footprint is given for $\alpha \neq 0$ by

$$\frac{\partial p_{m,a,\alpha}}{\partial s}(s) = \frac{-s}{a I_m(\alpha)} \cdot \sqrt{2\pi\alpha} \cdot \left(1 - s^2/a^2\right)^{m/2-1/4} \cdot I_{m-1/2}\left(\alpha\sqrt{1 - s^2/a^2}\right) \quad , \tag{5.6}$$

and for $\alpha = 0$ by

$$\frac{\partial p_{m,a,\alpha=0}}{\partial s}(s) = -\frac{4s}{a} \cdot [2^m m!/(1 \times 3 \times 5 \times \cdots \times (2m+1))] \cdot (m+1/2) \cdot \left[1 - s^2/a^2\right]^{m-1/2} \quad . \tag{5.7}$$

Example images of the conventional and differential footprint for several blob parameters varying in m and α are given in Fig. 5.5 and Fig. 5.6, respectively.

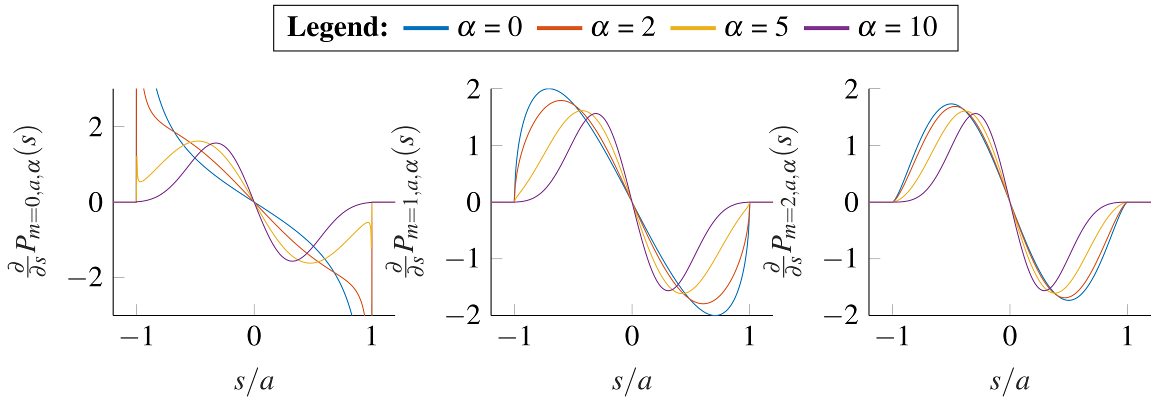

(a) $m = 0$ (b) $m = 1$ (c) $m = 2$

Figure 5.5: The differential footprint of the Kaiser-Bessel function for parameters varying in m and α.

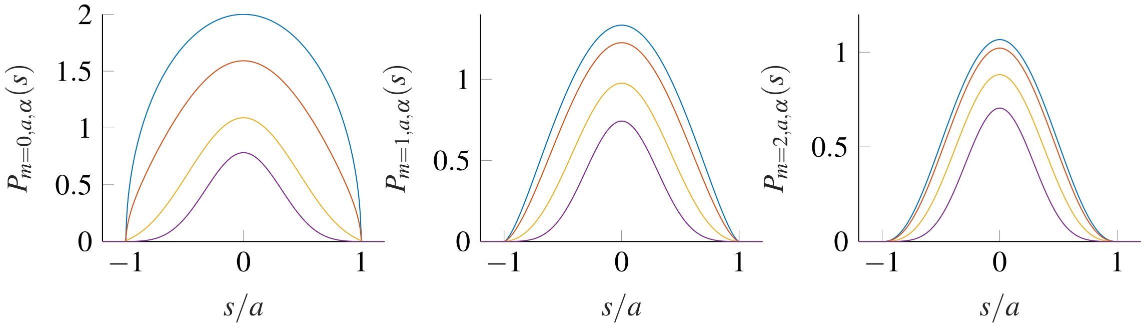

(a) $m = 0$ (b) $m = 1$ (c) $m = 2$

Figure 5.6: The conventional footprint of the Kaiser-Bessel function for parameters varying in m and α.

5.3.2 Calculation of matrix elements

For the non-differential attenuation and scatter images, the weights for the system matrix elements M_{ij} are computed as the integration of the footprint of blob j over the area of detector pixel i

$$M_{ij} = \frac{\int_{s_i}^{s_{i+1}} p_{m,a,\alpha}(s - b_j)\,\mathrm{d}s}{\int_{s_i}^{s_{i+1}} \mathrm{d}s} \quad , \tag{5.8}$$

where s_i denotes the pixels borders and b_j the projection of the blob's center on the detector. This integration is exemplary shown in Fig. 5.7. For the differential matrix elements M_{ij}^{δ}, the integration is performed over the differential footprint

$$M_{ij} = \frac{\int_{s_i}^{s_{i+1}} \frac{\partial}{\partial s} p_{m,a,\alpha}(s - s_j)\,\mathrm{d}s}{\int_{s_i}^{s_{i+1}} \mathrm{d}s} \quad , \tag{5.9}$$

as visualized in Fig. 5.8. The calculation of the system matrix elements differs to the implementation of Wolf [123]. In his work Wolf calculated first the projection of the blob's center on the detector. Subsequently he used the the value of the (differential) footprint at this position as the (differential) system

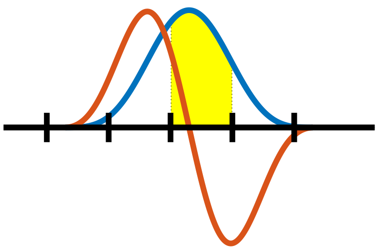

Figure 5.7: Matrix element of the conventional footprint.

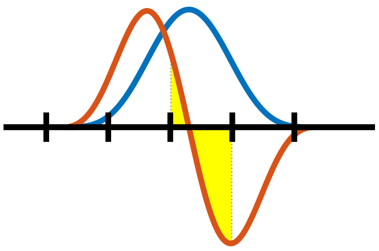

Figure 5.8: Matrix element of the differential footprint.

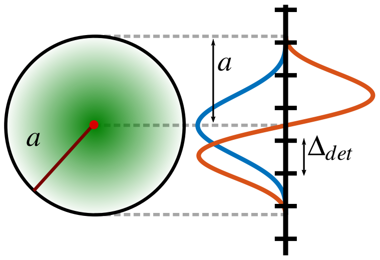

Figure 5.9: One blob functions affects a maximum of $S_{forward} = 2 + \frac{\lfloor 2 \cdot a \rfloor}{\Delta_{det}}$ pixels on the detector.

weight. This is only an approximation of the correct matrix element. Integration via Eqns. 5.8 and 5.9 provides the mathematically correct description of the system matrix elements.

In order to efficiently calculate all matrix elements, the integrals of the footprint and its derivative are precalculated. For the differential case this is given analytically by the radon transform. The integral of the conventional footprint[1] on the other hand can only be calculated numerically. By choosing this implementation method, the integrations of Eqns. 5.8 and 5.9 are no longer required to be performed numerically. Instead of computing the time expensive Riemann sum for each integral, we can simply take the difference of the integral value at the pixel boundaries.

5.4 Implementation of the System Matrix

The system matrix is a linear mapping of the image volume of size $N_{Volume} = N_x \cdot N_y$ onto a set of line integrals of size $N_{Sinogram} = N_{Projections} \cdot N_{Pixel}$. For simplicity we will assume $N_{Grid} = N_x = N_y$. The total number of matrix elements is then given by:

$$N_{total} = N_{Grid}^2 \cdot N_{Pixel} \cdot N_{Projections} = N_{Grid}^2 \cdot N_{Sinogram} \quad , \tag{5.10}$$

Using a typical CT setup with 512 × 512 voxels and 1000 detector pixels with 720 projections the total number N_{total} of required matrix elements is

$$N_{total} = 512^2 \cdot 1000 \cdot 720 = 1.8 \cdot 10^{11} \quad . \tag{5.11}$$

Assuming each matrix element to be stored as a float value, thus four byte per element, $0.8 \cdot 10^{12}$ bytes of system memory would be required. Storing almost 1 TB of memory is obviously infeasible, even if high performance computing hardware is used.

Fortunately, the system matrix is highly sparse: X-rays detected in one detector pixel have interacted with only a tiny fraction of the whole specimen. Exploiting this property, the maximum size of non-zero elements N_{sparse} is then estimated by

$$N_{sparse} = N_{Grid}^2 \cdot N_{Projections} \cdot S_{forward} \quad , \tag{5.12}$$

where $S_{forward}$ is a constant dependent on the reconstruction geometry. It is an upper bound of the number of pixels affected by one basis function of the image grid at a constant projection angle, see Fig. 5.9. If blobs are used, this bound is given by

---

[1] The footprint looks almost like a Gaussian bell. Thus, the integral is similar to the Gaussian error function.

$$S_{forward} = 2 + \frac{\lfloor 2 \cdot a \rfloor}{\Delta_{Det}} \quad , \tag{5.13}$$

where Δ_{Det} denotes the detector spacing and a the support of the blob. Implementation of this sparse matrix format is cumbersome. One cannot simply store the non-zero matrix elements in a large array. All information, i.e. the corresponding voxel element j and specific detector pixel i, would be lost. Thus, this information is required to be saved alongside with each matrix element.

For typical imaging geometries, one has $S_{forward}$ to be roughly 6. For the image geometry of Eqn. 5.11 one now has a maximum number of stored elements N_{max} of

$$N_{max} = 512^2 \cdot 720 \cdot 6 = 1.1 \cdot 10^9 \quad . \tag{5.14}$$

In total, four arrays with roughly 1 billion of entries each, are required to be saved: The standard and the differential weight (as floats) and the respective pixel and voxel index (as integers). With an efficient implementation this could be realized with roughly 12 GB of system memory. This amount of RAM is available in most modern computation hardware. Precalculation of the exact number of necessary system elements is not possible. In our implementation, we therefore preallocate arrays of size N_{total}. The matrix elements are successively calculated and stored in these arrays. After calculation the fill factor is around 95% depending on the used tomographic geometry. Forward and backward projectors are then easily implemented by looping over the respective matrix elements.

5.5 Choice of Parameters

In a discretization based on rectangular voxels one can vary only the grid's spacing. Large voxels reduce noise, but lower the resolution. Vice versa, a small grid spacing provides a large resolution, but the noise is increased. On the contrary, a discretization using blobs has a larger parameter space. Besides the grid spacing Δ, one can vary a, m and α. This problem was extensively discussed by Wolf [123]. He provides a formula to choose an optimal α if a, m and Δ are given. In our implementations we always chose $a = 2 \cdot \Delta$. The optimal α is then calculated by

$$\alpha_{Opt} = \sqrt{(2\pi a/\Delta)^2 - J_{zero}(m/2+m,1)^2} \quad , \tag{5.15}$$

where $J_{zero}(j,k)$ is the k-th zero of the Bessel-function of order j. No JAVA toolboxes have been found to calculate the zero. The Python toolbox *SciPy* allows for calculation of $J_{zero}(j,k)$. These values were taken and stored in a lookup-table for our implementation in JAVA.

Chapter 6

Methods

In the following sections we introduce several preprocessing methods that have been implemented during this thesis.

6.1 Reference Measurement

The reference scan is usually done prior to the actual measurement. Under ideal condition the free-field reference remains constant for any given time. However, due to external influences such as a varying room temperature or heating of the devices the reference images change. Among others, this leads to a drift of the reference phase measured in each pixel as visualized in Fig. 6.2. For tiled-based acquisitions several correction algorithms have been proposed [99, 51].

If not correctly accounted for, this can lead to severe artifacts in statistical grating based tomography. The optimal solution were to perform a reference measurement at each projection angle. Even though this is feasible with the setup at ECAP, the required beam time to perform a single tomographic scan would be disproportional high. As a compromise between beam time and missing information a reference scan is performed every N-projections. Although the time between two reference shots is not too large, phase drifting still occurs. An interpolation between the missing projection angles is therefore necessary. Due to phase-wrapping, the phase-image is not continuous which forbids direct application of standard interpolation techniques. To resolve this, one requires continuous phase-images. In this thesis we have

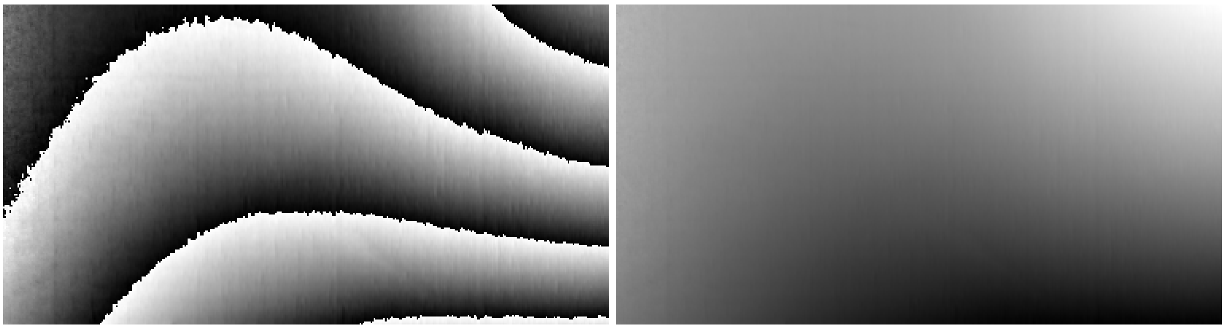
(a) Reference phase wrapped to 2π.
(b) Reference phase unwrapped.

Figure 6.1: Example of 2D phase unwrapping. Data was acquired with the high energy setup at ECAP.

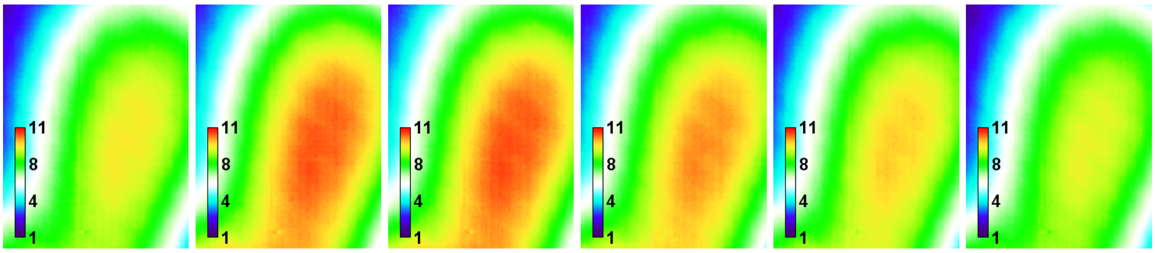

(a) 1/501. (b) 101/501. (c) 201/501. (d) 301/501. (e) 401/501. (f) 501/501.

Figure 6.2: The reference phase images changes over time. In this tomographic scan with 501 projections a reference image was taken every 100 projection angles.

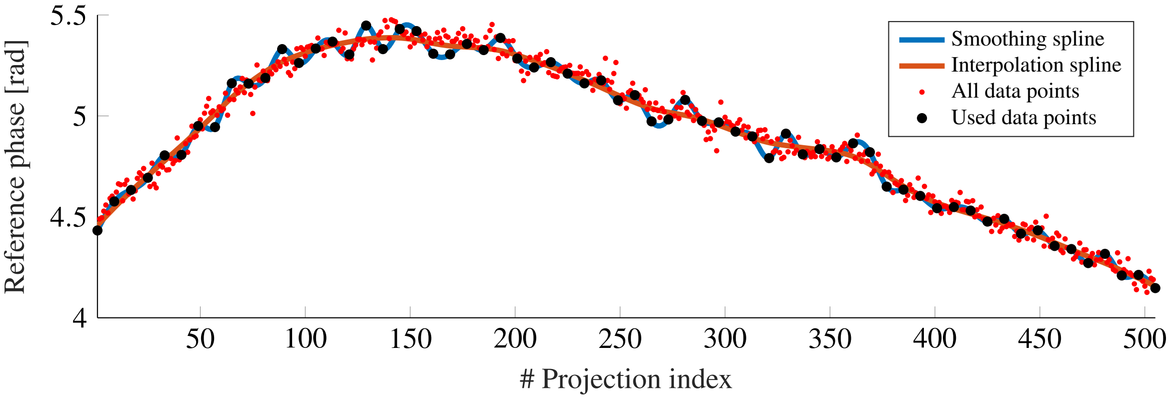

Figure 6.3: Example scans from ECAP to show that the reference phase drifts over time. The red points show the reference phase of a tomographic scan for each projection. In a real tomographic scan only the black data points are measured due to time constraints. Thus, the reference phase between two reference scans must be estimated. Due to noise in the phase, it seems better to estimate this using regression techniques (orange solid line) over interpolation methods (blue solid line).

used a technique proposed by Constantini [24] to unwrap the 2D phase images. Figure 6.1 demonstrates the 2D-phase unwrapping process for data acquired with a phase-contrast setup at ECAP.

After unwrapping the reference images we obtain the time dependence of the reference phase for each detector pixel. Using interpolation or approximation techniques we can estimate the missing information between the reference scans. Due to noise in the phase image we have chosen to use approximation techniques. Implementation, of both approximation and interpolation, was done with the Matlab method "smoothing spline". This methods allows to choose a smoothing parameter p. Depending on the properties of the present problem, such as noise or the amount of phase drift, one has to manually find an optimal p. The whole procedure is visualized in Fig. 6.3.

6.2 Estimation of X-ray Center of Rotation

In state of the art tomographic systems a geometric calibration is essential for an accurate image reconstruction [21, 129]. Here a set of parameters that describe the geometry of such systems are estimated. Calibration is usually done by measuring a well-known three-dimensional phantom composed of a set of easy detectable markers.

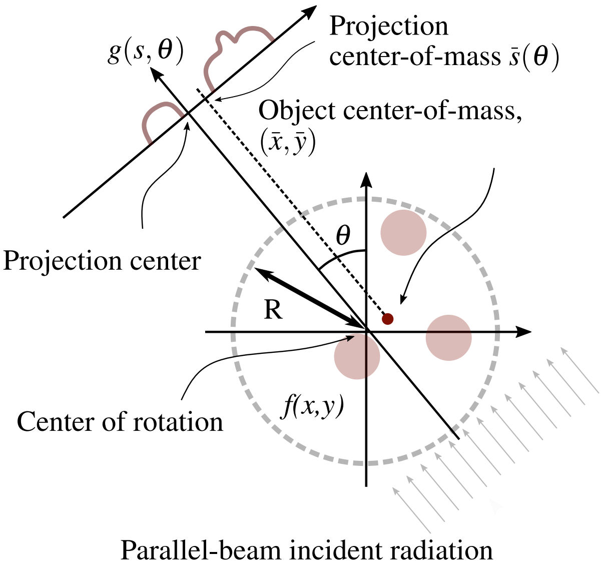

Figure 6.4: The sinogram $g(s,\theta)$ is non-truncated due to the finite extent of the object function $f(x,y)$. The object center-of-mass, $(\bar{x},\bar{y})$ projects on the projection center-of-mass $\bar{s}(\theta)$.

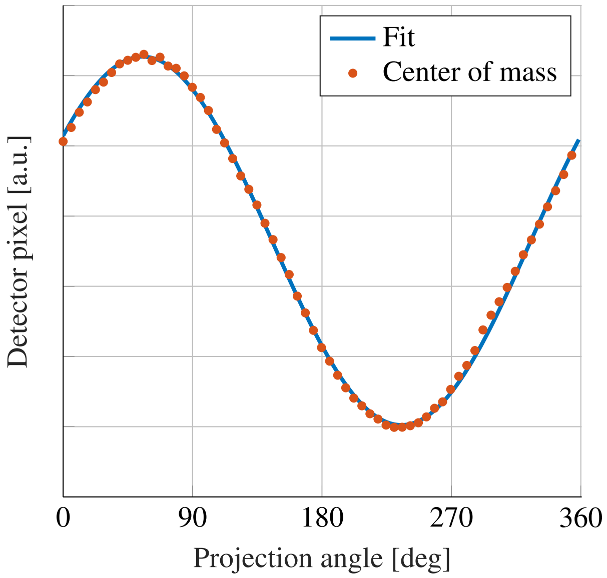

Figure 6.5: The projection center-of-mass is a sinusoidal function of the angle θ. The projection center is subsequently calculated by Least-Square-Estimation. The shown data stem from a tomographic scan performed at ECAP.

These calibration phantoms are not available for the tomographic systems at ECAP. However, if a parallel geometry is present no extensive calibration is required. A parallel beam geometry is valid if the geometric magnification M, defined by the ratio of the source-detector distance and source-object distance, approaches unity [32]. This is only approximately true for the phase-contrast imaging setups at ECAP. However, the objects are small when compared to the actual setup geometry. Consequently, the cone angle is very small which supports the assumption of a parallel beam geometry [32]. For this reason, no advanced geometric calibration is needed.

However, when a tomographic scan is performed, the exact axis of rotation is still unknown. Azvedo *et al.* have proposed a method that can estimate the center of rotation from a tomographic sinogram [4]. This method has been implemented in Matlab. It is then applied to the tomographic data measured at ECAP.

In a tomographic scan the Radon transform $g(s,\theta)$, see chapter 4, is measured as a discretized image given by

$$g_i(\theta) = \int_{s_i}^{s_{i+1}} g(s,\theta)\,\mathrm{d}s \quad , \tag{6.1}$$

where $i = 0,\ldots,(m-1)$ denotes the i-th detector element and m the number of pixels. The location of each detector element s_i is given in detector coordinates by

$$s_i = i \cdot \Delta_s \quad , \tag{6.2}$$

where Δ_s is the detector spacing. By estimating of the center of rotation, we meant to find the location (most probably non-integer) of the projected center-of-rotation, as shown in Fig. 6.4. This location is called the projection center c_s and can be assumed to be constant for all projection angles. The connection between the detector elements' location s_i and the projection space s is then simply given by the translation

$$s = s_i - c_s \quad . \tag{6.3}$$

To estimate the projection center we first need to understand the connection between the centers-of-masses of object and the projections, see Fig 6.4. The object center-of-mass is the two dimensional point $(\bar{x},\bar{y})^T$ where

$$\begin{pmatrix}\bar{x}\\ \bar{y}\end{pmatrix} = \frac{\int\int \begin{pmatrix}x\\ y\end{pmatrix} f(x,y)\,\mathrm{d}x\,\mathrm{d}y}{\int\int f(x,y)\,\mathrm{d}x\,\mathrm{d}y} \quad , \tag{6.4}$$

with the object function $f(x,y)$. The projection center-of-mass $\bar{s}(\theta)$ is given by

$$\bar{s}(\theta) = \frac{\int s\cdot g(s,\theta)\,\mathrm{d}s}{\int g(s,\theta)\,\mathrm{d}s} \quad , \tag{6.5}$$

where $g(s,\theta)$ is the Radon transform, s is the position on the detector, and θ the projection angle. Azvedo *et al.* have proven that for any parallel projection specified by θ, the object center-of-mass always projects onto the projection center-of-mass. With some calculation they express $\bar{s}(\theta)$ in terms of $(\bar{x},\bar{y})^T$.

$$\bar{s}(\theta) = \bar{x}\cos\theta + \bar{y}\sin\theta \quad . \tag{6.6}$$

With this theorem we can track a fiducial point of the object, the center-of-mass, in the projection space. This is done by computing the barycenter for each projection line in the sinogram. However, Eqn. 6.3 tells us that the measured sinogram is translated by the unknown constant c_s. The center-of-mass -is given in detector coordinates via summation to

$$\bar{s}_r(\theta) = \frac{\int s\cdot g(s-c_s,\theta)\,\mathrm{d}s}{\int g(s-c_s,\theta)\,\mathrm{d}s} \quad , \tag{6.7}$$

and simplifies to

$$\bar{s}_r(\theta) = c_s + \bar{s}(\theta) = c_s + \bar{x}\cos\theta + \bar{y}\sin\theta \quad . \tag{6.8}$$

Each projection in the tomographic set is specified by the angle θ_j, where $j = 1,\ldots,N$ is the index of projection. For each projection one can then calculate the projected center-of-mass in detector coordinates

$$\bar{s}_r(\theta_j) = \frac{\sum_i^m s_i\, g(s_i,\theta_j)}{\sum_i^m g(s_i,\theta_j)} = c_s + \bar{x}\cos\theta_j + \bar{y}\sin\theta_j \quad . \tag{6.9}$$

Equation 6.9 gives rise to following equation system

$$\begin{bmatrix} 1 & \cos\theta_1 & \sin\theta_1 \\ 1 & \cos\theta_2 & \sin\theta_2 \\ \vdots & \vdots & \vdots \\ 1 & \cos\theta_N & \sin\theta_N \end{bmatrix} \begin{bmatrix} c_s \\ \bar{x} \\ \bar{y} \end{bmatrix} = \begin{bmatrix} \bar{s}_r(\theta_1) \\ \bar{s}_r(\theta_2) \\ \vdots \\ \bar{s}_r(\theta_{N)} \end{bmatrix} \quad . \tag{6.10}$$

Inversion of this equation system yields the projected center-of-rotation c_s. In Fig. 6.5 we have applied this method for a tomographic scan performed at ECAP using the attenuation sinogram. The orange dots are the projected center-of-mass. The blue curves shows the least square approximation of the equation system 6.10. We want to remark that this tool can be used to see if the tomographic system is well aligned. Imagine that the projected center-of-mass does not form a sinusoidal curve. This can have several reasons. Among those is first that the parallel-beam assumption may not be valid for the imaging setup present. Secondly, the axis-of-rotation may not be aligned at a 90° angle to the detector. Both issues would require further calibration.

6.3 Error Metrics

To evaluate reconstruction results three different error metrics have been used. They will be discussed in the following.

Root-Mean-Square Error

The root-mean-square-error (RSME) is often used to measure the difference between models predicted by a model and the actually observed values. It is given by

$$\mathrm{RMSE}^2 = MSE = \frac{1}{N}\sum_{i=1}^{n}\left(\hat{Y}_i - Y_i\right)^2 \quad , \tag{6.11}$$

where $\hat{Y}$ is a vector of n predictions and Y is the vector of the actual measurement. MSE denotes the mean-square-error.

Peak Signal-To-Noise-Ratio

The peak signal-to-noise ration (PSNR) is the ratio between the maximum possible power of a signal and the power of corrupting noise. It is defined through the RSME via

$$PSNR = 20 \cdot log_{10}\left(\frac{MAX(Y)}{RSME}\right) \quad , \tag{6.12}$$

where $MAX(Y)$ denotes the maximum possible pixel value of the image.

Structural Similarity

The structural similarity is a perceptual metric that quantifies image quality degradation. It is designed to improve on conventional methods such as RSME or PSNR. The SSIM is calculated between a reference image x and a processed image y.

$$SSIM = \frac{(2\mu_x\mu_y)\cdot(2\sigma_{xy})}{\left(\mu_x^2+\mu_y^2\right)\cdot\left(\sigma_x^2+\sigma_y^2\right)} \quad , \tag{6.13}$$

where μ_x and μ_y is the average for the reference x and the processed image y, respectively. σ_x^2 and σ_y^2 denote the variance and σ_{xy} the covariance of x and y.

Chapter 7

Materials

This chapter reviews the materials used throughout this thesis. First, we will discuss the physical setups used for generation of tomographic Talbot-Lau data, before summarizing specimen and their properties for imaging. Subsequently, we shall explain how the wave propagation framework CXI can be used for the simulation of tomographic Talbot-Lau data, and will demonstrate this procedure for one phantom in particular.

Furthermore, a thorough analysis of the reconstruction algorithms requires knowledge of the ground-truth. However, this is not available for real nor simulated data. Therefore we shall clarify how synthetic Talbot-Lau data can be generated applying the proposed forward model. We will then introduce several well-defined phantoms which are used to analyze the reconstruction properties of the proposed algorithms.

7.1 Setup Parameters

7.1.1 High Energy Setup

The tomographic scans performed in this thesis have been acquired with the high-energy setup at ECAP. Its parameters are described in the following. The grating periods, heights and duty cycles are shown in table 7.2. The distances of the gratings, object and detector from the source a given in table 7.1. Within this setup, it is possible to use acceleration voltages between 50 keV and 125 keV with a sufficiently high reference visibility. A Siemens MEGALIX Cat Plus 125/40/90-125GW is used as X-ray source. The detector is a PerkinElmer DEXELA 1512 with 75 µm pixel pitch. The field of view is about 2.9 cm × 6.9 cm. Figure 7.1.1 shows the corresponding energy-visibility curve that is obtained if the setup parameter are input for a wave propagation algorithm.

G_0	7 cm
O	74 cm
G_1	97 cm
G_2	165 cm
D	172 cm

Table 7.1: Distances

	G_0	G_1	G_2
Period [µm]	13.31	5.71	10.0
Height [µm]	220	6.3	220
Duty Cycle	0.5	0.3	0.5
Material	Au	Au	Au

Table 7.2: Grating parameters

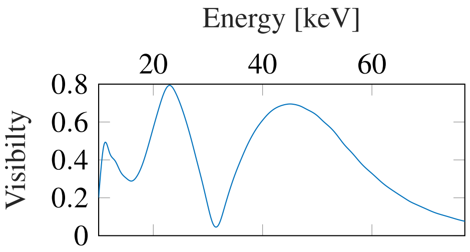

Figure 7.1: Energy-visibilty curve

The setup parameter of the current high energy setup at ECAP. In table 7.1 O and D denote the location of the object and detector respectively.

7.1.2 Setup used by Thomas Weber

In 2015, Weber *et al.* have reported an improved performance in phase-contrast tomography [116]. For their analysis they have imaged a phantom consisting of three different cylinders. In the following we shortly present the used setup. The grating properties and their locations in the setup are given in tables 7.3 and 7.4. The corresponding energy-visibility curve is given in Figure. 7.3. For photon detection, a flat panel detector (Dexela 1512) with a 600 µm CsI conversion layer and 75 µm pixel pitch was used.

G_0	16.5 cm
O	90 cm
G_1	103 cm
G_2	111 cm
D	164 cm

Table 7.3: Distances

	G_0	G_1	G_2
Period [µm]	24.39	2.185	2.4
Height [µm]	180	4.36	90
Duty Cycle	0.5	0.69	0.5
Material	Au	Au	Au

Table 7.4: Grating parameters

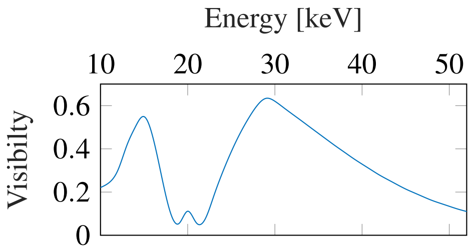

Figure 7.3: Energy-visibilty curve

The setup parameters of the Talbot-Lau inteferometer used in [116].

7.2 Specimen

The major difficulty when performing tomographic measurements with our Talbot-Lau interferometers is the correct alignment of the specimen in the tomographic setup. With a diameter of roughly 2 cm, the field-of-view of the high-energy setup is quite small. This allows the object to have a maximum radius of 1 cm. Thus, the object needs to be perfectly placed in the middle of the rotation center. On first glance, this does not seem to be a big problem. However, due to the small field-of-view a displacement of only 1 mm corresponds already to a relative displacement of 5%. This requires a 10% larger detector. Another problem is the alignment of the rotation axis. The rotations axis needs to be perpendicular to both, the detector and the optical axis. The fine adjustment could be avoided with a geometrical calibration done prior to the measurement. However, this has not yet been implemented for our setups.

For this thesis we have created and measured several phantoms. An overview over the phantoms is given in Fig. 7.5.

The first phantom, see Fig. 7.5a, consists of four cylinders. It is a screw, a cylinder filled with gritty sand, a couple of copper wires piled together to form again a cylinder and last, a cylinder made of foamed plastic with wires of different materials inserted.

Figure 7.5b shows a phantom made of 4 cylinders. One cylinder consists of foamed plastic. Two cylinders are made of PVC and PMMA and have a diameter of 4 mm each. The third cylinder is also made of PMMA, but coated with a 50 µm copper layer.

The phantom shown in Fig. 7.5c is a similar to the previous. It consists of three cylinders made of PMMA with a diameter of 4 mm each. Two of the cylinders are coated with a copper layer of 50 µm and 100 µm respectively. The copper is suppose to sufficiently harden the beam, such that polychromatic artifacts are observed in the phase and scatter image.

The specimen in Fig. 7.5d consists of three cylinders embedded in a plastic glass tube. The first is a syringe filled with a 16% iodine-water solution. The other two cylinders consist of foamed plastic and have different diameter.

Figure 7.5e displays a plastic syringe with an diameter of 1.4 cm filled with the same 16% iodine-water solution. The iodine has a large atomic number and is supposed to harden the beam and thus creates dark-field due to polychromatic effects. Moreover, it would be favorable to have an additional dark-field due to micro-scattering. For this reason, we have coated the iodine solution with a some layers of sand paper, see Fig. 7.5f.

In Fig. 7.5g we have built a phantom with mainly micro-scattering properties. A foamed plastic is put into a glass tube. Two small metal wires with a plastic coat are placed inside the foam. Additionally, we have inserted a plastic cylinder with no material (air). The attenuation of the foam should be small, thus differentiating between air and foam should be hard in the attenuation image. However, the foam should decrease the visibility. Thus, one would expect to differentiate foam and air easily in the scatter image. Due to its resemblance to a drawing of a face, it is henceforth called the smiley phantom.

A phantom made of four cylinders is depicted in Fig. 7.5h. The materials are aluminum ($r = 4mm$), copper($r = 4mm$), brass ($r = 3mm$) and steel ($r = 1.5mm$). Due to the large atomic numbers heavy beam hardening artifacts are expected.

The next phantom, see Fig. 7.5i, is a biological sample of a pig femur. The bone exhibits a small fissure, which is barely visible in radiographic images. One hopes to gain more information on the fissure from a tomographic scan. Moreover, this is a formidable opportunity to test the proposed algorithms with a biological specimen.

The last phantom, shown in Fig. 7.5j is an aluminum tube. It has an outer diameter of $d_{out} = 1.5\,\text{cm}$ and an inner diameter of $d_{in} = 0.5\,\text{cm}$. The aluminum is supposed to sufficiently harden the spectrum, such that beam-hardening artifacts in the attenuation and scatter image are observed.

7.3 Wave Propagation Simulation

The framework CXI developed at ECAP allows to simulate Talbot-Lau phase-stepping data [93]. By providing a material distribution to the framework, the complex refractive indexes at any energy are given by literature values. For known setup parameters, CXI subsequently performs a wave propagation which results in phase-stepping data. However, CXI calculates only the phase-stepping data in one pixel. To simulate a whole detector row this calculation has to be repeated for each detector pixel. Moreover, a tomographic scan requires simulation of the whole detector row from all angular positions. This demands a high computational effort. For this reason a small framework to simulate a tomographic scan has been

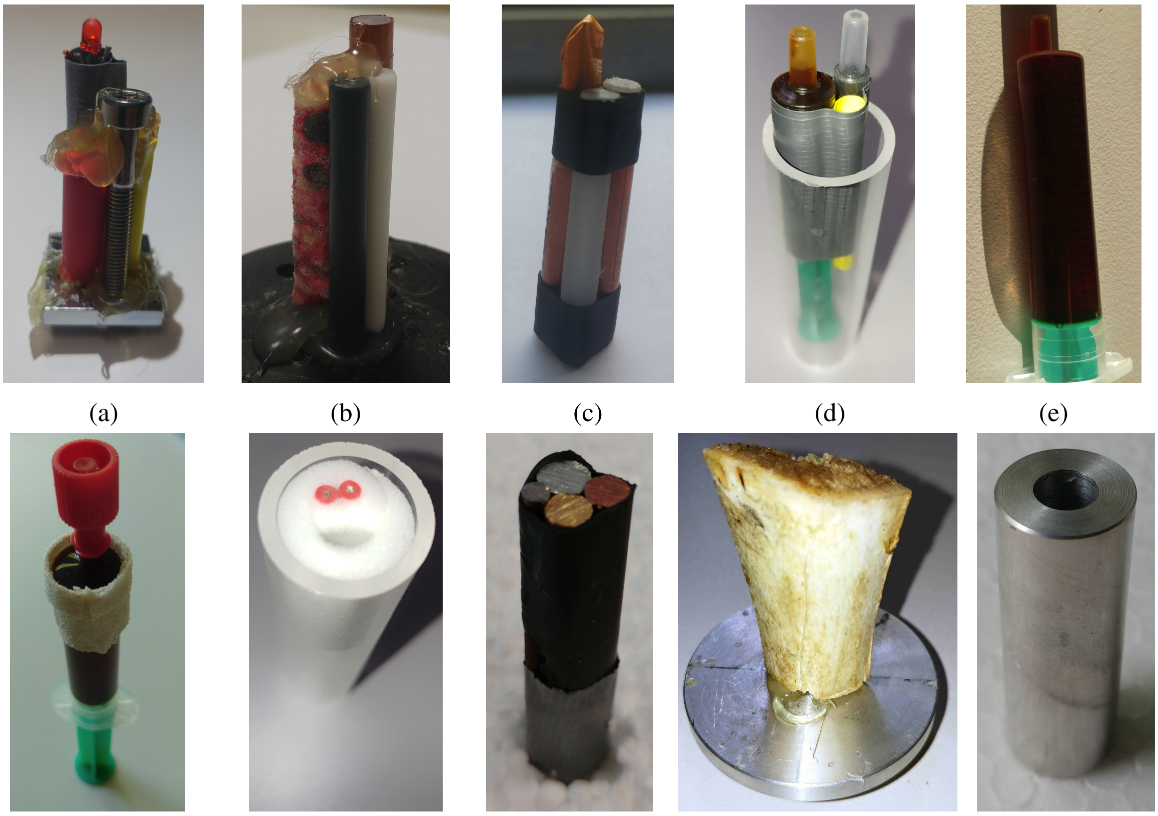

(a) (b) (c) (d) (e)

(f) (g) (h) (i) (j)

Figure 7.5: An overview of the specimen that have been imaged throughout this thesis.

developed. It utilizes the processing power of the high performance cluster to simultaneously perform the wave propagation on many computing nodes. With this framework the tomographic simulation can be performed in reasonable time.

No tomographic Talbot-Lau data stemming from a real setup has been available in the first months during development of the reconstruction framework. To test our algorithms we have therefore relied on tomographic data obtained by CXI. In the following we introduce the used phantom:

The phantom consists of a cylinder filled with water and has a radius of 5 mm. Inside this cylinder there are several small objects. The two bigger spheres with a radius of 1 mm are made of PVC. The ellipsoid is made of PMMA. The remaining spheres are made of Teflon They have radii of 200 µm and 150 µm. On the right there are many densely packed spheres made of Teflon with radius of 75 µm. They are supposed to create a homogeneous dark-field.

The simulation was done mono-chromatically at an energy of 50 keV. The detector consists of 256 pixel and has a pixel pitch of 40 µm. The grating periods are $g_0 = 2.5\,\mu\text{m}$, $g_1 = 5\,\mu\text{m}$ and $g_2 = 2.5\,\mu\text{m}$. The phase-grating was $\pi/2$ shifting and the detector was placed directly after G_2. The analyzer grating was placed at the first fractional Talbot order at 37.8 cm. A tomographic scan over 360° was performed with an angular step of 1°. Due to the parallel geometry the exact location of the object does not influence the simulated result.

In Fig. 7.6 the ground truth data of the complex refractive index is visualized. Moreover, the filtered back projection results of the simulated Talbot-Lau data are shown as well. The attenuation and phase image looks like the the ground truth, however small streak artifacts are visible which are probably due

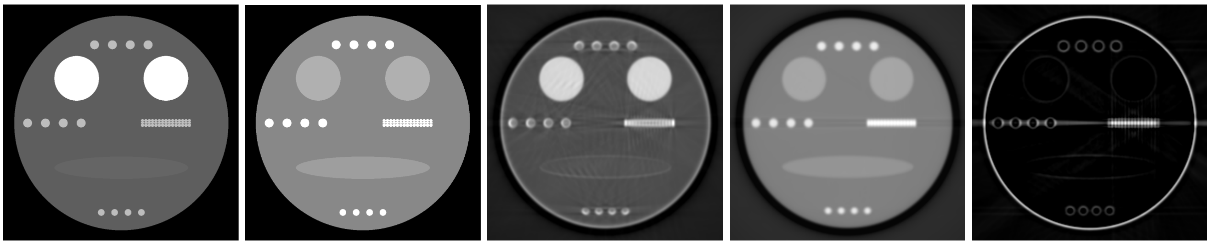

(a) Ground truth μ (b) Ground truth δ (c) FBP μ (d) FBP δ (e) FBP σ

Figure 7.6: The shown phantom was used to simulate Talbot-Lau data with the wave propagation simulation CXI. On the left is the ground truth data known by literature. On the right are shown tomographic reconstruction done with filtered back projection on the noise free image. Note that the scatter image yields non-zero entries which stems from edge-induced dark-field.

to discretization artifacts. Moreover, intensity in the scatter image occurs due to dark-field induced by the object's edges.

As a matter of fact, Talbot-Lau data simulated with CXI are inherently noise free. The phase-reconstructed sinograms are shown in the first row of Fig. 7.7. The simulated phase-stapping data can be augmented with Poisson distributed noise to account for a realistic environment. An example of simulated data corrupted by noise is shown in the second row of Fig. 7.7.

7.4 Phantom Data using Forward Model

In order to analyze properties of an algorithm it is favorable to have ground truth data. This allows to calculate error metrics such as RSME or PSNR, see also section 6.3. Ground-truth data are not available for real Talbot-Lau data. Theoretically, if the exact material decomposition were known, one could take the refractive index given by literature. Unfortunately, for real data this can not be determined within feasible effort. But still, exact knowledge of attenuation and refractive decrement would not suffice as ground truth data: The scattering coefficient can not be inferred from this because it depends on the object's micro-structure. For this reason ground truth data are also not available for simulated data using a wave propagation algorithm such as CXI.

One can circumvent this problem by applying the forward model to a well-defined phantom. The provided phase-stepping data can then be reconstructed and the well-defined phantom serves as the ground-truth. In doing so, one can freely choose the spacing and resolution of the reconstructed volume and detector. Also, wee can simulate any reference visibility and sensitive. Furthermore, we can set the number of reference photon counts seen per pixel. By adding e.g. Poisson distributed noise we can simulate noisy image data.

Different phantoms have been implemented during this thesis to analyze properties of the reconstruction algorithm. Furthermore, we have rebuilt a couple of real specimen inside of our reconstruction framework for a better understanding of discrepancies between the physical model and real data.

In particular, our phantoms are defined as follows: A specific element or material, like water or Teflon, is assigned to each pixel in the reconstructed volume. For any energy E of interest the attenuation coefficient $\mu(E)$ and refractive decrement $\delta(E)$ in one voxel element is then given by literature, see [13]. The scatter coefficient is chosen to have meaningful values and depends on what we are interested to image. E.g., if we set $\sigma = 0$ we inherently assume this region of the object to be homogeneous. A coefficient $\sigma > 0$ would then represent an object with micro-scattering properties, such as foam, sponges or lung tissue. Too

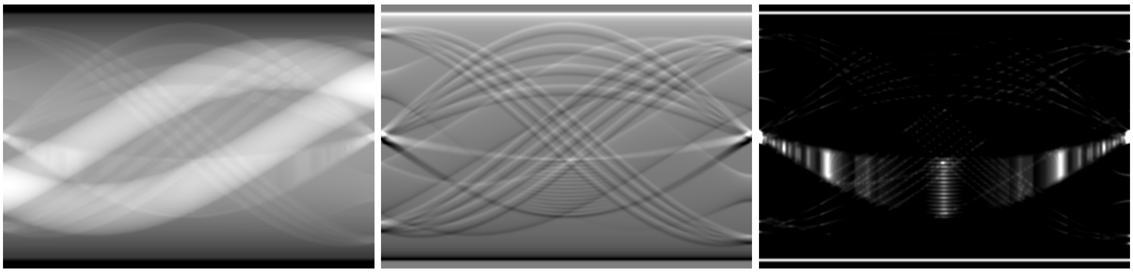

(a) Absorption (noise free) (b) Phase (noise free) (c) Dark-field (noise free)

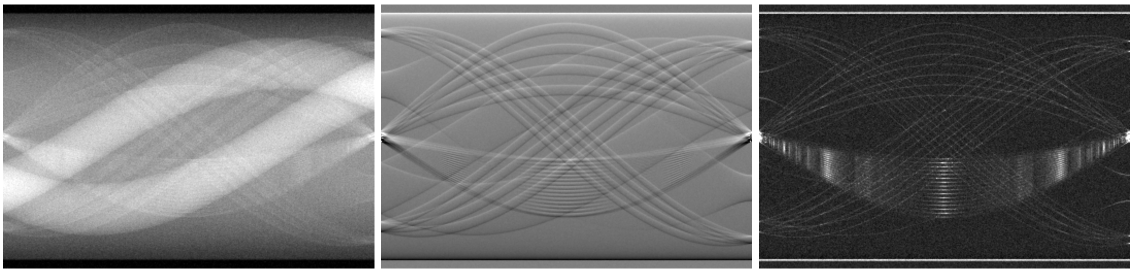

(d) Absorption (Poisson noise) (e) Phase (Poisson noise) (f) Dark-field (Poisson noise)

Figure 7.7: The figures show the phase-reconstructed sinograms of the Talbot-Lau data that were simulated using CXI. The simulated object is shown in Fig. 7.6. Figures (a-c) are noise free sinograms. Figures (d-f) are reconstruction after Poisson distributed noise was added to the simulate phase stepping data. Due to the small dimensions of the object, noise in the phase image is smaller than in the absorption image. Note that discretization artifacts due to the simulation in CXI are visible in the phase and scatter image.

large values will immediately lead to a saturated dark-field, while too small will not lead to any visibility drop at all.

The following introduces three well-defined phantoms that were used for numerical analysis throughout this thesis.

Three Cylinder Phantom

We defined a numerical phantom consisting of three cylinders of different material each, see Fig. 9.20. The largest cylinder is filled with H_2O and has radius of 17.5 mm. The second cylinder has a radius of 13.5 mm and is filled with PTFE. The smallest has a radius of 12.5 mm and contains PMMA. The attenuation coefficient μ and refractive decrement δ are taken from tabulated values [13]. For our synthetic phantom, we choose $\sigma(\mathrm{PMMA}) = 20$, $\sigma(\mathrm{PTFE}) = 14$, and $\sigma(\mathrm{H_2O}) = 8$ at a mean energy of $E_0 = 38.8\,\mathrm{keV}$.

Shepp-Logan Phantom

The second phantom is the well-known Shepp-Logan phantom. A material decomposition of the Shepp-Logan phantom is not given in literature. For this reason each intensity region of the Shepp-Logan phantom was assigned to a specific material. The outer shell is assigned to typical bone material. The inside regions are typical material compositions for soft tissue.

Coefficients for the scatter image are not given by literature, thus they need to chosen manually to take physical meaningful values. Particularly, we assume soft-tissue to have no micro-scattering components, such that its scatter coefficient is set set to zero. Example images an energy of $E = 50\,\mathrm{keV}$ are given in Fig. 7.9.

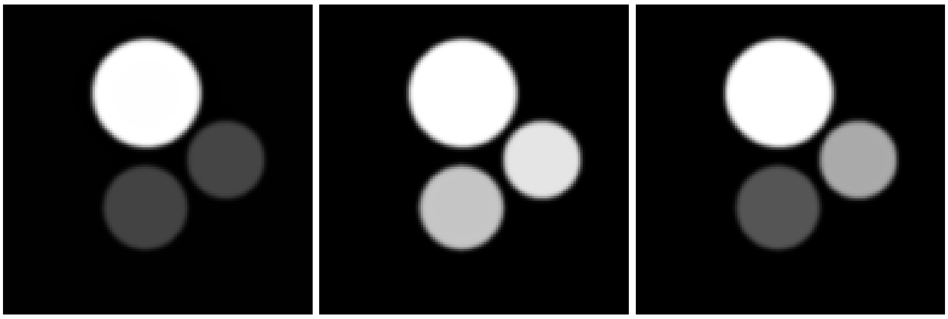

(a) Attenuation μ (b) Phase δ (c) Scatter σ

Figure 7.8: Three cylinder phantom used to generate Talbot-Lau with the proposed forward models. The cylinders contain water (upper left), PMMA (lower left) and Teflon (right).

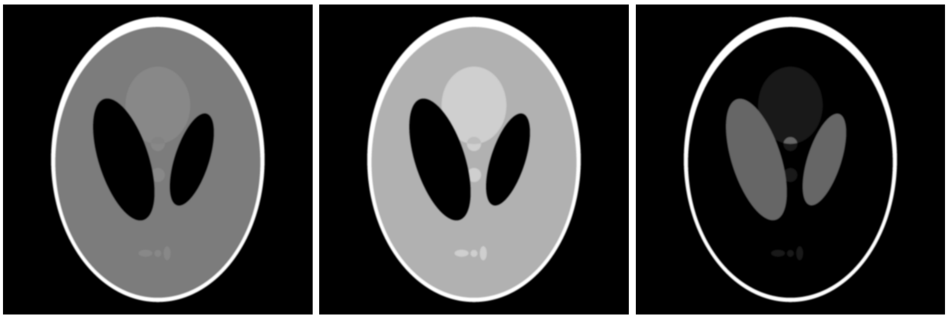

(a) Attenuation μ (b) Phase δ (c) Scatter σ

Figure 7.9: Each intensity in the Shepp-Logan phantom is assigned to a specific material. The complex refractive index is then given by literature. The image for scatter coefficient was chosen to have physically meaningful values.

Mouse Sample

The caveat with the cylinder and Shepp-Logan phantom introduced above, is that no literature values are known for the scatter coefficient. Moreover, the phantoms have a very simple geometry and might therefore favor certain reconstruction algorithms. For this reason it would be advantageous to have a phantom that provides realistic features for all three images.

In order to achieve this, we have created a phantom from tomographic data obtained by a prior reconstruction of a real biological sample. Images for μ, δ, and σ of a mouse are retrieved via filtered back projection since full phase-stepping data have been available [114]. Subsequently, tomographic images were retrieved using filtered back projection. However, severe ring artifacts are present in the reconstructed image. For this reasons, we have applied a ring artifact correction algorithm proposed by Kyriakou *et al.* [56]. Example images of the pure filtered back projection and the ring-artifact corrected images are shown in Fig. 7.11.

The phantom yields indeed complementary information. High scatter coefficients arise e.g. inside pulmonary tissue where one has no image signal in neither the attenuation nor the phase image.

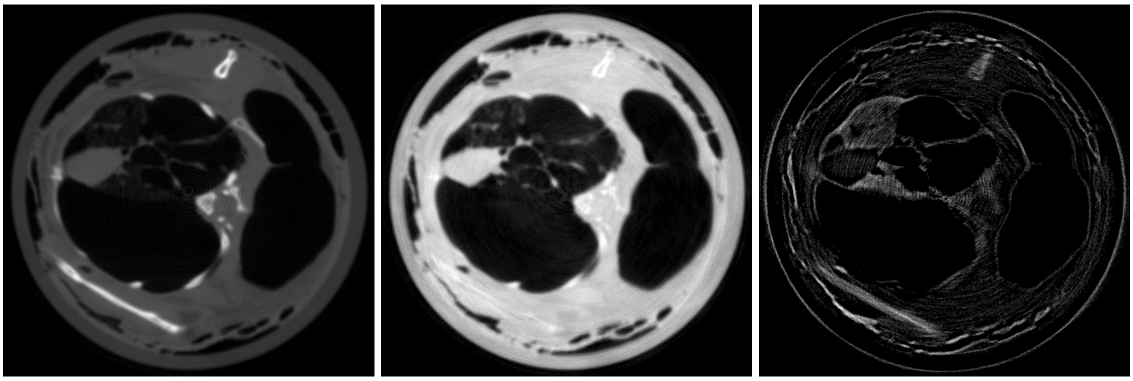

(a) Attenuation μ (b) Phase δ (c) Scatter σ

Figure 7.10: Filtered back projection of the mouse sample sinograms. All three images show severe ring artifacts.

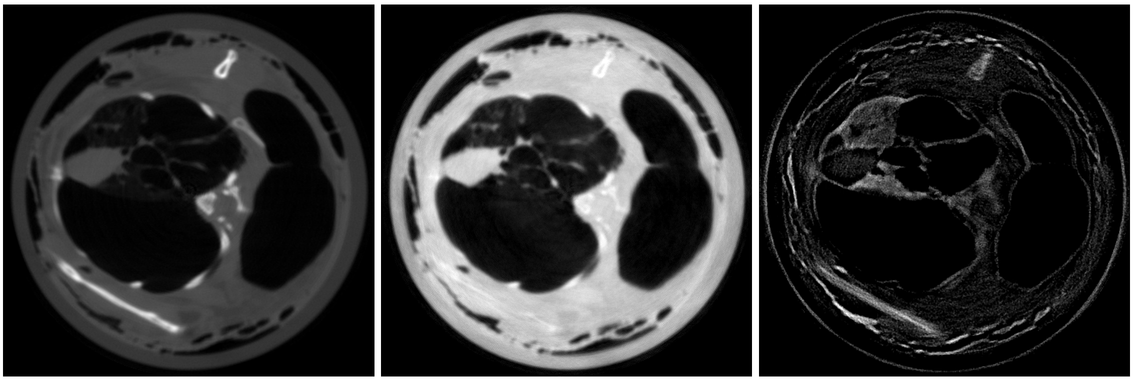

(a) Attenuation μ (b) Phase δ (c) Scatter σ

Figure 7.11: Tomographic Talbot-Lau reconstruction after a ring artifact correction algorithm was applied. The ring artifacts are reduced.

Chapter 8

Contributions

An overview over tomographic reconstruction techniques and their application to grating-based X-ray imaging was given in chapter 4. Ritter *et al.* were the first to investigate a maximum-likelihood algorithm to simultaneously reconstruct attenuation, phase and scatter images without requiring phase retrieval [92, 94]. In subsequent work, Brendel *et al.* added regularization techniques to the algorithm and showed first reconstruction results on biological data. Wolf compared several projector operators and their influence on the reconstruction result [123]. He additionally tried to enhance the imaging model using the so-called complex dark-field contrast. All proposed algorithms assume monochromatic radiation and can not cope with polychromatic data. Additionally, slow convergence for the phase-image was reported [19, 94]

In this thesis, two major advances for Talbot-Lau X-ray tomography are developed. Our key contribution is to extend the monochromatic forward model to polychromatic data. The main benefit of the enhanced model is that beam-hardening artifacts are implicitly dampened or even completely removed. Secondly, we try to tackle the problem of slow convergence of the phase-image. For this, we propose and evaluate an advanced reconstruction technique exploiting information of the second derivative.

In this chapter we first review the state of the art regarding statistical grating-based tomographic reconstruction in more detail. Subsequently, a polychromatic forward model is introduced. We then derive how tomographic reconstruction can be done using this model. Last, we propose an optimized reconstruction algorithm.

8.1 State-of-the-Art

In this section we will give a short overview over the state of the art investigating statistical grating based tomography without phase-retrieval.

Statistical reconstruction without Phase-Retrieval

Ritter *et al.* were the first to introduce a maximum likelihood reconstruction for simultaneous grating-based tomography. They have used a system matrix approach to implement the forward and back projector. The matrix elements have been calculated using Siddon's method [100].

No experiments with real data have been published. Instead, they have used a wave propagation simulation [92] to obtain Talbot-Lau imaging data. Both radiographic data as well as the reconstructed data had a very low spatial resolution of 90 detector elements and 90×90 voxels, respectively. The proposed reconstruction algorithm was able to reconstruct the attenuation and the phase image which was given as

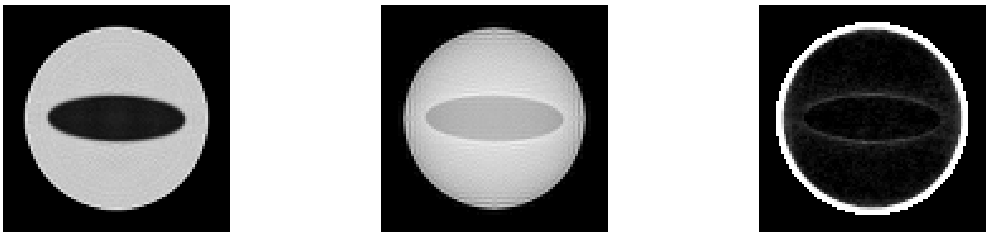

(a) Attenuation μ. (b) Refractive decrement δ. (c) Scatter σ.

Figure 8.1: Example reconstruction from Ritter *et al.* [92]. Talbot-Lau data were obtained using a wave propagation simulation. 360 projections with 90 detector pixels have been simulated where four phase-steps per projection have been performed. The reconstruction image resolution is 90 × 90 voxels.

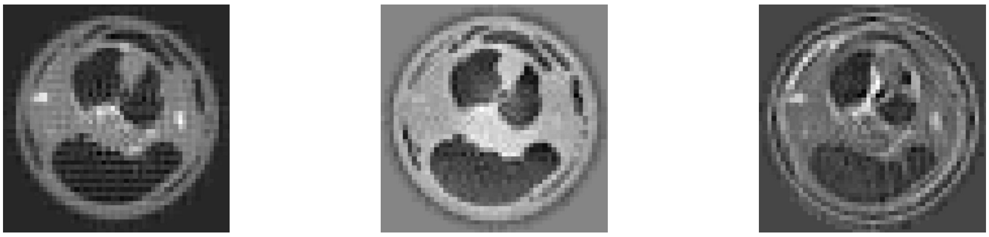

(a) Attenuation μ. (b) Refractive decrement δ. (c) Scatter σ.

Figure 8.2: Example reconstruction from the second publication of Ritter *et al.* [94]. Talbot-Lau data were obtained at ECAP with 601 projections over 360°. The detector resolution has been 67 pixels where eight phase-steps per projection have been performed. The reconstructed image had a resolution of 51 × 51.

input to the wave-propagation algorithm. Since the objects are assumed to be homogeneous, a dark-field signal occurs only at the edges of the object [124]. This propagates then into the reconstruction of the scatter image. The reconstruction results are shown in Fig. 8.1.

In subsequent work Ritter *et al.* have published reconstruction results of a mouse sample, see Fig. 8.2. Data was obtained with a Talbot-Lau interferometer at ECAP. For the tomographic scan, 601 projections with 67 pixels each have been acquired over 360°. At each projection, eight phase-steps have been measured over an interval of 2π. The image resolution was 51×51. Additionally, a concise convergence analysis of the proposed algorithm was given. However, due to the low spatial resolution these results should be interpreted with caution, as they may not generalize to high resolution data due to discretization artifacts.

Statistical reconstruction without Phase-Retrieval using Regularization

Brendel *et al.* have augmented the cost function of Ritter *et al.* with regularization techniques [19, 92]. In their work they demonstrated that the image quality of statistical reconstruction was significantly increased over filtered back projection algorithms requiring prior phase-retrieval. They have been the first to apply statistical grating-based tomography on real data. For this they have used tomographic data of a biological mouse sample, see Fig. 8.3. The phase-stepping data were acquired with synchrotron radiation [106]. Additionally, they have been the first to show that reconstruction using the interlaced acquisition scheme is feasible [127]. To the best of our knowledge, a standard forward projector with numerical differentiation has been used.

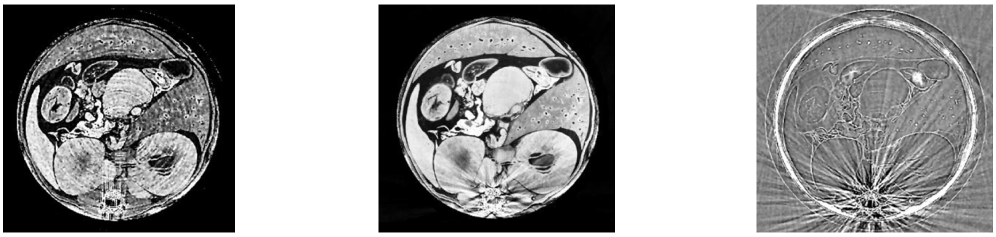

(a) Attenuation μ. (b) Refractive decrement δ. (c) Scatter σ.

Figure 8.3: Example reconstruction from Brendel *et al.* [19]. Talbot-Lau data of a mouse was obtained using a synchrotron light source. 901 projections over 360° with 4 phase-steps per projection have been measured.

Evaluation of the Choice of Projector and Back Projection Implementation

Andreas Wolf has investigated the influence of different implementations of forward projectors [123]. For his experiments he has used two data sets: First, monochromatic Talbot-Lau data were simulated using a wave propagation algorithm [93]. Second, real images of a physical phantom were measured at ECAP.

In contrary to the synchrotron data used in the experiments of Brendel *et al.*, these data were obtained with a conventional X-ray tube.

He developed the reconstruction framework in the programming language *Python*. For optimization of the likelihood he used an implementation of the conjugated gradient method provided by the *Python* package *SciPy* [47]. Its implementation is not optimized for tomographic reconstruction. For this reason reconstructions with a resolution exceeding 60×60 can not be obtained within reasonable time. In Fig. 8.4 example reconstructions are given for a physical phantom consisting of three cylinders made of PTFE, PVC and PMMA. Iterative reconstruction using three different projectors (Siddon [100], distance-driven [63] and blobs [58]) were compared to filtered back projection results. Wolf found that the blob projectors provided the best results regarding noise and other artifacts.

However, these results should be interpreted with caution since the reconstruction resolution has been very small. In particular, there is reason to believe that differences between the actual implementation of the forward projectors become negligible for high image resolutions. The good performance of the blobs in the work of Andreas Wolf might be explained by strong discretization artifacts exhibited by the Siddon and distance-driver projector since extremely small image resolutions were used.

8.2 Polychromatic Forward-Projection and Reconstruction

In contrast to the last section, where an overview over the current state of the art was given, the following sections now present the contributions of this thesis to the progress of science.

Talbot-Lau imaging with a conventional X-ray tube suffers from polychromatic artifacts. These stem from two energy dependent factors: the energy-dependent material coefficients and, specific to Talbot-Lau interferometers, the energy-dependence of the interferometer - which includes reference photon counts, phase and visibility - itself.

In tomographic reconstruction of the attenuation and refractive decrement, beam hardening and dispersions effects degrade the image quality. Beam hardening describes the effect that as the mean energy of the propagating X-ray beam shifts to higher energies, the larger the attenuation - see Fig. 8.5. It is due to energy dependence of the attenuation coefficient according to Eqn. 2.15. This has severe consequences for the dark-field image. The interferometer's visibility is highly dependent on the spectrum. Let us assume

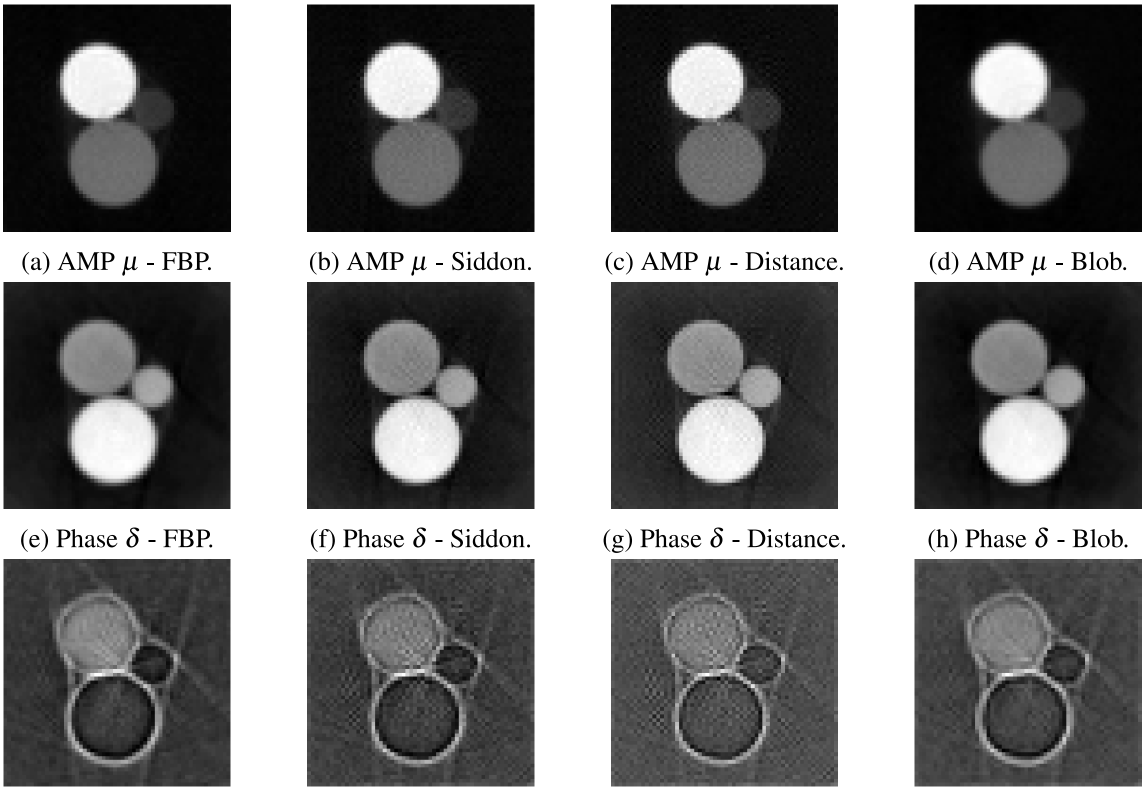

(a) AMP μ - FBP. (b) AMP μ - Siddon. (c) AMP μ - Distance. (d) AMP μ - Blob.

(e) Phase δ - FBP. (f) Phase δ - Siddon. (g) Phase δ - Distance. (h) Phase δ - Blob.

(i) Scatter σ - FBP. (j) Scatter σ - Siddon. (k) Scatter σ - Distance. (l) Scatter σ - Blob.

Figure 8.4: Tomographic reconstruction examples of the work of Andreas Wolf [123]. Talbot-Lau data of a physical phantom containing PTFE, PVC and PMMA were measured at ECAP with a conventional X-ray tube. The reconstructed resolution is 60×60 voxels.

that the shape of the spectrum changes due to beam hardening effects. The new spectrum yields a different reference visibility compared to the unperturbed spectrum. Consequently, a dark-field signal arises due to reduction or enhancement in reference visibility which can not be accounted for without prior knowledge. Note that this dark-field is purely due to polychromatic artifacts and not due to micro-angle scattering properties.

Dispersion is a similar effect. However, here we are not interested in the attenuation of the beam, but in the refraction of the beam. The angle of refraction is given via the energy dependent refractive decrement δ introduced in Eqn. 2.13. Thus, the location of the Talbot pattern is dependent on the photons' energy. Eventually, the detector can measure only the superposition of the individual components. The measured Talbot-pattern is smeared out. This leads to image degradation in the measured differential phase and, more interestingly, also to a decrease in visibility when sampled with the analyzer grating. A schematic example of the dispersion effect is given in Fig. 8.6.

In conclusion, both beam hardening and dispersion lead to a decrease in visibility, see also chapter 3. This means that a dark-field signal may be observed purely due to the polychromatic character of the radiation. However, in radiographic X-ray dark-field imaging or tomographic reconstruction of the scatter coefficient one seeks to image only the small-angle scattering properties of the object since this is the valuable information. For this reason the phase-contrast imaging community is required to come up with solutions to reduce polychromatic artifacts.

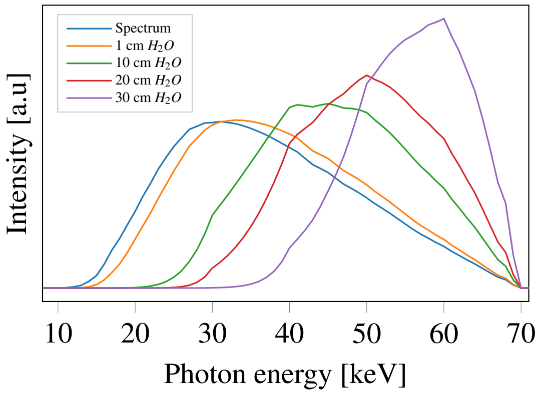

Figure 8.5: A spectrum propagating through water. Low-energy photons are more likely to be absorbed while high energy-photons will pass through. The mean energy of the beam shifts the further it propagates into water. It follows that beam-hardening becomes an issue for highly absorbing objects. Each spectrum is normalized to 1 for better visualization.

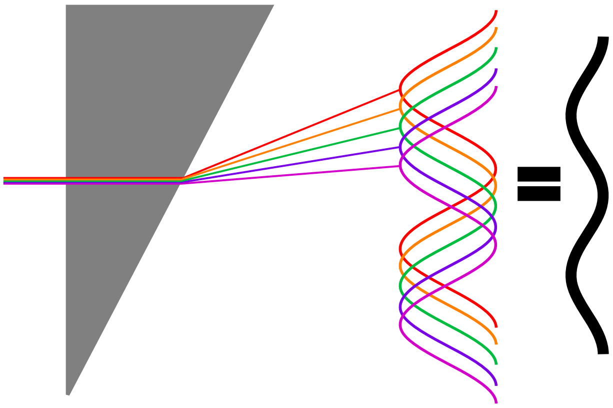

Figure 8.6: X-rays of different photon energies experience a different angle of refraction due to dispersion. The location of the Talbot-pattern depends therefore also on the angle of refraction. The observed Talbot-pattern is therefore a superposition of the individual components. If the shift between the individual Talbot pattern is large the total Talbot pattern is smeared out. The visibility decreases and a dark-field signal appears purely due to dispersion effects.

In this thesis we try to tackle this problem by a polychromatic modeling of the Talbot-Lau image process. We will first introduce and motivate this model in more detail. Afterwards, we discuss how this model is embedded in the reconstruction framework introduced in chapters 4 and 5.

8.2.1 A Physical Forward Model with Energy Dependence

The physical model needs to be carefully chosen. On the one hand, a more expressive model allows a more accurate physical interpretation of the data. On the other hand, the model has to remain manageable for the reconstruction algorithm to achieve convergence. The proposed model presents a tradeoff between these two aspects.

The desired result of tomographic reconstruction is the material distribution of a specimen. In the case of Talbot-Lau tomography, this material distribution has to be inferred from attenuation, refractive decrement and scattering properties. To allow for the avoidance of polychromatic artifacts, we define the measured quantities in dependence of the energy.

As a starting point, we review established models for absorption, phase, and scatter per energy for a Talbot-Lau interferometer [23, 22, 14]. In the energy range between $E = 5\,\mathrm{keV}$ to $E = 120\,\mathrm{keV}$, the energy-dependent linear attenuation coefficient $\mu(E)$ are decomposed approximately into the photoelectric cross-section and the Compton scatter, see Eqn. 2.15. Here we ignore K-edge effects, which is valid for biological tissue in the energy range of interest [14, 21].

The differential phase shift $\phi(E)$ of an X-ray with energy E propagating through matter is given by the energy dependent adaption of Eqn. 3.10 to

$$\Delta\phi(E) = \frac{hc}{2\pi E}\frac{\partial}{\partial x}\phi(E) = \frac{\partial}{\partial x}\int_l \delta(E)\,\mathrm{d}l \quad . \tag{8.1}$$

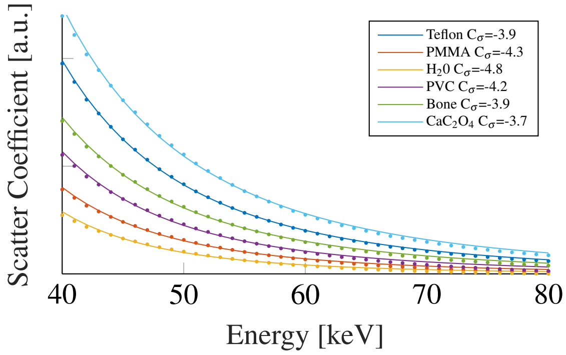

Figure 8.7: Simulation results for the scatter coefficient of different porous materials.

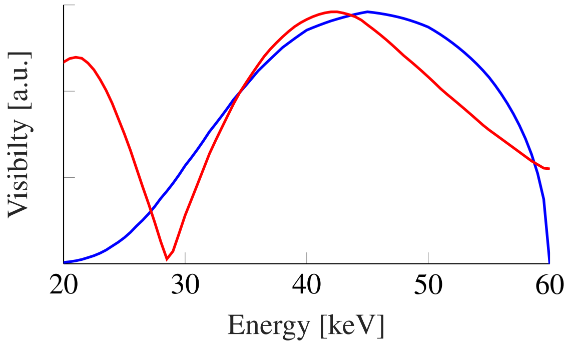

Figure 8.8: Blue: X-ray spectrum scaled to arbitrary unit for better visualization. Red: Simulated visibility of a grating interferometer as a function of the photon energy.

To our knowledge, there exists no full theoretical model for the energy-dependence of the scatter coefficient σ. Following the work by Bech *et al.* [7], we model the scatter coefficient analogously to the attenuation coefficient.

However, it turns out that a full model in the sense of Eqn. 2.15 and Eqn. 8.1 is challenging to reconstruct. Thus, to keep the model manageable, energy dependence is approximated using monomials for each coefficient μ, δ, σ by defining

$$\mu(E) = \mu(E_0) \cdot \left(\frac{E}{E_0}\right)^{C_\mu} \quad , \tag{8.2}$$

$$\delta(E) = \delta(E_0) \cdot \left(\frac{E}{E_0}\right)^{C_\delta} \quad , \tag{8.3}$$

$$\sigma(E) = \sigma(E_0) \cdot \left(\frac{E}{E_0}\right)^{C_\sigma} \quad . \tag{8.4}$$

Here, the material coefficients $\mu(E_0), \delta(E_0), \sigma(E_0)$ are assumed to be known at a given energy E_0 and then extrapolated to arbitrary energies E. The exponents are set to $C_\mu = -3$, $C_\delta = -2$ according to physical properties described in Eqns. 2.15 and 2.13. Doing so, we considered only the first term in Eqn. 2.15 and omitted the energy-dependence of the Klein-Nishina approximation.

The energy dependence of the scatter coefficient is not yet fully explored. While attenuation and phase-sensitive imaging can be explained by material properties, the linear scatter coefficient also depends on the actual setup parameters. We use the wave propagation algorithm of [80, 93] to simulate the scatter coefficient at different energies for several porous materials. To model structures varying in the sub-pixel range, close-packing of spheres with a maximal granular size of 6 µm were generated. The complex refractive decrement for each materials was then assigned to values known by literature [12]. For each material the simulation was repeated 25 times to minimize statistical fluctuations. Sample results from these simulations are shown in Fig. 8.7 for the high energy setup introduced in Sec. 4.3. The exponent C_σ is obtained by least-square fitting of the simulated data to Eqn. 8.4. The simulation indicates that the energy dependence for different materials might be approximated with a monomial, but the exponent varies highly with the material. However, the fitted data are located roughly around $C_\sigma \approx -4$, which is used henceforth.

8.2.2 Reconstruction Framework

We propose an adaption to the iterative maximum-likelihood reconstruction algorithm chapter 4 to Talbot-Lau data corrupted by polychromatic artifacts. For this, a polychromatic modeling of the imaging process is required.

Polychromatic Talbot-Lau Image Model

For a given energy, the transmission T_i, dark field D_i and object phase-shift ϕ_i seen by ray i are modeled by integration along the line-of-sight of the attenuation coefficient, refractive decrement and scatter coefficient. This follows section 4.5.1 for monochromatic imaging. For this, we simply introduce the energy dependence for the radiographic images as well as the object parameters.

The three images are then given by

$$T_i(E) = \exp\left(-\sum_j M_{ij} \cdot \mu_j(E)\right) \quad , \tag{8.5}$$

$$D_i(E) = \exp\left(-\sum_j M_{ij} \cdot \sigma_j(E)\right) \quad . \tag{8.6}$$

$$\Delta\phi_i(E) = \sum_j M_{ij}^{\delta} \cdot \delta_j(E) \quad , \tag{8.7}$$

where the notation of section 4.5.1 is used. The specific ray and the voxel coefficient are denoted by i and j, respectively. The conventional and differential matrix elements are denoted by M_{ij} and M_{ij}^{δ}. Given the projected values $T_i(E)$, $D_i(E)$ and $\Delta\phi_i(E)$ we expect the observed photon counts $n_{i,s}$ at stepping position s to be

$$n_{i,s} = \int n_{i,s}(E)\,\mathrm{d}E = \int \mathrm{d}E \;\; N_i(E) \cdot (1 + V_i(E) \cdot \cos\phi_{i,s}(E)) \quad , \tag{8.8}$$

with the expected mean photon count

$$N_i(E) = N_i^0(E) \cdot T_i(E) \quad , \tag{8.9}$$

the expected visibility

$$V_i(E) = V_i^0(E) \cdot D_i(E) \quad , \tag{8.10}$$

and the expected phase

$$\phi_{i,s}(E) = \phi_i^0(E) + \phi_s + \Delta\phi_i(E) \quad . \tag{8.11}$$

The relative phase $\phi_s := 2\pi\frac{s}{p_2}$ depends on the stepping distance s of G_2 and the grating period p_2. $N_i^0(E)$, $V_i^0(E)$, and $\phi_i^0(E)$ denote energy-dependent free-field reference measurements for pixel i. However, $N_i^0(E)$, $V_i^0(E)$, and $\phi_i^0(E)$ can not directly be measured in a setup with an energy-integrating detector. Prior knowledge on the X-ray tube and the acquisition setup provides the per-energy amount of photons $N_i^0(E)$. Phase shift per energy $\phi_i^0(E)$ and visibility per energy $V_i^0(E)$ can be reasonably well estimated from free-field simulation using prior knowledge of the setup parameters, i.e., spectrum, source focal size, detector response and grating materials, geometry and positions. Figure 8.8 shows example simulations for the setup used in this thesis. Here, the spectrum is plotted in blue, the energy-dependent visibility is plotted in red.

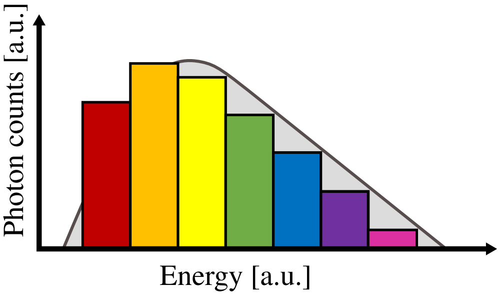

Figure 8.9: The continuous spectrum is subdivided into several energy bins.

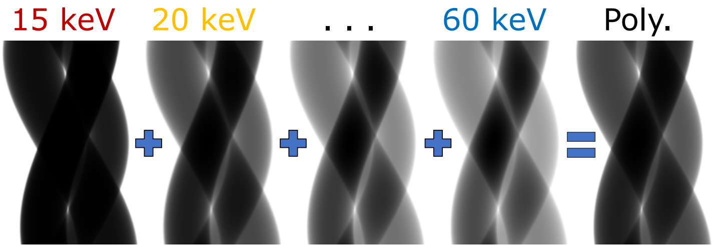

Figure 8.10: Schematic example of polychromatic model: For each energy bin phase-stepping data (her exemplary shown for phase step 0) are estimated. The superposition of these images result in the expected phase-stepping data of a polychromatic setup.

The forward model stated above is general and requires multi-spectral images in reconstruction domain[1]. Each voxel element j is required to contain the attenuation, refractive decrement and scattering coefficient at any energy E. The information per energy is inferred from the model in Eqn. (8.2) to Eqn. (8.4). The integration over the whole spectrum is done by subdivision into an arbitrary number of energy bins and subsequent summation.

$$n_{i,s} = \sum_k N_i(E_k) \cdot (1 + V_i(E_k) \cdot \cos \phi_{i,s}(E_k)) \quad . \tag{8.12}$$

A schematic example of this polychromatic estimation of phase-stepping data is given in Fig. 8.10.

8.2.3 Connection between Polychromatic and Monochromatic Reference

Since a continuous forward projection is not possible, the spectrum is subdivided into several energy bins. The binned spectrum - as illustrated in Fig. 8.9 - is then given by

$$N(E_k) = \int_{E_{k-1}}^{E_k} N(E)\,\mathrm{d}E \quad , \tag{8.13}$$

where $N(E)$ and $N(E_k)$ denote the continuous and binned spectrum, respectively. Estimation of the binned visibility is done with an equivalent integration. With the wave propagation simulation CXI [92] it is possible to estimate the spectral data of the setup's photon flux, phase and visibility. Tomographic Talbot-Lau data can then be simulated either using CXI or applying the polychromatic forward model given by Eqn. 8.12.

For some application, such as filtered back projection techniques to estimate an initial solution for the iterative reconstruction, a prior phase-retrieval of the Talbot-Lau data is required. For this the setup's total photon flux and visibility have to be known. The total number of photons is simply given by integration over the spectrum by

$$\overline{N} = \int N(E)\,\mathrm{d}E \quad , \tag{8.14}$$

---

[1] We want to mention explicitly that no multi-spectral radiographic images are required. By multi-spectral images in reconstruction domain we mean that attenuation coefficient, refractive decrement and scattering index are required to be known at all energies of the spectrum.

To calculate the total reference visibility of the system one cannot simply integrate the spectral visibility, but has to weight it with the photon flux at the energy of interest:

$$\overline{V} = \frac{\int N(E) \cdot V(E)\,\mathrm{d}E}{\int N(E)\,\mathrm{d}E} \quad . \tag{8.15}$$

This formula is only valid in an energy region where no zero-crossing of the energy-visibility curve occurs. At this point the differential phase experiences a phase-shift of π, which requires special consideration for a correct description. However, for the sake of simplicity this effect was not included in the above given formula, since this effect is almost negligible for the used setups.

Reconstruction Algorithm

For reconstruction we adapt the iterative maximum-likelihood algorithm for monochromatic Talbot-Lau tomography introduced in chapter 4. In doing so we exchange the monochromatic forward model with the proposed polychromatic model. Minimization of the cost function performed by coordinate gradient descent to iteratively update attenuation, phase and scatter image [19]. In each update step a line search is done by backtracking, see [18].

Derivation of Gradient

The gradient formulas of the monochromatic imaging model given in Sec. 4.5.3 are not valid for the polychromatic model defined by Eqn. 8.12. The following section derives the gradient for the proposed imaging model with respect to the Likelihood function given by Eqn. 4.18.

To achieve this, we remember that the general gradient of this Likelihood is already given by Eqn. 4.38. As the first step we calculate the derivatives of the imaging model with respect to μ_j, δ_j and σ_j:

$$\begin{aligned}
\frac{\partial}{\partial \mu_j} n_{i,s} &= \frac{\partial}{\partial \mu_j} \int \mathrm{d}E \;\; N_i(E) \cdot (1 + V_i(E) \cdot \cos(\phi_{i,s}(E))) \\
&= \int \mathrm{d}E \;\; \frac{\partial}{\partial \mu_j} N_i(E) \cdot (1 + V_i(E) \cdot \cos(\phi_{i,s}(E))) \\
&= \int \mathrm{d}E \;\; (-M_{ij} \cdot N_i(E)) \cdot (1 + V_i(E) \cdot \cos(\phi_{i,s}(E))) \\
&= -M_{ij} \cdot n_{i,s}
\end{aligned} \tag{8.16}$$

$$\begin{aligned}
\frac{\partial}{\partial \delta_j} n_{i,s} &= \frac{\partial}{\partial \delta_j} \int \mathrm{d}E \;\; N_i(E) \cdot (1 + V_i(E) \cdot \cos(\phi_{i,s}(E))) \\
&= \int \mathrm{d}E \;\; N_i(E) \cdot V_i(E) \cdot \frac{\partial}{\partial \delta_j} \cos(\phi_{i,s}(E)) \\
&= \int \mathrm{d}E \;\; N_i(E) \cdot V_i(E) \cdot (-1) \sin(\phi_{i,s}(E)) \cdot \frac{\partial}{\partial \delta_j} \phi_i(E) \\
&= -\int \mathrm{d}E \;\; N_i(E) \cdot V_i(E) \cdot \sin(\phi_{i,s}(E)) \cdot M_{ij}^{\delta}
\end{aligned} \tag{8.17}$$

$$\begin{aligned}\frac{\partial}{\partial \sigma_j} n_{i,s} &= \frac{\partial}{\partial \sigma_j} \int \mathrm{d}E \;\; N_i(E)\cdot(1+V_i(E)\cdot\cos(\phi_{i,s}(E))) \\ &= \int \mathrm{d}E \;\; N_i(E)\cdot \frac{\partial}{\partial \sigma_j} V_i(E)\cdot\cos(\phi_{i,s}(E)) \\ &= -\int \mathrm{d}E \;\; N_i(E)\cdot V_i(E)\cdot\cos(\phi_{i,s}(E)) M_{ij}\end{aligned} \tag{8.18}$$

Inserting into Eqn. 4.38 leads to the gradient of the likelihood l for the polychromatic model in respect to the three image coefficients:

$$\frac{\partial}{\partial \mu_j} l = \sum_{i,s} (N_{i,s} - n_{i,s})\cdot M_{ij} \;\; . \tag{8.19}$$

$$\frac{\partial}{\partial \delta_j} l = \sum_{i,s} \left(\frac{N_{i,s}}{n_{i,s}} - 1\right) \int \mathrm{d}E \;\; N_i(E) V_i(E) \sin\phi_{i,s}(E)\cdot M^{\delta}_{ij} \;\; . \tag{8.20}$$

$$\frac{\partial}{\partial \sigma_j} l = \sum_{i,s} \left(\frac{N_{i,s}}{n_{i,s}} - 1\right) \int \mathrm{d}E \;\; N_i(E) V_i(E) \cos\phi_{i,s}(E)\cdot M_{ij} \;\; . \tag{8.21}$$

Implementation

Implementation was done within the reconstruction framework developed in this thesis, see chapter 5. The highest computational effort is located in the polychromatic forward-projection. This requires projection of N volumes at different energies E, where N is the number of used energy bins. Since each energy bin is mutually independent, multi-core computing was applied to significantly reduce computation time.

8.3 Second Derivative

The reconstruction algorithm proposed by Ritter *et al.* is the simple gradient descent, see chapter 4. Brendel *et al.* reported faster convergence if attenuation, phase and scatter images are reconstructed independently using coordinate descent. Additionally, slow convergence for the phase image was reported [19, 94]. More detailed experiments regarding this convergence behavior will be given in chapter 9 .

In this section we propose a novel reconstruction algorithm to optimize the cost function given by Eqn. 4.37.

The algorithm proposed here is inspired by work of Boyd and Vandenberghe [18]. In their book they give a comprehensive overview over convex optimization techniques. Gradient descent is a special case of the so-called steepest descent algorithm. For this, we review the first-order Taylor approximation $\hat{f}(x)$ of a function $f(x)$ around x

$$f(x+v) \approx \hat{f}(x) = f(x) + \nabla f(x)^T v \;\; , \tag{8.22}$$

where $\nabla f(x)^T v$ is the directional derivative of $f(x)$ in direction v. We now seek to find the direction v to make the directional derivative as negative as possible. Since this is a linear function, we can make it as

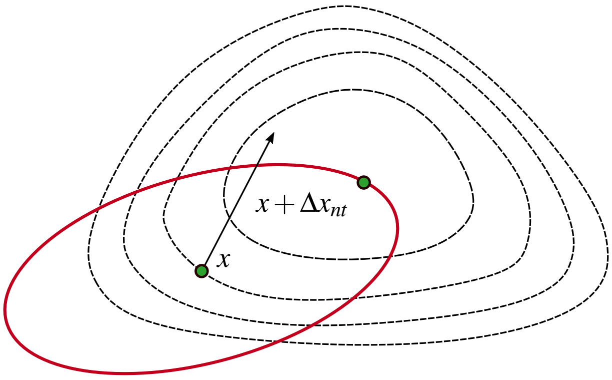

Figure 8.11: The dashed lines are level curves of a convex function. The ellipsoid (red) is defined by $\{x+v \mid v^T\nabla^2 f(x)v \leq 1\}$. The arrow shows the gradient descent direction $-\nabla f(x)$. The Newton step Δx_{nt} is the steepest descent direction in the norm $\|\cdot\|_{\nabla^2 f(x)}$. Redrawn after [18].

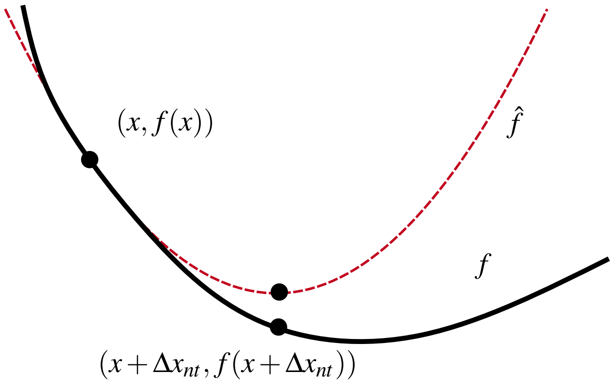

Figure 8.12: The function f (solid line) and its second-order approximation $\hat{f}$ at x (red). The Newton step Δx_{nt} is what must be added to x to give the minimizer of the parabola $\hat{f}$. Redrawn after [18].

negative as we like by simply taking v large. For this reason, v has to be constrained in length. Let $\|\cdot\|$ be any norm in $\mathbb{R}^N$. We then define a normalized steepest descent direction as

$$\Delta x_{nsd} = \arg\min\ \{\nabla f(x)^T v \mid \|v\| = 1\}\ . \tag{8.23}$$

Using this definition, it is simple to show that Δx_{nsd} coincides with the negative gradient $-\nabla f(x)$ if the euclidean norm is applied. However, more complicated norms are possible. If chosen appropriately, this can account for ill-conditioned optimization problems. In these problems, slow convergence speed is observed because the gradient is sharp in some directions but shallow in others.

A particularly interesting choice is the quadratic norm defined by the Hessian $\nabla^2 f(x)$, i.e.,

$$\|u\|_{\nabla^2 f(x)} = (u^T\nabla^2 f(x)u)^{1/2}\ , \tag{8.24}$$

for $u \in \mathbb{R}^N$. This norm leads to the same direction as the so-called Newton step and is given by

$$\Delta x_{nt} = -\left(\nabla^2 f(x)^{-1}\right)\nabla f(x)\ . \tag{8.25}$$

The newton step emerges from the second-order Taylor approximation, see Fig. 8.12. It provides the exact minimizer if the function is quadratic and a fairly well estimation if the function f is nearly quadratic. Figure. 8.11 provides an intuitive example why the Newton step is a more efficient choice than the gradient direction. It is because by including the second-derivatives, or in other words the curvature, we rescale directions with too sharp or shallow slopes.

Theoretically, this method could be applied to minimize the likelihood for grating-based tomography. However, this optimization problem is high dimensional. For this reason the Hessian matrix is typically too large to compute and store, and too expensive to invert.

Becker *et al.* [8] proposed in a completely different field of optimization theory, namely neural networks in machine learning, an algorithm to improve convergence of back-propagation learning with second order methods. Since back-propagation is a sort of gradient descent algorithm, it can be adapted to our problem. Instead of calculating the full Hessian matrix, they ignore all non-dialog entries. Under this approximation, the Hessian has only diagonal elements

$$\frac{\partial^2}{\partial {x_j}^2} f = \frac{\partial^2}{\partial x_j \partial x_j} f \ , \tag{8.26}$$

and its inversion becomes trivial. They then define the "pseudo-Newton step" for coordinate x_j as follows:

$$\Delta x_j = \frac{\frac{\partial}{\partial x_j} f}{\frac{\partial^2}{\partial {x_j}^2} f + \varepsilon} \ , \tag{8.27}$$

where $\frac{\partial}{\partial x_j} f$ denotes the first derivative and $\frac{\partial^2}{\partial {x_j}^2}$ the second derivatives. The heuristic ε is commonly used in numerical optimization methods to improve the conditioning of the Hessian in case the curvature approaches 0.

8.3.1 Adaption for Grating Based Iterative Reconstruction

Now we will replace the gradient step, as shown in section 4.3, with the "pseudo-Newton step" from Eqn. 8.27.

First we define the parameter set as usual to be

$$\theta_j = (\mu_j, \delta_j, \sigma_j) \ . \tag{8.28}$$

The function to be minimized is again the Poisson likelihood as defined in Eqn. 4.37. The first derivatives are given by Eqns. 4.45 to 4.47

We then calculate the second derivative with respect to image coordinate θ_j

$$\begin{aligned}
\frac{\partial^2}{\partial {\theta_j}^2} l &= \frac{\partial}{\partial \theta_j} \sum_{i,s} \left(1 - \frac{N_{i,s}}{n_{i,s}}\right) \cdot \frac{\partial}{\partial \theta_j} n_{i,s} \\
&= \sum_{i,s} \left(\frac{\partial}{\partial \theta_j} \left(1 - \frac{N_{i,s}}{n_{i,s}}\right)\right) \cdot \frac{\partial}{\partial \theta_j} n_{i,s} + \left(1 - \frac{N_{i,s}}{n_{i,s}}\right) \cdot \frac{\partial}{\partial \theta_j} \frac{\partial}{\partial \theta_j} n_{i,s} \\
&= \sum_{i,s} \frac{N_{i,s}}{n_{i,s}^2} \cdot \left(\frac{\partial}{\partial \theta_j} n_{i,s}\right)^2 + \left(1 - \frac{N_{i,s}}{n_{i,s}}\right) \cdot \frac{\partial^2}{\partial {\theta_j}^2} n_{i,s}
\end{aligned} \tag{8.29}$$

This summation is split into the squared first derivatives and the second derivatives of the Talbot-Lau imaging model of Eqn. 4.23. Again, the first derivatives have already been derived in Eqns. 4.45 to 4.47.

It remains to calculate the second derivative for the three images.

$$\begin{aligned}
\frac{\partial^2}{\partial {\mu_j}^2} n_{i,s} &= \frac{\partial}{\partial \mu_j} \frac{\partial}{\partial \mu_j} n_{i,s} \\
&= \frac{\partial}{\partial \mu_j} \left(-M_{ij} \cdot n_{i,s}\right) \\
&= (M_{ij})^2 \cdot n_{i,s}
\end{aligned} \tag{8.30}$$

$$\begin{aligned}
\frac{\partial^2}{\partial {\delta_j}^2} n_{i,s} &= \frac{\partial}{\partial \delta_j} - N_i \cdot V_i \cdot \sin(\phi_{i,s})\, \delta M_{ij} \\
&= -N_i \cdot V_i \cdot \cos(\phi_{i,s})\, (M_{ij}^{\delta})^2
\end{aligned} \tag{8.31}$$

$$
\begin{aligned}
\frac{\partial^2}{\partial {\sigma_j}^2} n_{i,s} &= \frac{\partial}{\partial \sigma_j} - N_i \cdot V_i \cdot \cos\left(\phi_{i,s}\right) \cdot M_{ij} \\
&= N_i \cdot V_i \cdot \cos\left(\phi_{i,s}\right) \cdot \left(M_{ij}\right)^2
\end{aligned}
\tag{8.32}
$$

After insertion of Eqns. 8.30 to 8.32 into Eqn. 8.29 we obtain the diagonal entries of the Hessian for each image as

$$
\begin{aligned}
\frac{\partial^2}{\partial {\mu_j}^2} l &= \sum_{i,s} \frac{N_{i,s}}{n_{i,s}^2} \cdot \left(-M_{ij} \cdot n_{i,s}\right)^2 + \left(1 - \frac{N_{i,s}}{n_{i,s}}\right) \cdot \left(M_{ij}\right)^2 \cdot n_{i,s} \\
&= \sum_{i,s} n_{i,s} \cdot M_{ij}^2 \quad ,
\end{aligned}
\tag{8.33}
$$

$$
\begin{aligned}
\frac{\partial^2}{\partial {\delta_j}^2} l =& \sum_{i,s} \frac{N_{i,s}}{n_{i,s}^2} \cdot \left(-N_i \cdot V_0^i \cdot \sin\left(\phi_{i,s}\right) M_{ij}^{\delta}\right)^2 + \left(1 - \frac{N_{i,s}}{n_{i,s}}\right) \cdot (-1) \cdot N_i \cdot V_i \cdot \cos\left(\phi_{i,s}\right) \left(M_{ij}^{\delta}\right)^2 \\
=& \sum_{i,s} \left[\frac{N_{i,s}}{n_{i,s}^2} \cdot \left(N_i \cdot V_i \cdot \sin\left(\phi_{,s}\right)\right)^2 + \left(\frac{N_{i,s}}{n_{i,s}} - 1\right) \cdot N_i \cdot V_i \cdot \cos\left(\phi_{i,s}\right)\right] \left(M_{ij}^{\delta}\right)^2 \quad ,
\end{aligned}
\tag{8.34}
$$

$$
\begin{aligned}
\frac{\partial^2}{\partial {\sigma_j}^2} l =& \sum_{i,s} \frac{N_{i,s}}{n_{i,s}^2} \cdot \left(-N_i \cdot V_0^i \cdot \cos\left(\phi_{i,s}\right) M_{ij}\right)^2 + \left(1 - \frac{N_{i,s}}{n_{i,s}}\right) \cdot \cdot N_i \cdot V_i \cdot \cos\left(\phi_{i,s}\right) \left(M_{ij}\right)^2 \\
=& \sum_{i,s} \left[\frac{N_{i,s}}{n_{i,s}^2} \cdot \left(N_i \cdot V_i \cdot \cos\left(\phi_{,s}\right)\right)^2 + \left(1 - \frac{N_{i,s}}{n_{i,s}}\right) \cdot N_i \cdot V_i \cdot \cos\left(\phi_{i,s}\right)\right] \left(M_{ij}\right)^2 \quad .
\end{aligned}
\tag{8.35}
$$

Chapter 9

Experiments and Results

The following chapter discusses the experiments and results. First, example reconstructions using the framework developed in this thesis - see chapter 5 - are shown. For one, tomographic data that were simulated with CXI - see Sec. 7.3 - are reconstructed. Second, reconstructions results of several real data measurements are presented.

It follows a detailed analysis of the discussed algorithms. For this, simulated data as described in Sec. 7.4 were used as ground truth. The section starts out with an analysis of the reconstruction algorithm employing the monochromatic imaging model. For this, two acquisitions schemes are analyzed with regard to the convergence properties of the three images attenuation, phase and scatter. First, Talbot-Lau data are reconstructed where full phase-stepping information is available at every projection angle. Second, reconstruction with the so-called interlaced acquisition scheme is investigated. This means that only one phase-step is performed per projection angle. Subsequently, we investigate the dependence of the reconstruction quality on various properties like noise, number of projections, number of phase steps or resolution. This section concludes with an study of the optimized reconstruction algorithm proposed in section 8.3.

The last part investigates the polychromatic forward model proposed in Sec. 8.2. The section commences with a simulation of synthetic Talbot-Lau data by applying the polychromatic model on a well-defined phantom. Phase-retrieval of the phase-stepping data and subsequent reconstruction with filtered back-projection reveals that the simulated data are indeed affected by polychromatic artifacts. It turns out that application of the proposed reconstruction algorithm - introduced in Sec. 8.2.3 - is able to remove these artifacts. These results will be published as a proceeding paper of the 2017th Fully3D conference [97]. After the algorithm is successfully applied on synthetic data, the last part of this chapter focuses on the reconstruction of real data.

For all reconstructions done with the iterative algorithm that will be presented in this chapter, the reconstruction volumes were initialized with zero. During this thesis different initialization methods - such as starting with the (smoothed) filtered back projection reconstructions - were investigated. However, initialization may result in a different outcome. For this reason only the zero volume initialization was used to exclude any possible bias.

9.1 Case Studies

The following section provides a selection of example reconstructions of tomographic Talbot-Lau data. An overview of the specimen used during this thesis has already been given in section 7.2. The reconstructed

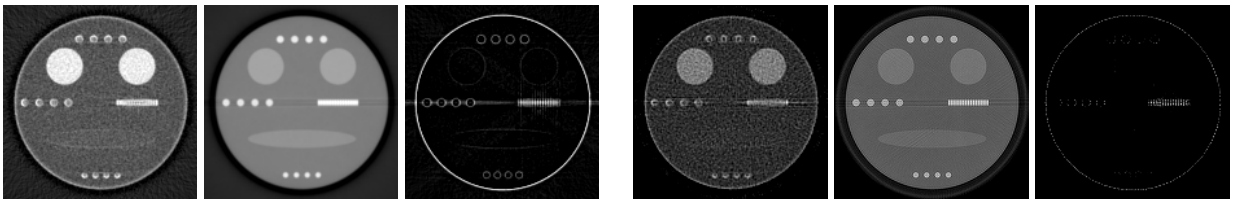

(a) μ (b) δ (c) σ (a) μ (b) δ (c) σ

Filtered back projection Iterative reconstruction

Figure 9.1: Reconstruction results for the Talbot-Lau data simulated with CXI. Talbot-Lau data are acquired with the interlaced acquisition scheme. There are no huge differences visible between filtered back projection and the iterative reconstruction. The phase image appears sharper when using the iterative reconstruction. Some streak artifacts are suppressed in the scatter image.

examples comprise both simulated and real data.

9.1.1 Simulations using CXI

Section 7.3 illustrated how Talbot-Lau data can be simulated using the CXI framework. In particular, a phantom made of several circular and elliptical shapes was discussed. In order to simulate a realistic imaging environment, Poisson distributed noise was added to the phase-stepping data of this phantom. For the experiment presented here the mean reference photon count per pixel was set to $N_0 = 5000$.

This section demonstrates that tomographic reconstruction with the interlaced acquisition scheme - proposed by Zanette *et al.* [127] - is possible using the framework developed in this thesis. Figure 9.1 compares results of filtered back projection and iterative reconstruction. The latter was stopped after 140 iterations. To apply filtered back projection, the missing phase-stepping data have been interpolated based on the algorithm proposed by [127]. The interlaced phase-stepping curve comprises 3 phase steps over 2π.

The image grid has a resolution of 150×150 with a spacing of $71\,\mu\text{m}$. 512 projections were measured in an angular range of 180°. The images do not significantly differ between filtered back projection and iterative reconstruction. However, the phase and scatter images appear to be sharper with iterative reconstruction. Also, some streak artifacts are suppressed in the scatter image.

9.1.2 Phantom made of Copper Wires, Steel, Foamed Plastic and Sand

This paragraph provides reconstruction results of the phantom shown in Fig. 7.5a. The detector comprises 268 pixels and 512 projections were measured over 360° with eight phase steps performed per projection angle. The reconstructed volume has a resolution of 200×200. The acceleration voltage was 100 kVp with an exposure of 1.133 mAs per phase-step. Even though the images were slightly truncated no major influence on the reconstruction result was observed. The coefficient were constrained to be always positive. Furthermore, all coefficients outside of the maximal possible reconstructed volume were set zero. Reconstruction was done with the coordinate descent. The gradient step was calculated using information of the second derivative.

Figure 9.2 contains results for filtered back projection and the iterative reconstruction. The attenuation and phase image do not differ much. However, the iterative reconstruction suppresses heavy streak artifacts in the scatter image.

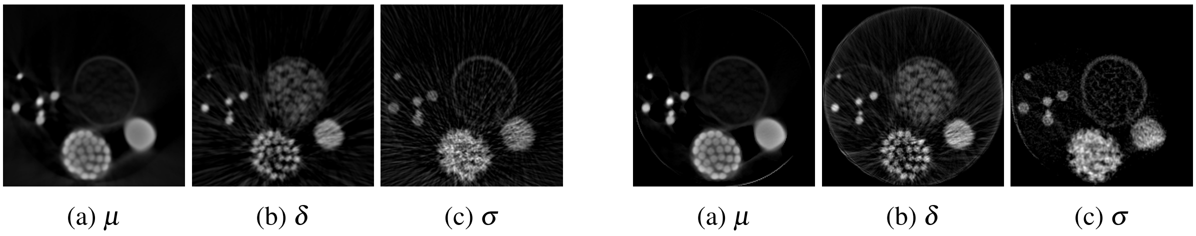
(a) μ (b) δ (c) σ (a) μ (b) δ (c) σ

Filtered back projection Iterative reconstruction

Figure 9.2: Reconstruction results for the phantom shown in Fig. 7.5a. The streak artifacts that appear in the scatter image of the filtered back projection are suppressed with the iterative reconstruction. The coefficients outside of maximal the possible volume are constrained to 0.

9.1.3 Phantom Made of Three Plastic Cylinders

This section is dedicated to data measured by Thomas Weber. These data were first published by Weber *et al.* in a work on the performance of phase-contrast tomography [116] and later reused by Andreas Wolf in his master thesis [123]. The employed setup was already introduced in Sec. 7.1.2. Eleven phase-steps per projection angle haven been performed. The sinogram comprises 1001 projections and 366 pixels. The acceleration voltage of the x-ray tube was set to 40 kVp. More information on the employed setup is found in [116]. The reconstructed volume has a resolution of 320×320. For optimization, the standard gradient descent was applied. The images have not been constrained in any way. Filtered back projection and iterative reconstruction results are shown in Fig. 9.3.

The images of the iterative reconstruction appear sharper than the filtered back projection. Streak artifacts seem to be removed in the scatter image. However, ring artifacts are more apparent in the iterative reconstruction. This is less severe for low reconstruction results, which is why ring artifacts are not seen in the results published by Weber *et al.* and Wolf [116, 123].

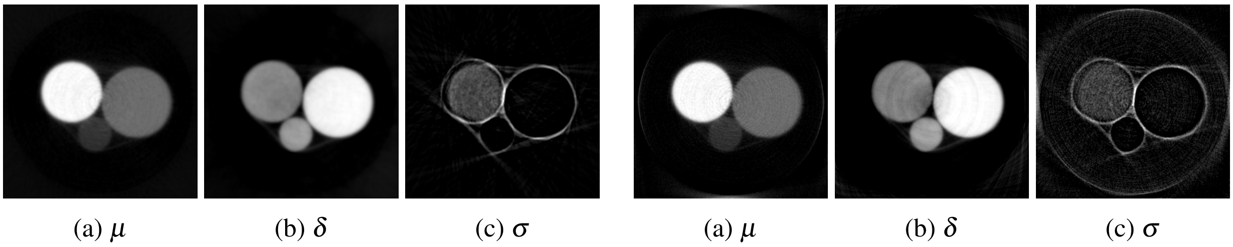
(a) μ (b) δ (c) σ (a) μ (b) δ (c) σ

Filtered back projection Iterative reconstruction

Figure 9.3: Reconstruction results of Talbot-Lau data aquired by Thomas Weber [116]. Iterative reconstruction produces sharper images. However, severe ring artifacts are exhibited by the iterative reconstruction.

9.1.4 Phantom made of Brass, Copper and Steel

This section aims to demonstrate that the iterative reconstruction is beneficial if strong noise in the differential and dark-field image is apparent. For this filtered back projection and iterative reconstruction results of phantom shown in Fig. 7.5h are given in Fig. 9.5. The data were acquired with an the acceleration voltage of 120 kVp and an exposure of 0.53 mAs per phase-step. Eight phase-steps per projection angle were measured.

Filtered back projection of the differential phase image does not provide any meaningful image, whereas the iterative reconstruction can at least partly reconstruct the correct image. Furthermore, the scatter image appears to be much smoother compared to filtered back projection.

To understand why, one recalls that the phantom comprises three cylinders made of three different metals: brass, copper and steel. These materials have large attenuation coefficients and thus harden the beam. Bearing in mind that the applied interferometer - see Sec. 7.1.1 - has very low reference visibilities for higher energies, it becomes clear why the measured visibility in the regions affected by severe beam hardening is almost saturated. This implies that while attenuation can still be reconstructed well, data retrieval for the differential phase and dark-field becomes infeasible. However, strong beam-hardening artifacts still occur in the attenuation image. For a better grasp of situation, the reconstructed sinograms are shown in Fig. 9.4. The strong noise in the phase image has fatal consequences for the tomographic reconstruction of the refractive decrement where the Hilbert-filter is applied to the differential image. This effect is not that severe for the dark-field, where the Ram-Lak kernel is applied. The scatter image appears only noisy.

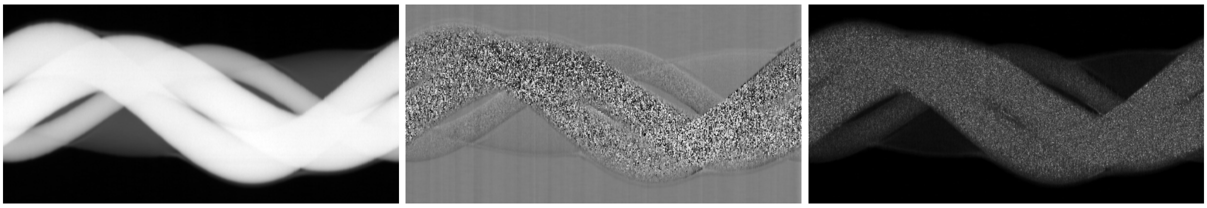

(a) μ (b) δ (c) σ

Figure 9.4: Talbot-Lau sinogram data of the phantom shown in Fig. 7.5h. The visibility has been saturated. No meaningful data for the differential phase and the dark-field images can be retrieved. This has fatal consequences for the tomographic reconstruction of the phase images, as shown in Fig. 9.5.

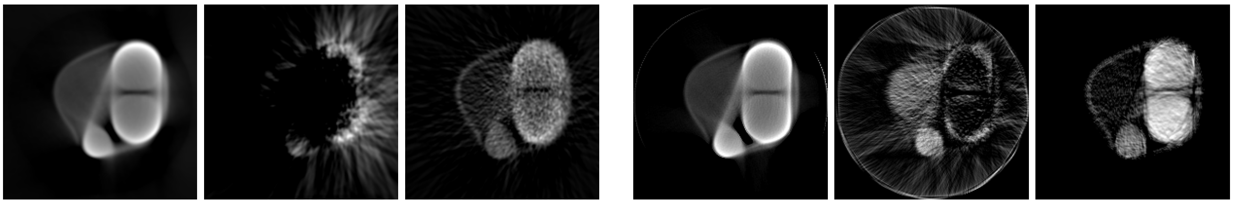

(a) μ (b) δ (c) σ (a) μ (b) δ (c) σ

Filtered back projection. Iterative reconstruction

Figure 9.5: The attenuation image is well reconstructed by filtered back projection and iterative reconstruction. However, strong beam hardening effects occur. The tomographic image of the phase can not be reconstructed via filtered back projection. Iterative reconstruction can reconstruct it better, but strong are artifacts are still visible. Filtered back projection of the dark-field is noisy. The iterative reconstruction results in a sharper and much smoother image.

9.1.5 Bone with Fissure

Jonas Pfeiffer investigates in his master thesis the potential of the differential phase-contrast and the dark-field image to detect the filamentous structures of fissures. A tomographic scan of a pig femur inflicted with a fissure was performed to gain further information on the geometrical structure of fissures. An image of the sample is shown in Fig. 7.5i. The acceleration voltage was 65 kVp with an exposure of 4.5 mAs per phase-step. Eight phase-steps per projection angle have been performed.

The fissure was artificially created by driving a small nail into the bone. However, the whole bone is too large to be measured within the field-of-view of our tomographic setup. The bone was therefore sawed around the fissure to fit in the field-of-view.

Reconstruction results are shown in Fig. 9.6. Filtered back projection provides satisfactory images for attenuation and refractive decrement, while the scatter image exhibits streak artifacts inside and outside of the object. Application of the iterative reconstruction algorithm is able to suppress those. However, other artifacts, such as ring artifacts and unphysical values for the refractive decrement and scatter at the boundaries of the field-of-view, appears. We believe that these artifacts can be reduced by small adjustment of the reconstruction algorithm which is left open for future work. Additionally, it is remarkable that the iterative reconstruction provides a sharper image of the phase image than filtered back projection.

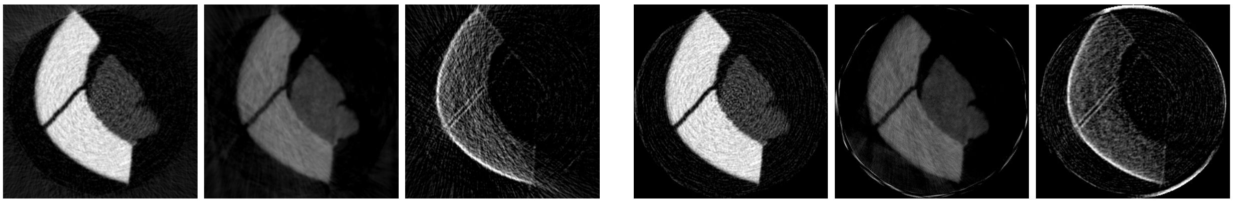

(a) μ (b) δ (c) σ (a) μ (b) δ (c) σ

Filtered back projection Iterative reconstruction

Figure 9.6: The attenuation images looks similar for filtered back projection and iterative reconstruction. The phase-images appears to be much sharper in the iterative reconstruction. The scatter image exhibits streak artifacts that are suppressed with the iterative reconstruction.

9.1.6 Tomographic Scan of an Ex-Vivo Mouse

Section. 7.4 illustrates how a synthetic phantom can be defined from prior reconstructed image data, for instance obtained with filtered back projection. In this case an ex-vivo tomographic scan performed by Weber *et al.* was used [114]. This phase-stepping data can also be used as input for the iterative reconstruction.

The setup parameter are listed in Sec. 7.1.2. The acceleration voltage of the X-ray tube was 40 kV, leading to a mean energy of $E = 29.6\,\mathrm{keV}$ taking the energy-dependent quantum efficiency of the detector into account. The mean visibility was calculated to be $V_0 = 42.2\%$. One row of the detector comprises 751 pixels and 601 projections with eight phase-steps per angle were measured in an angular range of 360°. The reconstructed volume has a resolution of 512×512 with a grid spacing of 86 µm. More information on the employed setup is found in [114].

The reconstruction was done with the standard coordinate descent method and was stopped after 500 iterations. The resulting images are shown in Fig. 9.7. For reconstruction, the coefficients were constrained to have non-negative values and are always zero outside the possible reconstruction volume. The phase image appears sharper for the iterative reconstruction, but besides of this no major differences are visible compared to filtered back projection. A concise analysis of the convergence properties is given in Fig. 9.8. Here the filtered back projection reconstructions were used as ground truth to calculate the structural similarity as introduced in Sec. 6.3. The attenuation image convergences the fastest, while phase and scatter image require significantly more iterations until sufficient convergence.

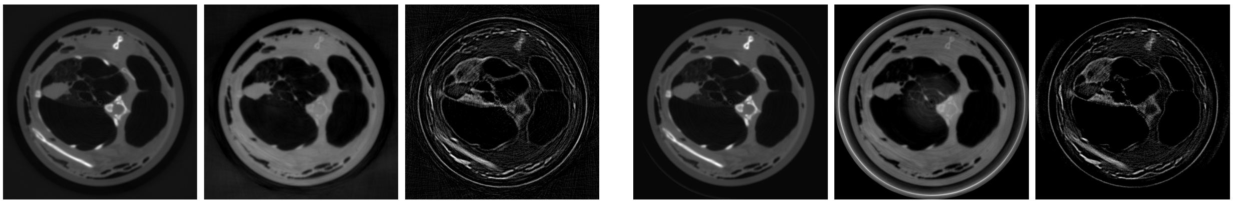

(a) μ (b) δ (c) σ (a) μ (b) δ (c) σ

Filtered back projection Iterative reconstruction

Figure 9.7: Reconstruction results of the ex-vivo mouse sample. Filtered back projection and iterative reconstruction do not differ much. The iterative reconstruction algorithms seems to provide a sharper image of the refractive decrement and scatter.

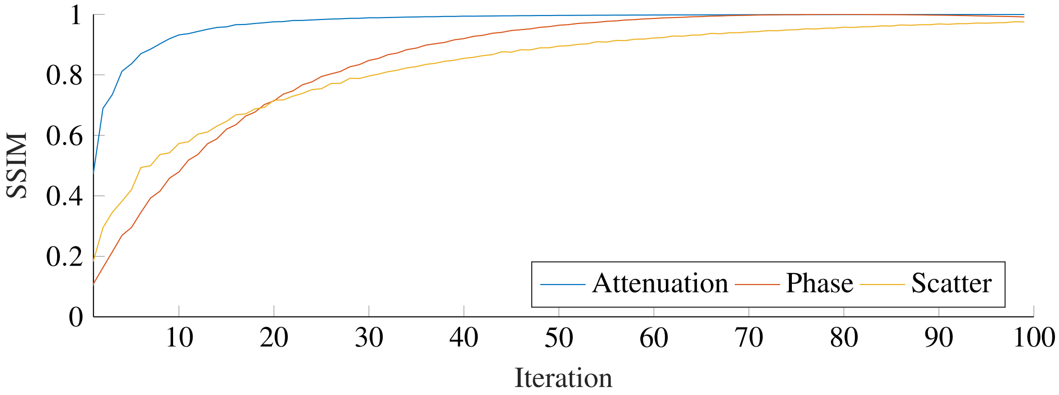

Figure 9.8: The plot shows the structural similarity of the mouse sample for the three images in respect to the iteration number. The filtered back projection reconstructions were used as ground truth data for calculation of the SSIM. For a better visualization only the first 100 iterations are plotted. The attenuation image convergences the fastest.

9.2 Reconstruction Properties

This section provides an analysis of the reconstruction properties with the monochromatic forward model. Among those are - for instance - the influence of noise, number of projections, reference visibility or object size. For this, the Talbot-Lau data that were generated by forward projection of well defined phantoms as described in Sec. 7.4 are used. The reconstruction results can then be compared with the ground truth. Application of error metrics - such as the *PSNR* or *RMSE* introduced in Sec. 6.3 - allow to quantify the reconstruction quality. The first part concentrates on tomographic Talbot-Lau data where the full phase-stepping data are acquired. The second part focuses on data where only one phase step per projection is measured.

For all simulation experiments reconstruction was done using the coordinate descent. The update step is calculated exploiting information on the second derivative as proposed in Sec. 8.3. The initial solution has been the zero volume for all three images. The coefficients were constrained to be always positive. Furthermore, all coefficients outside of the physically possible reconstruction area are set to be always zero. The algorithm was stopped after 1000 iterations.

For the simulation experiments, Talbot-Lau data are generated by monochromatic forward projection according to Sec. 7.4. The used phantom is the circle phantom introduced in Fig. 7.8 where attenuation and refractive decrement are assigned from literature values at an photon energy of 80 keV. The resolution of the detector and reconstructed volume were 512 pixels and 256 × 256, respectively. The pixel pitch was 390 µm and the grid spacing 780 µm. The acquisition geometry was 360 projections over 360°. Four phase-steps per projection angle have been performed with a reference visibility of 50 %. For most experiments the mean reference count per pixel was set to $N_0 = 5 \cdot 10^5$ if not declared otherwise. Depending on the actual experiment performed, some of these parameters may vary.

9.2.1 Full Phase Stepping Reconstruction

Number of Reference Photon Counts

This section investigates the noise properties of the iterative reconstruction. For our experiment, the mean reference counts N_0 seen per pixel was increased exponentially. The *PSNR* - introduced in Sec. 6.3 - for the reconstruction results are plotted in Fig. 9.9. The results coincide with the expectation since the *PSNR* increases linearly with the photon counts.

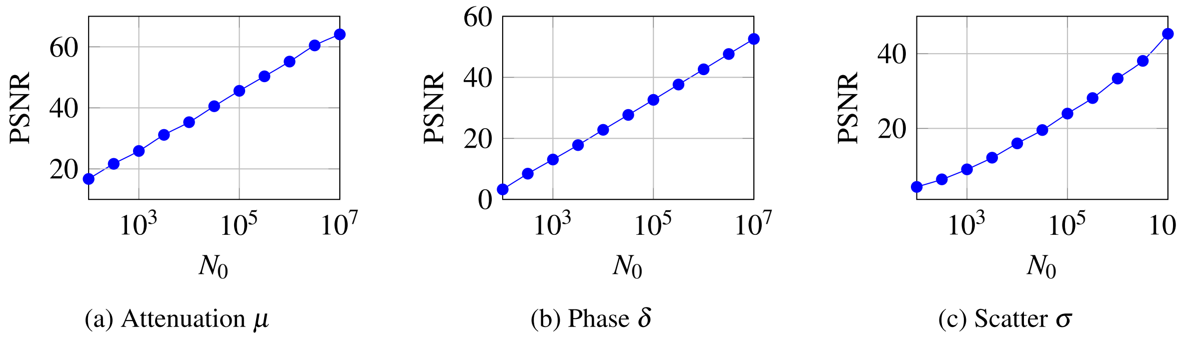

(a) Attenuation μ (b) Phase δ (c) Scatter σ

Figure 9.9: In this experiment the influence of the mean reference photon count N_0 on the reconstruction result is studied. The cylinder phantom was used for simulation of Talbot-Lau data where the mean reference photon count N_0 was increased exponentially. The plots shows the *PSNR* which is increasing linearly.

Object Size

The object size has an essential influence in computed tomographic. Generally, the larger the object, the higher are the line-integral values. In medical imaging where large objects are of interest bad photon statistics are apparent due to the exponential character of the Beer-Lambert law. This becomes a major issue in Talbot-Lau imaging. Heavy noise in the phase-stepping data does not translate linearly in the measured phase-shift [88]. However, the situation is different for small objects. In this case almost no attenuation contrast is observed, but the differential phase-shift provides sufficient signal.

A comprehensive study on signal and noise propagation for X-ray differential phase-contrast tomography was published by Raupach *et al.* [88, 87]. However, his findings assume filtered back projection and do not necessarily translate directly to iterative reconstruction techniques, especially when regularizers are used.

This experiments studies the influence of the object size on the reconstruction parameters. Phantom and setup parameters are listed in the beginning of the section above. The object size was increased exponentially from 1 cm to 68 cm. The pixel pitch and the grid spacing were coupled to the current object size. Moreover, for different object sizes, the noise level differs drastically. For example, the smallest

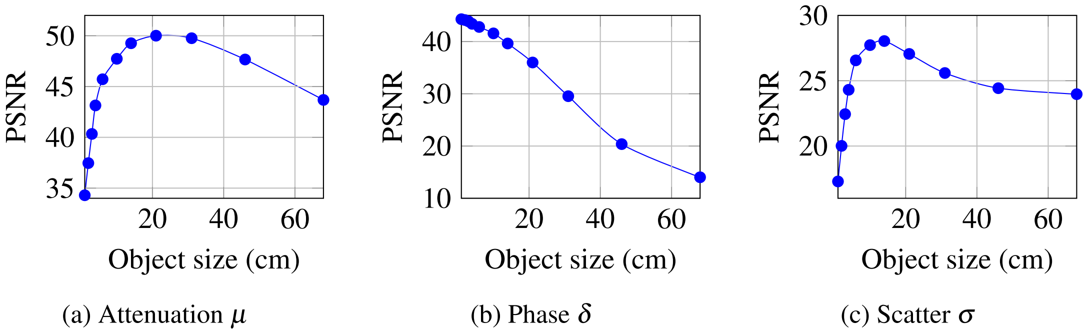

(a) Attenuation μ (b) Phase δ (c) Scatter σ

Figure 9.10: In this experiment we have investigated the influence of the object size on the reconstruction result. Tomographic reconstruction of the phase image is the best for small objects. The attenuation image becomes better for increasing object size. However, due to the large dimensions, attenuation becomes too large and the noise degree permits good reconstruction. Similar behavior is observed for the scatter image.

object (1 cm) experiences much less absorption than the largest (68 cm). For this reason, we admit that on might rightfully doubt if the presented results can be considered meaningful or not. However, due to time constraints we could not repeat the experiments with more meaningful parameters.

The *PSNR* for the three images in dependence of the object size is shown in Fig. 9.10. For small object sizes the attenuation image can not be reconstructed well because the attenuation contrast is low. The *PSNR* increases rapidly with an increased objects size due to concomitantly increased attenuation contrast. This goes on until a critical point is reached at which the *PSNR* is decreased because absorption is too high and the noise prevails. Similar behavior is observed for the scatter image. The situation different for the image of the refractive decrement. The *PSNR* is maximal for small objects and decays with an increasing object size.

Influence of Reference Visibility

This experiment examines the influence of the reference visibility on the reconstruction results. Phantom and setup parameters are the same as in Sec. 9.2.1. The reference visibility was varied from 5 % up to 60 %.

The *PSNR* for the images in dependence of the reference visibility is shown in Fig. 9.11. The attenuation image is almost independent of the visibility. This in accordance to our expectation since the phase-stepping curve's mean does not change with an decreased visibility. On the other hand, the noise properties of differential phase and the dark-field do indeed depend on the reference visibility. This translates also to the iterative reconstruction results. The *PSNR* increases noticeably with increasing visibility.

Number of Phase Steps

This section studies the influence of the number of phase-steps on the reconstruction result. Phantom and setup parameters are the same as in Sec. 9.2.1. In this experiment the number of phase-steps performed per projection angle is varied from two to ten. In order to keep the dose level the same, the total number of reference photon counts was set to be constant. The *PSNR* in dependence of the number of phase-steps is shown in Fig. 9.12.

If three or more phase-steps are performed, the reconstruction result does not depend on the number of phase-steps. For two phase-steps the image of the refractive index can not be reconstructed correctly.

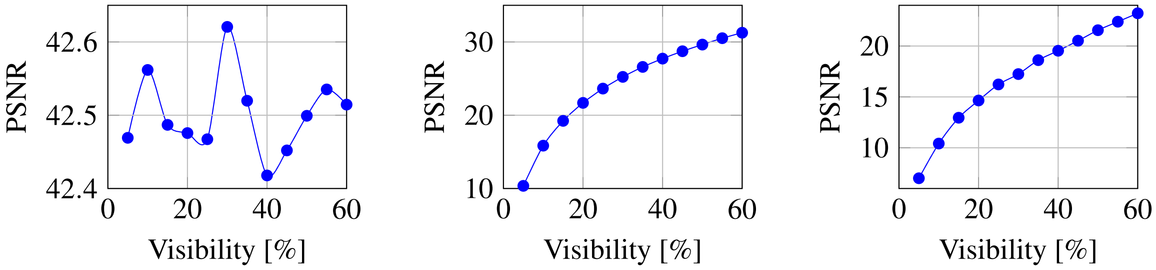

(a) Attenuation μ (b) Phase δ (c) Scatter σ

Figure 9.11: In this experiment the influence of the reference visibility on the reconstruction result was investigated. Here we show the PSNR over visibility. As expected, the attenuation image is almost independent on the reference visibility, while phase and scatter image increase with the visibility.

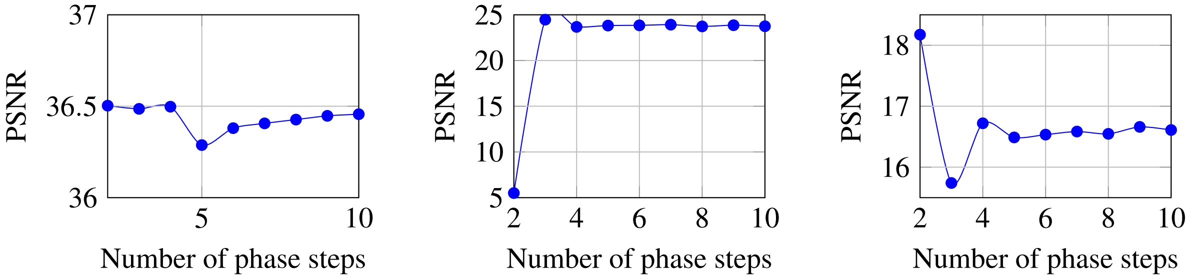

(a) Attenuation μ (b) Phase δ (c) Scatter σ

Figure 9.12: Reconstruction properties if the number of phase-steps per projection angle is changed. Data are acquired with the full acquisition scheme. The phase-image fails to be recovered with only 2 phase-steps per projection angle. This is in accordance to conventional phase-contrast imaging where at least 3 phase-steps need to be performed. The attenuation is easier extracted, thus two phase-steps suffice for a proper reconstruction. Generally, the result does not depend heavily on the number of phase-steps.

However, attenuation and scatter image do not suffer[1].

9.2.2 Interlaced Reconstruction

A major advantage of iterative Talbot-Lau tomography is that no phase-retrieval is necessary. This allows for acquisition schemes where only phase-step per projection angle is measured [127]. This is a necessary step to embed a Talbot-Lau interferometer into a continuous rotating ct gantry. The following discusses reconstruction properties of the interlaced acquisition scheme.

Number of Projections

This experiment investigates how the reconstruction depends on the number of used projections. Talbot-Lau data were simulated using the monochromatic forward model at an energy of 80 keV. The detector size was set to be 20 cm and thus in the dimension of medical imaging applications. The detector consists of 512 pixels which results in a pixel spacing of 391 µm. The reconstructed image has a resolution of 400 × 400 with a grid spacing of 500 µm. The acquisition theme is interlaced where the phase-stepping curve consists of three phase-steps. The reference visibility was set to be 40 %. The Talbot distance is 67.5 cm. The gratings were $g_0 = 13.31\,\mu\text{m}$, $g_1 = 5.71\,\mu\text{m}$ and $g_2 = 10\,\mu\text{m}$.

---

[1] The PSNR of the visibility is the highest for only two phase-steps. It is possible that the location of the two phase-steps was in favor for the dark-field and mischievous for the phase. However, due to time constraints this could not be investigated further.

The tomographic angle has been 180° and the reconstructions performed for a different number of projection angles. The number of projections is increased from 100 up to 1200 projections with a step size of 100. In order to keep the dose level the same, the total number of detected reference photons was set to be constant

$$N_{Total} = N_{Steps} \cdot N_{Projections} = \text{const.} \quad , \tag{9.1}$$

where N_{Steps} is the number of phase-steps and $N_{Projections}$ the number of projections. The number of reference counts per detector pixel is then given by

$$N_{ref} = \frac{N_{Total}}{N_{Projections} \cdot N_{Steps}} \quad . \tag{9.2}$$

This experiment has been performed for two different photon statistics. For the low photon counts one has $N_{Total} = 20 \cdot 10^6$ and for better photon statistics $N_{Total} = 20 \cdot 10^8$. The results are shown in Fig. 9.15 and Fig. 9.16. In these plots, only the results with 400 projections and larger are included. Reconstructions with a lower number of projections have been possible, but exhibit strong streak artifacts. The proposed error metrics are not capable to provide a meaningful value. Indeed, the *PSNR* and *RMSE* suggest a better reconstruction for a lower number of projections even though the visual conception of the images clearly shows worse images.

For the low photon count experiment the *PSNR* increases noticeably with the number of projections until $N_{Proj} = 1000$. The behavior is different for the high photon experiment. Here the *PSNR* saturates after projection numbers of around 600.

In Fig. 9.13 and 9.14 we have shown the phase-reconstructed sinograms, filtered back projection and iterative reconstruction results for $N_{Proj} = 100$ and $N_{Proj} = 1200$, respectively. The under sampled scan has much better photon statistics, but shows very strong interpolation artifacts, especially in the phase and dark-field image. This propagates into the reconstruction with filtered back projection as heavy streak artifacts. The iterative reconstruction is able to suppress these under the cost of high, non uniform noise. On the contrary, the densely sampled tomographic scan shows much less interpolation artifacts, while the noise level is much higher. Filtered back projection is therefore noise as well. Especially in the the scatter image non zero coefficient are observed, where the ground truth has zero values. Reconstruction with the iterative method yield sharper images and some artifacts are reduced. However, the noise is increased. It is remarkable that the noise in the differential image shows different characteristics for filtered back projection and iterative reconstruction.

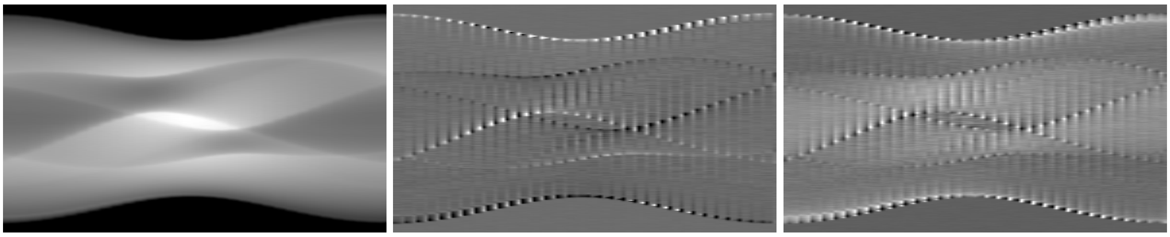

(a) Attenuation (b) Differential Phase (c) Dark-Field

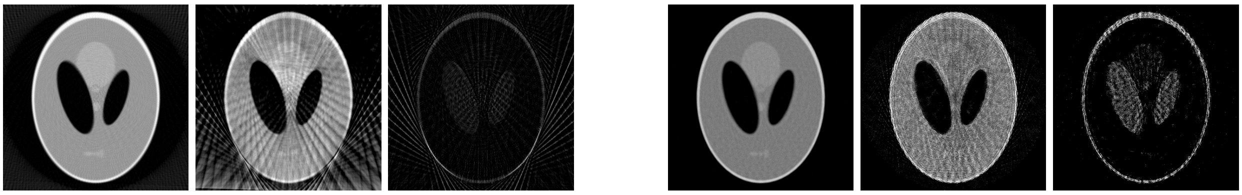

(d) μ (e) δ (f) σ (g) μ (h) δ (i) σ

Figure 9.13: The first row shows the interlaced Talbot-Lau sinograms for a tomographic set comprising 100 projections. Fig. (d-f) show filtered back projection results and Fig. (g-i) reconstructions with the iterative reconstruction. Strong interpolation artifacts between two projection angles are observed.

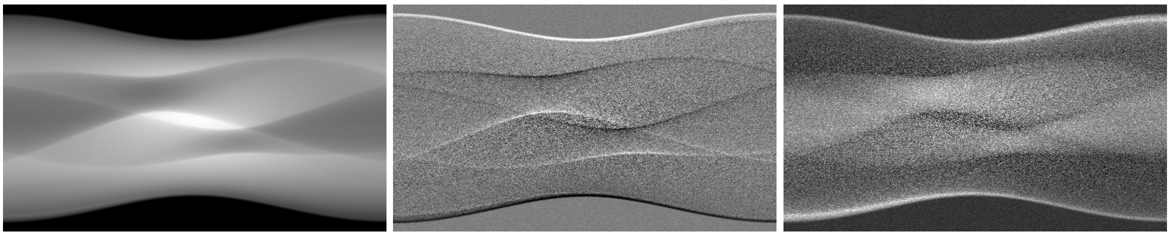

(a) Attenuation (b) Differential Phase (c) Dark-Field

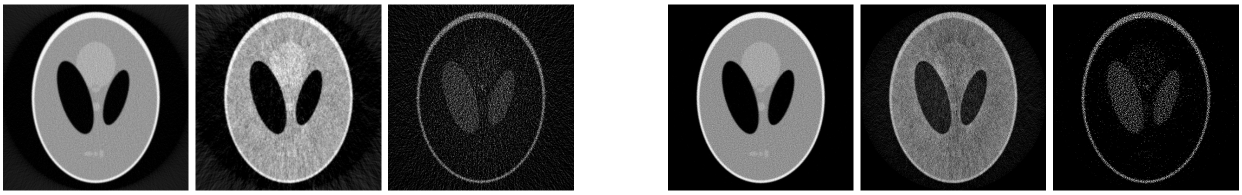

(d) μ (e) δ (f) σ (g) μ (h) δ (i) σ

Figure 9.14: The first row shows the interlaced Talbot-Lau sinograms for a tomographic set comprising 1200 projections. Fig. (d-f) show filtered back projection results and Fig. (g-i) reconstructions with the iterative reconstruction. While interpolation artifacts are highly reduced when compared to a scan with only 100 projections, the noise level is much higher.

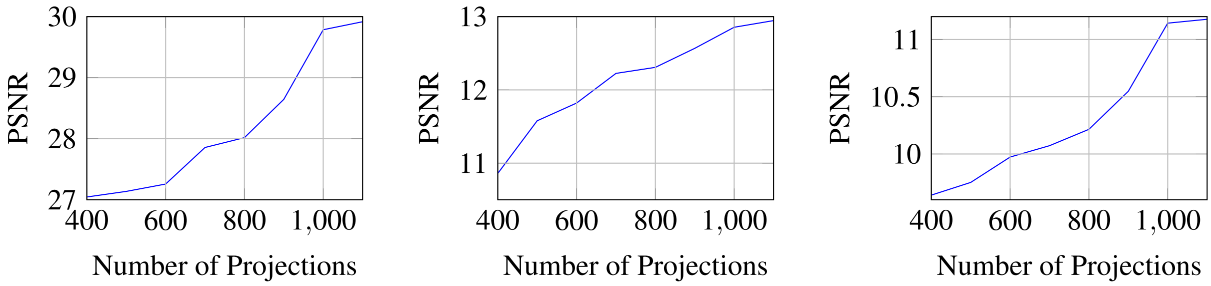

(a) Attenuation μ (b) Phase δ (c) Scatter σ

Figure 9.15: In this experiment we evaluate how the reconstruction results depends on the number of projections. As an error measured we have chosen the PSNR. The total photon counts measured in one pixel have been $N_{Total} = 20 \cdot 10^6$. We refer to this as the low photon count experiment

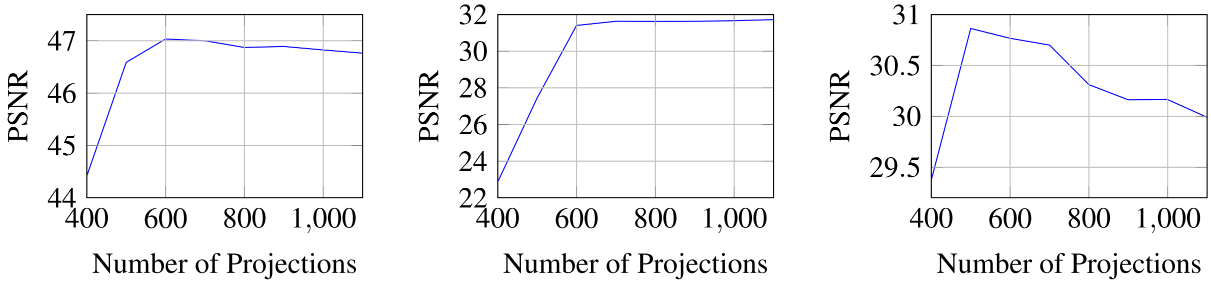

(a) Attenuation μ (b) Phase δ (c) Scatter σ

Figure 9.16: In this experiment we evaluate how the reconstruction results depends on the number of projections. As an error measure we have chosen the PSNR. The total photon counts measured in one pixel have been $N_{Total} = 20 \cdot 10^8$. We refer to this as the high photon count experiment.

9.3 Reconstruction with Second Derivative

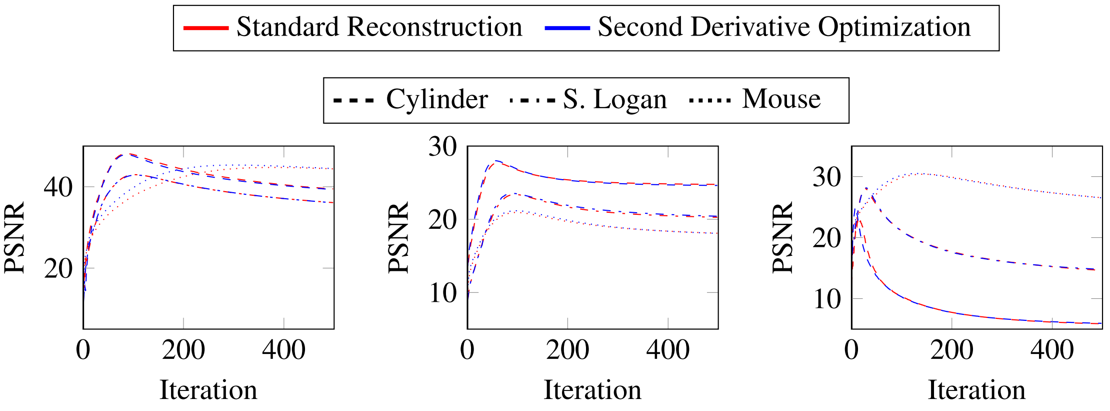

(a) Attenuation μ (b) Phase δ (c) Scatter σ

Figure 9.17: Second derivative vs. standard reconstruction for a detector size of 10cm.

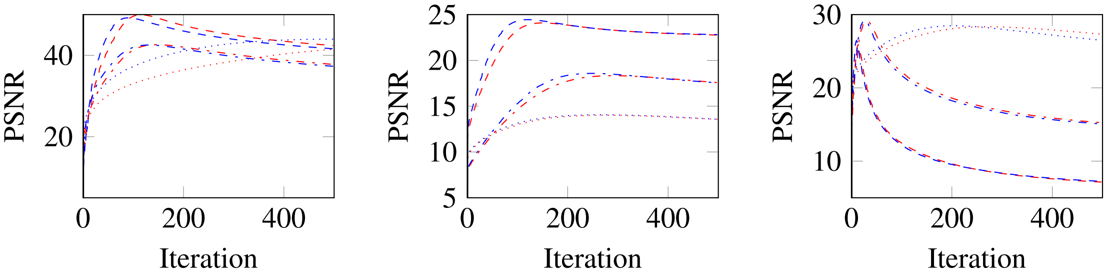

(a) Attenuation μ (b) Phase δ (c) Scatter σ

Figure 9.18: Second derivative vs. standard reconstruction for a detector size of 20cm.

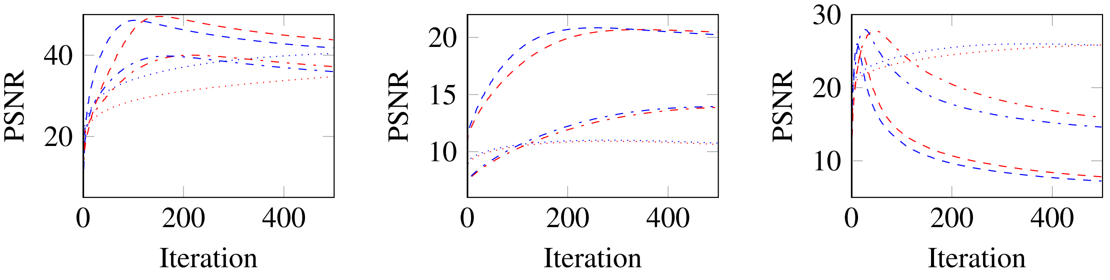

(a) Attenuation μ (b) Phase δ (c) Scatter σ

Figure 9.19: Second derivative vs. standard reconstruction for a detector size of 30cm.

Section 8.3 introduced an alternative algorithm to optimize the likelihood function. The main difference is that the gradient is scaled with the diagonal entries of the Hessian matrix, i.e. the second derivative. The following shortly compares convergence properties of the standard method (simple gradient) and the proposed method based on the second derivative.

For this experiment Talbot-Lau data were simulated with the monochromatic model at en energy of 70 keV for the three phantoms defined in Sec. 7.4. The detector comprises 300 pixels and a resolution of 200×200. The reference visibility was 35 %. The G_2 location and the grating periods have been the same as in 9.2.1. The reference photon counts per pixel has been set to 20.000. The tomographic setup was 360 projections over an angular range of 180°.

A full analysis of the proposed optimization algorithm has not been possible to due time constraints. It turned out that the performance depends on many parameters. In some cases the proposed method outperformed the standard reconstruction, while in other cases there has not been any visible difference. We have determined at least on important parameter, which is the size of the object. To prove this point, the above mentioned setup was simulated for three different object sizes. The object size is indirectly given via the detector size, since the size of the phantom - see Sec. 7.4 - scales with the detector size. The examined detector sizes have been 10 cm, 20 cm and 30 cm. The analysis investigates the *PSNR* in dependence of the iteration number for the three images attenuation, phase and scatter. Each figure depicts the *PSNR* for the standard reconstruction (blue) and proposed method (red). Results for the cylinder sample are plotted dashed, for the Shepp Logan dotted-dashed and for the mouse dotted. The obtained convergence curves for the three object sizes 10 cm, 20 cm and 30 cm are shown in Fig. 9.17, 9.18 and 9.19, respectively.

The reconstructions results are hard to interpret. For the mouse phantom the second derivative method is more effective than for the cylinder and the Shepp-Logan phantom. More over, there is a small tendency that the larger the object sizes the larger is the benefit of the second derivative. Additionally there are differences between the convergence behavior of the attenuation, phase and scatter images. The proposed method tends to yield a faster convergence, however it is questionable if this speed benefit justifies the higher computational effort of calculating the second derivative. A deeper analysis of the proposed algorithm has not been possible and leaves room for further investigation.

9.4 Polychromatic Reconstruction

This sections investigates properties of the polychromatic reconstruction proposed in Sec. 8.2.3. The first parts demonstrates that application of the forward model on synthetic data leads to polychromatic artifacts. Subsequent reconstruction with the proposed method is able to remove these artifacts. This follows an analysis of the reconstruction with real data.

9.4.1 Simulation Data

The evaluation in this section is based on synthetic data affected by beam-hardening. The data were obtained using the proposed forward model with a well-defined phantom. The objective is to see if an artifact free reconstruction within the maximum-likelihood framework is possible.

For this purpose a Talbot-Lau imaging system was simulated using a wave-propagation algorithm [80]. A 60 keV tungsten tube with a source size of 300 µm is used, and a perfect detector without any cross talk is assumed. All three gratings are made of gold. The source grating G_0 has a grating period of $p_0 = 10\,\mu\text{m}$ and a height of $h_0 = 200\,\mu\text{m}$. For the phase grating G_1, we have $p_1 = 5.716\,\mu\text{m}$, $h_1 = 6.3\,\mu\text{m}$. The analyzer grating G_2 has $p_2 = 10\,\mu\text{m}$, $h_2 = 200\,\mu\text{m}$ respectively. The distance from G_0 to G_1 is 0.8 m and G_1 to G_2 is 0.6 m.

The detector consists of 300 pixels with a size of 333 µm each. The reconstructed volume is 256^2 with a voxel size of 390 µm. The angular range is 360° with 480 projection images using a parallel beam setup where three phase steps per projection angle are performed. The mean reference photon count is constant over the detector with $N_{tot}^0 = 4.5 \times 10^6$ photons detected by each pixel per exposure. The spectrum was binned into 15 energy bins. Synthetic phase-stepping data of the three-cylinder phantom introduced in Sec. 7.4 are generated with the proposed forward model using the setup parameter from above.

Next, phase-retrieval is performed via least-square fitting on the phase-stepping data. Subsequently, the obtained attenuation, phase and dark-field sinograms are reconstructed using filtered back projection.

We use the Ram-Lak filter for attenuation and scatter, and the Hilbert filter for the differential phase image. This reconstruction is used as an initial solution for the proposed reconstruction algorithm. The algorithm is stopped after 200 iterations.

Figure 9.20 shows the difference between ground truth and the reconstruction results. From left to right, the images show distributions of absorption, phase, and scatter. In the top row, the ground truth is shown. The second and third row show the result of filtered backprojection and of the proposed algorithm. The two lines in Fig. 9.20 (a) indicate the location of the associated cross-section lineplots that are shown in Fig. 9.21. Here, ground truth is shown in black, the result by filtered backprojection is shown in blue, and the proposed method is shown by the red dashed line. In all three images reconstructed with filtered backprojection, typical cupping and streak artifacts are visible. These artifacts are more pronounced in attenuation and scatter than in the phase image. This is because the refractive decrement decays with only E^{-2}, while attenuation and scatter yield a stronger energy dependence.

The proposed algorithm is able to reconstruct all three images with almost all polychromatic artifacts removed. Reconstruction of attenuation and scatter are almost perfect. The phase-image exhibits slight cupping artifacts. We assume that these artifacts might also disappear if a higher number of iterations were chosen, but we will investigate this in greater detail in future work. Overall, we observed that attenuation and scatter images converge much faster than the phase-images. A similar behavior has already been mentioned by Brendel *et al.* with a maximum-likelihood reconstruction for monochromatic Talbot-Lau imaging [19]. We assume that this behavior originates from the differential nature of the phase image and the non-convexity of the cost function.

9.4.2 Real Data

The reconstruction results of the synthetic data shown in the previous chapter do not reflect the physical reality. This is because the simulated data live in a perfect, ideal world where data are generated in full accordance to the chosen physical model. One the one hand, it is necessary that the reconstruction framework is at least able to reconstruct simulated data. However, it is by far not sufficient to infer that the chosen model indeed reflects the physical reality.

In this thesis several specimen that exhibit polychromatic artifacts were built. Due to the small field-of-view of the tomographic scanner available at ECAP this is not an easy task. Most materials, such as plastic or soft-tissue, do not sufficiently harden the beam and thus no artifacts are observed. On the other hand, if highly absorbing materials, such as aluminum or copper are used, artifacts such as phase-wrapping emerge quickly. Eventually, a special focus was placed on polychromatic induced dark-field. Several phantoms have been found that indeed exhibit the desired image signals. Unfortunately, the proposed polychromatic reconstruction algorithm has not been able to suppress or remove the unwanted dark-field components. In fact, it turned out that the physical reality, i.e. the measured data, are in contradiction to what is expected from the polychromatic model.

This section discusses an example measurement affected by dark-field due to beam-hardening. It turns out that application of the polychromatic model can not describe the observed artifacts correctly. As a consequence, the iterative reconstruction cannot deal with polychromatic artifacts.

Equal results were obtained for all other specimen where polychromatic induced dark-field was observed. For this reason we restrain ourself to discussion of only one phantom since the same physical argumentations applies for the other specimen.

The least that could be done is to understand why the proposed model fails to reproduce the physical reality. For this, the examined specimen were synthetically rebuilt as well-defined phantoms that are subsequently polychromatic forward projected. The obtained Talbot-Lau data are phase-reconstructed such that the expected attenuation, differential phase and dark-field images are obtained. Since the specimen

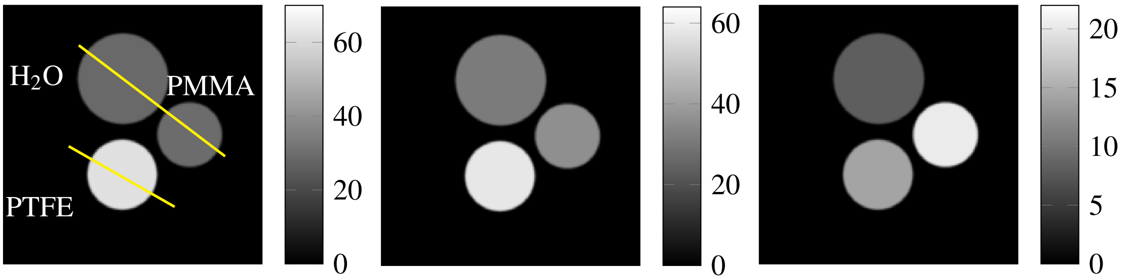

(a) Ground Truth μ_0 (b) Ground Truth δ_0 (c) Ground Truth σ_0

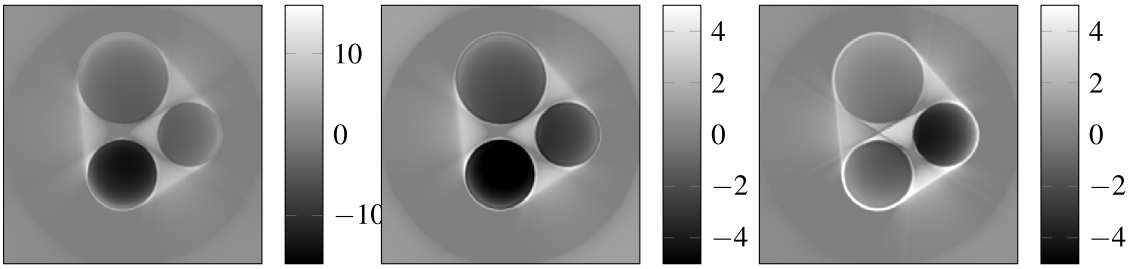

(d) Filtered Backprojection $\Delta\mu = \mu_{FBP} - \mu_0$ (e) Filtered Backprojection $\Delta\delta = \delta_{FBP} - \delta_0$ (f) Filtered Backprojection $\Delta\sigma = \sigma_{FBP} - \sigma_0$

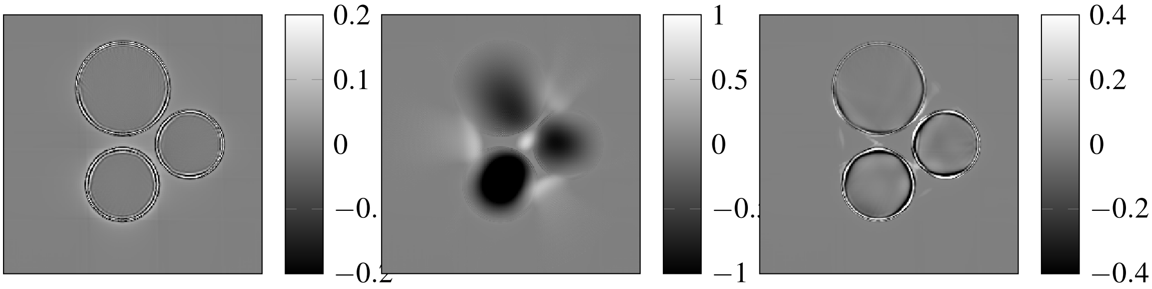

(g) Iterative Reconstruction $\Delta\mu = \mu_{reco} - \mu_0$ (h) Iterative Reconstruction $\Delta\delta = \delta_{reco} - \delta_0$ (i) Iterative Reconstruction $\Delta\sigma = \sigma_{reco} - \sigma_0$

Figure 9.20: The first row shows ground truth data for absorption, refractive decrement and scatter at a mean energy of $E_0 = 38.8\,\text{keV}$. The two yellow lines define crosssections shown in Fig. 9.21. The range of the refractive decrement δ was scaled to be in the same range as the attenuation coefficient by multiplication of 0.2×10^8. The second row shows the difference between the direct reconstruction using filtered backprojection and ground truth data. The third row shows the difference between the iterative reconstruction and ground truth data. The error of the iterative reconstruction is a magnitude smaller than for the filtered backprojection reconstruction.

can be assumed homogeneous materials, i.e. they yield no micro-scattering properties, the scatter coefficient is set to zero. However, beam hardening effects are inherently included by the polychromatic model, thus an artificial dark-field is simulated. Its magnitude can then be compared to the dark-field measured in experiment.

As an example the aluminum pipe introduced in Fig. 7.5j is chosen. Other imaged specimen contained iodine, brass or copper. Aluminum, however, has one advantage over the latter: there are no K-edges in the energy range of interest. Thus, the energy dependence of the attenuation coefficient is a steady function and should be a fairly well approximated by Eqn. 8.2.

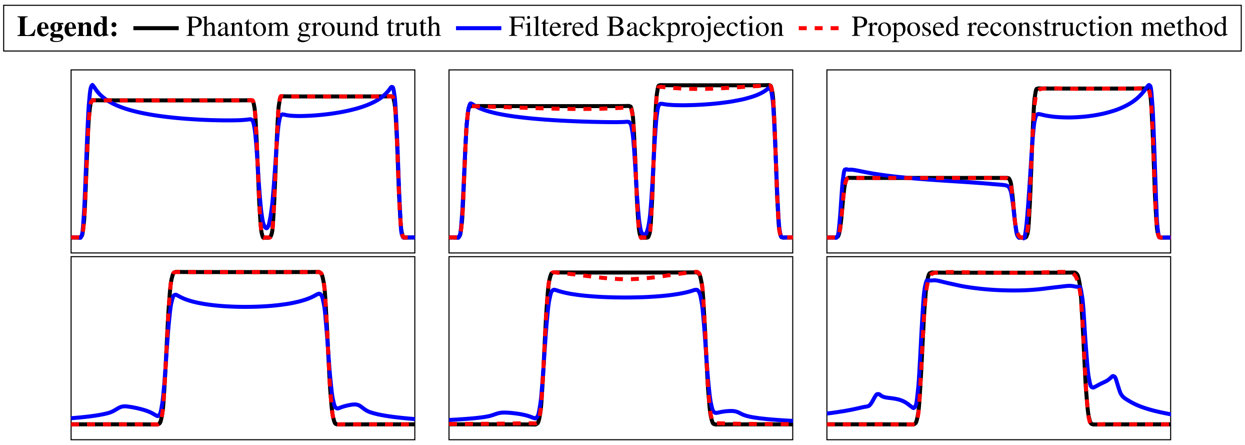

(a) Attenuation (b) Refractive decrement (c) Scatter

Figure 9.21: Two cross-sections through the reconstructed data as visualized in Fig. 9.20. Black: Phantom ground truth, Blue: Filtered Backprojection, Red (dashed): Proposed reconstruction method. For all images, the iteratively reconstruction and ground truth are in high agreement.

The acceleration voltage was 60 kVp which results in a mean energy of about $E = 39\,\mathrm{keV}$. Filtered back projection and iterative reconstruction are shown in Fig. 9.22. The coefficient for the polychromatic model were $C_\mu = -3$, $C_\delta = -2$, and $C_\sigma = -3$. The spectrum as divided into 20 energy bins. Cross-sections for all three images are plotted in Fig. 9.22. Cupping artifacts in the attenuation image are observed. Additionally, beam-hardening effects lead to an artificial dark-field eventually leading to non-zero entries in the scatter image. The polychromatic reconstruction does reduce cupping artifacts, but can not cope with the polychromatic induced scatter image.

Aluminum Pipe

For a proper analysis why it fails to deliver, the phantom was rebuilt synthetically and subsequently polychromatic forward projected. For this, the mean values for attenuation and refractive decrement were extracted from the reconstructed image and assigned to the corresponding regions in the phantom. As explained above, the scatter coefficients are zero over the whole image. The measured and expected visibilities are shown in Fig. 9.24. For the measured data, a positive dark-field is observed inside the aluminum region and a slightly negative dark-field in the air region. This is different for the simulated data, where only a negative dark-field is observed except of edge-induced effects. The magnitude of positive dark-field at the energies is of the same dimension.

Negative dark-field values require special consideration. At first glance, this seems unphysical since a negative dark-field would correspond to a higher object visibility compared to the reference. For a meaningful physical interpretation, one needs to bear in mind that the reference visibility - see Eqn. 8.15 - is given by a weighted integration. On the one hand, the object is homogeneous, and thus, at least no drop in visibility is expected due micro-angle scattering. However, the shape of spectrum changes due to hardened beam. Consequently, depending on the shape of the energy-visibility curve, see Fig. 8.8, the reference visibility of the hardened spectrum may now be either larger or smaller than the initial reference visibility.

For tomography a negative dark-field may lead to negative scatter values. Negative coefficients are not observed for attenuation imaging, since an X-ray beam can not gain energy while traversing the material. In

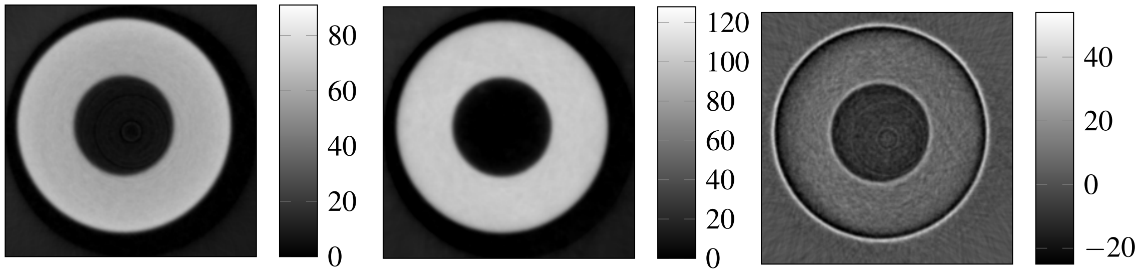
80
60
40
20
0
120
100
80
60
40
20
0
40
20
0
−20

(a) FBP μ (b) FBP δ (c) FBP σ

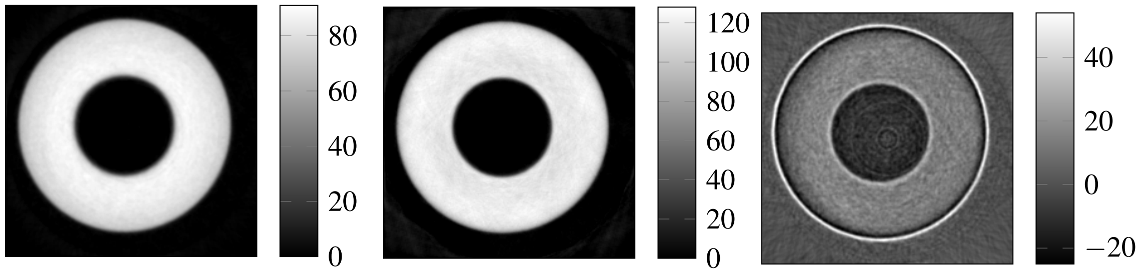
80
60
40
20
0
120
100
80
60
40
20
0
40
20
0
−20

(d) It. Reco. μ (e) It. Reco. δ (f) It. Reco. σ

Figure 9.22: Reconstructions of the aluminum pipe phantom. Filtered back projection are shown in figures (a-c). Iterative reconstruction results are shown in figures (d-f). Cupping artifacts have been removed in the attenuation image. The scatter image yields non-zero coefficients due to beam hardening effects. Application of the polychromatic reconstruction is not able to remove those.

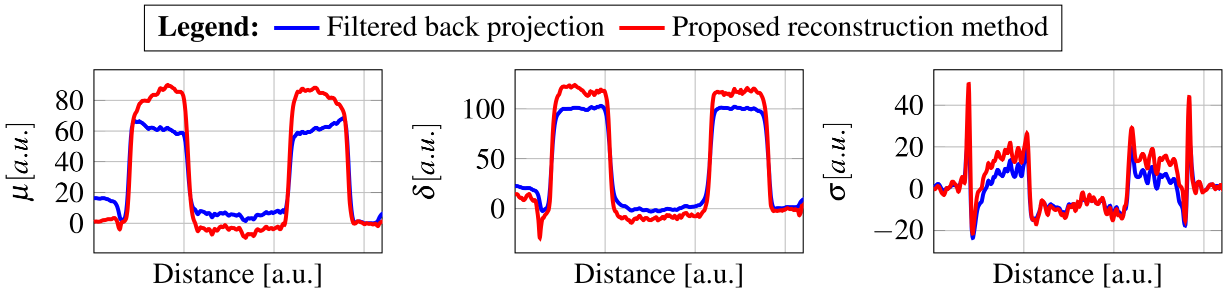

(a) Attenuation (b) Phase (c) Scatter

Figure 9.23: Cross-sections through the reconstruction results shown in Fig. 9.22.

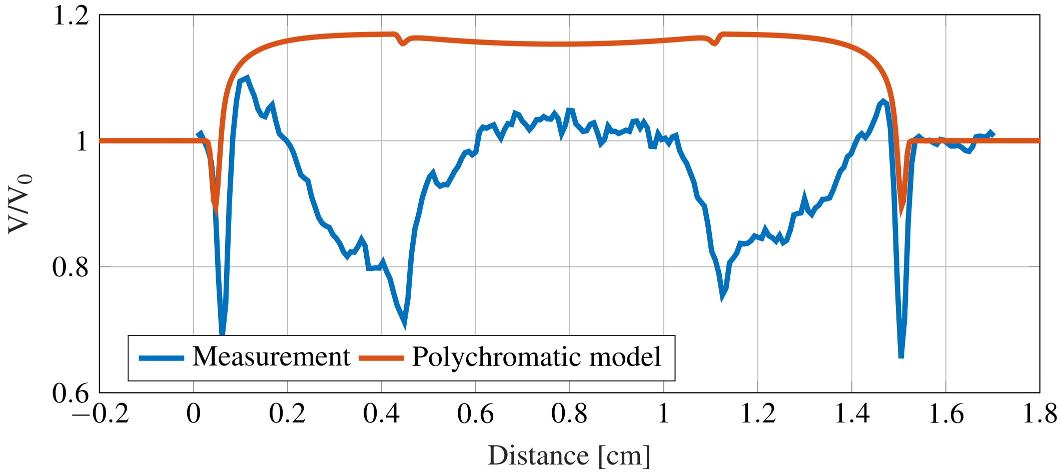

Figure 9.24: In this experiment an aluminum tube- introduced in Fig. 9.22 - was measured at 60 kVp. The plots show the measured (blue) and expected (orange) visibility. An increase in visibility is expected for the polychromatic model in the region of the aluminum tube. On the contrary, the measurement shows contradictory behavior.

fact, one might even set a zero constraint for the attenuation coefficient. For Talbot-Lau imaging, negative scatter values correspond to generation of visibility.

Figure 9.25 depicts the filtered back projection results of the simulated aluminum phantoms. Similar cupping artifacts as in the measured case are observed. Only little dispersions effects are visible for the refractive decrement. On the contrary, only negative scatter coefficients are observed which is in contradiction to the measured data. This discrepancy explains why the iterative reconstruction fails to remove the polychromatic artifacts. Variation of the model parameters for the attenuation coefficient (e.g. to $C_\mu = 3.5$) or the scatter coefficients did not significantly change the result.

One possible explanation of this disparity might be Compton scattering component that is not considered in the proposed model. This component might stem from scattering of the object, the X-ray chamber or other sources. To understand the influence of this effect on the visibility, we model it by a constant offset $N_{Compton}$ on the phase-stepping curve to

$$N_{i,s} = N_i \cdot (1 + V_i \cdot \cos\phi_{is}) + N_{Compton} \quad . \tag{9.3}$$

Assuming an object of size d with homogeneous attenuation and scatter coefficient, μ and σ, the expected visibility is approximated without considering Compton scatter by

$$V = \frac{A_0 \cdot e^{-\mu \cdot d} \cdot e^{-\sigma \cdot d}}{N_0 \cdot e^{-\mu \cdot d}} = V_0 \cdot e^{-\mu \cdot d} \quad , \tag{9.4}$$

where A_0 denotes the reference amplitude. With considering the Compton scatter one has

$$V' = \frac{A_0 \cdot e^{-\mu \cdot d} \cdot e^{-\sigma \cdot d}}{N_0 \cdot e^{-\mu \cdot d} + N_{Compton}} \quad . \tag{9.5}$$

From these two equations it follow that $V \neq V'$ if the Compton term is not negligible. To support this claim, a syringe filled with iodine - see Fig. 7.5d - was measured once with and once without a lead collimator at an acceleration voltage of $E = 60\,\text{kV}$. The lead collimator was placed directly after the X-ray

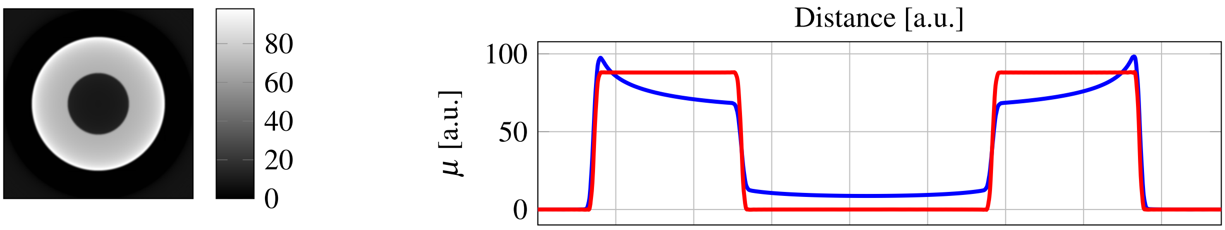

(a) Attenuation μ

(b) Cross-section

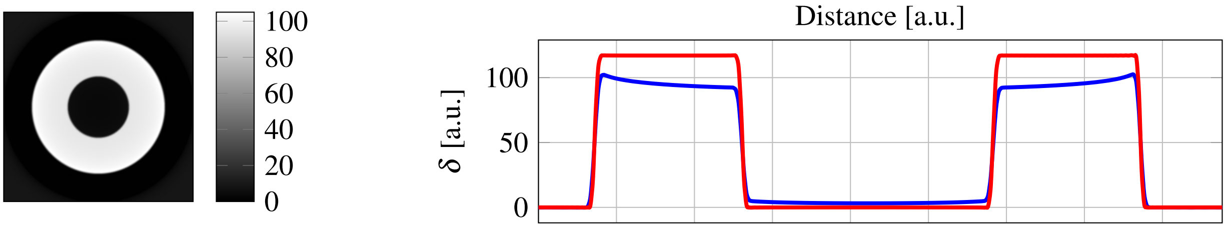

(c) Refractive decrement δ

(d) Cross-section

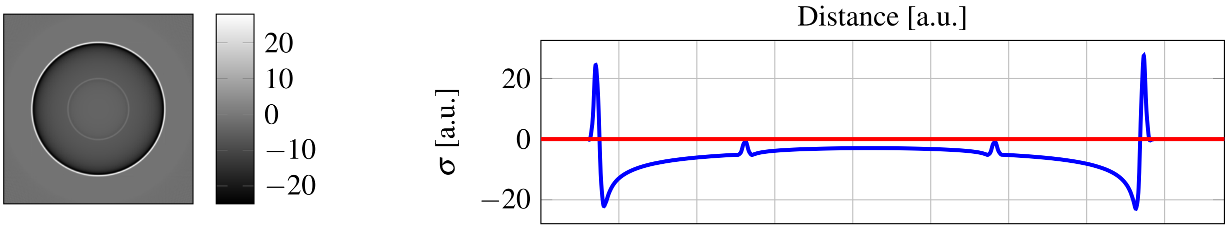

(e) Scatter σ

(f) Cross-section

Figure 9.25: Figure (a,c,e) show filtered back projection reconstructions of simulated Talbot Lau data. For this an aluminum tube was forward projected with the polychromatic model with an 60 kV spectrum. Cross-sections of the ground truth (red) and reconstruction (blue) are shown in Fig. (b,d,f). Beam hardening and dispersions artifacts are visible in the attenuation and phase image. Moreover, a negative scatter index occurs due to beam hardening effects.

source. Figure 9.26 shows that both measurements exhibit a drop in visibility even if the object should not yield any small-angle properties, but the magnitude of the decrease varies significantly between the two measurements. This difference indicates that there is indeed a scatter component that has a substantial effect on interferometer. However, the discrepancy between the expected and measured dark-field could not be resolved even by addition of the collimator. Until now, we have not fully understood the physical reasons for this. One reason might be that additional scattering - such as from the object or other parts of the experimental setup - are not removed by the collimator. Due to lack of time, no further experiments could be performed to clarify this issue.

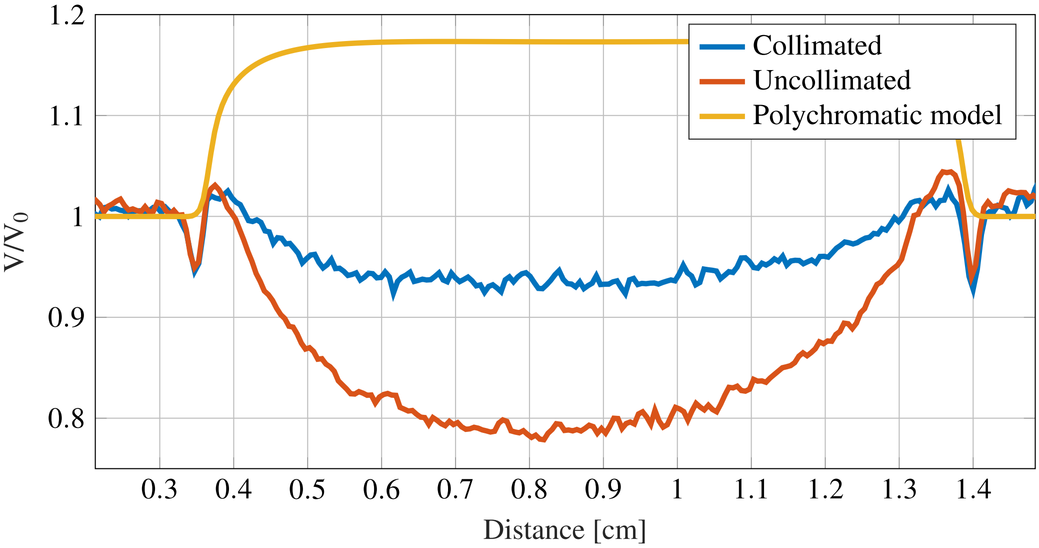

Figure 9.26: In this experiment a syringe filled with iodine - introduced in Fig. 7.5d - was measured with and without a lead collimator. The plots show the measured dark-field for the collimated (orange) and uncollimated (blue) measurement as well as the expected dark-field which is calculated by applying the polychromatic model (yellow). The visibility is decreased for the collimated measurement. However, the simulated dark-field still differs from the measured one.

Chapter 10

Conclusion and Outlook

A reconstruction framework for Talbot-Lau tomography employing Kaiser-Bessel functions was developed in chapter 5. The framework allows for simultaneous reconstruction of Talbot-Lau data acquired with the full and interlaced acquisition scheme without prior phase retrieval. Reconstruction with typical resolutions used in medical imaging, e.g. 512×512, are possible within reasonable time and computational effort. A detailed description of the framework's underlying physical and mathematical fundamentals are found in the chapters 2,3 and 4.

The reconstruction framework was tested in Sec. 9.1 with several case studies comprising real and simulated data. For each specimen, Talbot data was reconstructed by both, filtered back projection and the monochromatic iterative reconstruction. A finding of this thesis is that the iterative reconstruction performs better for data affected by heavy noise in the differential phase and dark-field image. In particular, streak artifacts that occur in phase and scatter image are reduced compared to analytic reconstruction requiring prior phase-retrieval.

Furthermore, an in-depth analysis of the monochromatic reconstruction algorithm was conducted in Sec. 9.2. The influence on the reconstruction results of several parameters such as noise, reference visibility or number of projections was investigated.

This thesis contributes to the state of the art with the proposal of two novel algorithms. First, an alternative optimization approach that exploits information of the second derivative is suggested in Sec. 8.3. The performance of this algorithm was shortly examined in Sec. 9.3. The obtained results are ambiguous. For some special cases, the proposed method provides a faster convergence. However, for some others cases, no change in the convergence behavior was observed. A thorough analysis to fully understand (dis)advantages has not been possible due to time constraints.

The second and main contribution is the proposal of a novel reconstruction algorithm that incorporates a polychromatic model of grating based phase-contrast imaging. The biggest benefit of polychromatic modeling is that it implicitly avoids beam-hardening artifacts. To our knowledge, this is the first tomographic reconstruction algorithm that is specifically designed for polychromatic Talbot-Lau imaging. For synthetic phantom data, the proposed method is able to correct beam-hardened corrupted data for reconstructions of attenuation, phase and scatter. Results for attenuation and scatter are highly accurate. The phase image is also greatly improved over a naive reconstruction, but still exhibits slight cupping artifacts. Also, we observed that reconstruction of attenuation and scatter converges much faster than reconstruction of the phase. We believe that the slow convergence can be efficiently targeted with a specially tailored optimization algorithm, for instance with an adaption of the method proposed in Sec. 8.3.

Additionally, the algorithm was evaluated on real data. The measured Talbot-Lau data are affected by beam-hardening in the attenuation image, leading to cupping artifacts in the reconstruction. Moreover, due to the hardened spectrum a dark-field is observed which propagates into the scatter image as artifacts. Application of the proposed polychromatic algorithm could not remove these artifacts. An analysis of the forward model with synthetic data revealed that the model prediction is not in accordance with the measured data. This discrepancy could not be resolved and is not yet understood.

For future work there are still many open questions. Since development of the reconstruction framework was a major task, there has not been enough time to fully investigate the reconstruction algorithm itself. In future work, one could perform further experiments to specify in which imaging scenarios the iterative reconstruction is advantageous over analytic reconstruction techniques.

Furthermore, the framework can easily be enhanced with additional and novel reconstruction algorithms. It leaves place to easily play around with novel ideas to improve reconstruction. One could think of adaption of advanced reconstruction techniques known from conventional attenuation tomography. But also in regards to physics more challenging topics are possible. In recent publications, Talbot-Lau imaging with two phase grating instead of a phase grating and an analyzer grating arouse interest to the phase-contrast community. This imaging process can be easily modeled and implemented with our framework and allows for derivation of novel reconstruction techniques for phase-contrast imaging.

Another important aspect will be to compare the presented method to state-of-the-art beam hardening corrections.

List of Figures

1.1 Medical images (Talbot-Lau imaging) 4
1.2 Talbot-Lau tomography of a mouse 5

2.1 The electromagnetic spectrum with a focus on the X-ray range [119] and corresponding applications indicated. 8
2.2 Bremsstrahlung 9
2.3 characteristic radiation 9
2.4 The X-ray energy spectrum generated by an X-ray tube. 10
2.5 The functional components of an X-ray tube. 10
2.6 Cross-section examples 11
2.7 Wavepropagation through object. 14

3.1 Talbot effect 16
3.2 Simulation of Talbot effect 16
3.3 Lau effect 17
3.4 Talbot-Lau interferometer 17
3.5 Example Talbot-Lau wiht gummybears 18
3.6 Phase-stepping curve 19

4.1 Tomography: Projection geometry 24
4.2 Projections from two different angles. 24
4.3 Fourier slice theorem 25
4.4 2D inverse Fourier transform 25
4.5 Filtered back projection 26
4.6 Example for a tomographic projection with 9 unknowns and 9 measurements. 27
4.7 Illustration of gradient descent in 2D and 1D. 28
4.8 Phase steping sinograms 32
4.9 Talbot-Lau sinograms. 32
4.10 Talbot-Lau Example Filtered Back Projection. 32
4.11 Gradient in Talbot-Lau tomography. 37

5.1 Kaiser-Bessel Function and its (differential) footprint on the detector. The blue and orange curves denote the conventional and differential footprint respectively. 40
5.2 Composition of several blobs provide a smooth object function $f(r)$. The strength of each blob i is denoted by f_i. 40
5.3 Rectangular and blob dicretization. 41

5.4 Images (a,b,c) show the the radial profiles of the Kaiser-Bessel function for the blob parameter $m = 0$, $m = 1$, and $m = 2$, respectively. Each subfigure comprises plots where the second blob parameter α takes the values 0, 2, 5, and 10. 42
5.5 The differential footprint of the Kaiser-Bessel function for parameters varying in m and α. 43
5.6 The conventional footprint of the Kaiser-Bessel function for parameters varying in m and α. 43
5.7 Matrix element of the conventional footprint. 44
5.8 Matrix element of the differential footprint. 44
5.9 Effect of blob on detector. 44

6.1 Example of 2D phase unwrapping. Data was acquired with the high energy setup at ECAP. 47
6.2 Reference phase drift. 48
6.3 Reference phase drift (Plot). 48
6.4 Projection center of mass (Geometry). 49
6.5 Projecton center of mass (Plot). 49

7.1 Energy-visibilty curve 54
7.2 The setup parameter of the current high energy setup at ECAP. In table 7.1 O and D denote the location of the object and detector respectively. 54
7.3 Energy-visibilty curve 54
7.4 The setup parameters of the Talbot-Lau inteferometer used in [116]. 54
7.5 An overview of the specimen that have been imaged throughout this thesis. 56
7.6 CXI Phantom (Ground truth + FBP). 57
7.7 CXI sinograms 58
7.8 Three cylinder phantom 59
7.9 Shepp Logan phantom. 59
7.10 Mouse sampe (original). 60
7.11 Mouse sample (with Ring artifact correction) 60

8.1 Example reconstruction from Ritter *et al.* [92] (2013) 62
8.2 Example reconstruction from the second publication of Ritter *et al.* [94] (2016). 62
8.3 Example reconstruction from Brendel *et al.* [19]. 63
8.4 Tomographic reconstruction examples of the work of Andreas Wolf [123]. 64
8.5 Beam-hardening example. 65
8.6 Dispersion example. 65
8.7 Simulation results for the scatter coefficient of different porous materials. 66
8.8 Spectrum and visbilty curve. 66
8.9 The continuous spectrum is subdivided into several energy bins. 68
8.10 Schematic example of polychromatic model. 68
8.11 Hessian steepest descent 71
8.12 Newton step. 71

9.1 Tomographic reconstructions of simulated data (CXI) 76
9.2 Reconstruction of phantom shown in (Fig. 7.5a) 77
9.3 Reconstruction of Thomas Weber phantom 77
9.4 Sinogram data of phantom shown in (Fig. 7.5h) 78
9.5 Reconstruction of phantom shown in (Fig. 7.5h) 78
9.6 Reconstruction of bone with fissure. 79

9.7 Reconstruction results of the ex-vivo mouse sample. Filtered back projection and iterative reconstruction do not differ much. The iterative reconstruction algorithms seems to provide a sharper image of the refractive decrement and scatter. 80
9.8 The plot shows the structural similarity of the mouse sample for the three images in respect to the iteration number. The filtered back projection reconstructions were used as ground truth data for calculation of the SSIM. For a better visualization only the first 100 iterations are plotted. The attenuation image convergences the fastest. 80
9.9 Analysis: Influence of noise level 81
9.10 Analysis: Influence of object size 82
9.11 Analysis: Influence of reference visibility 83
9.12 Analysis: Number of reference phase steps (Full acquisition) 83
9.13 Interlaced, 100 projections, sinograms 85
9.14 Interlaced, 1200 projections, sinograms 85
9.15 Interlaced, low photon CT plots 86
9.16 Interlaced, high photon CT plots 86
9.17 Second derivative vs. standard reconstruction for a detector size of 10cm. 87
9.18 Second derivative vs. standard reconstruction for a detector size of 20cm. 87
9.19 Second derivative vs. standard reconstruction for a detector size of 30cm. 87
9.20 Simulation results for polychromatic model 90
9.21 Cross-sections for simulated, polychromatic data. 91
9.22 Reconstruction of aluminum phantom. 92
9.23 Cross-sections through the reconstruction results shown in Fig. 9.22. 92
9.24 Real data with beam-hardening dark-field. 93
9.25 Simulated Aluminium phantom. 94
9.26 In this experiment a syringe filled with iodine - introduced in Fig. 7.5d - was measured with and without a lead collimator. The plots show the measured dark-field for the collimated (orange) and uncollimated (blue) measurement as well as the expected dark-field which is calculated by applying the polychromatic model (yellow). The visibility is decreased for the collimated measurement. However, the simulated dark-field still differs from the measured one. 95

Bibliography

[1] Bipin K. Agarwal. *X-Ray Spectroscopy*. Springer, 1991. ISBN 3540507191. URL `http://www.ebook.de/de/product/21743834/bipin_k_agarwal_x_ray_spectroscopy.html`.

[2] Jens Als-Nielsen and Des McMorrow. *Elements of Modern X-ray Physics*. Wiley, 2001. ISBN 978-0471498582. URL `https://www.amazon.com/Elements-Modern-X-ray-Physics-Als-Nielsen/dp/0471498580?SubscriptionId=0JYN1NVW651KCA56C102&tag=techkie-20&linkCode=xm2&camp=2025&creative=165953&creativeASIN=0471498580`.

[3] David Attwood. *Soft X-Rays and Extreme Ultraviolet Radiation: Principles and Applications*. Cambridge University Press, 2007. ISBN 978-0521029971. URL `https://www.amazon.com/Soft-X-Rays-Extreme-Ultraviolet-Radiation/dp/052102997X?SubscriptionId=0JYN1NVW651KCA56C102&tag=techkie-20&linkCode=xm2&camp=2025&creative=165953&creativeASIN=052102997X`.

[4] S.G. Azevedo, D.J. Schneberk, J.P. Fitch, and H.E. Martz. Calculation of the rotational centers in computed tomography sinograms. *IEEE Transactions on Nuclear Science*, 37(4):1525–1540, 1990. doi: 10.1109/23.55866.

[5] Julia F. Barrett and Nicholas Keatba. Artifacts in CT: Recognition and avoidance. *RadioGraphics*, 24(6):1679–1691, Nov. 2004. doi: 10.1148/rg.246045065.

[6] F. L. Bayer, S. Hu, A. Maier, T. Weber, G. Anton, T. Michel, and C. P. Riess. Reconstruction of scalar and vectorial components in x-ray dark-field tomography. *Proceedings of the National Academy of Sciences*, 111(35):12699–12704, aug 2014. doi: 10.1073/pnas.1321080111.

[7] M. Bech, O. Bunk, T. Donath, R. Feidenhans'l, C. David, and F. Pfeiffer. Quantitative x-ray dark-field computed tomography. *Physics in Medicine and Biology*, 55(18):5529–5539, Aug. 2010. ISSN 1361-6560. doi: 10.1088/0031-9155/55/18/017. URL `http://dx.doi.org/10.1088/0031-9155/55/18/017`.

[8] S. Becker and Yann Lecun. *Improving the convergence of back-propagation learning with second-order methods*, pages 29–37. Morgan Kaufmann, 1989.

[9] Burkhard Beckhoff, habil. Birgit Kanngießer, Norbert Langhoff, Reiner Wedell, and Helmut Wolff, editors. *Handbook of Practical X-Ray Fluorescence Analysis*. Springer Nature, 2006. doi: 10.1007/978-3-540-36722-2.

[10] Rolf Behling. *Modern Diagnostic X-Ray Sources*. Apple Academic Press Inc., 2015. ISBN 1482241323. URL `http://www.ebook.de/de/product/23641682/rolf_behling_modern_diagnostic_x_ray_sources.html`.

[11] Marcel Beister, Daniel Kolditz, and Willi A. Kalender. Iterative reconstruction methods in x-ray CT. *Physica Medica*, 28(2):94–108, Apr. 2012. doi: 10.1016/j.ejmp.2012.01.003.

[12] Martin J Berger, JH Hubbell, SM Seltzer, J Chang, JS Coursey, Ry Sukumar, DS Zucker, and K Olsen. Xcom: Photon cross sections database. *NIST Standard reference database*, 8(1):3587–3597, 1998.

[13] M.J. Berger and J.H. Hubbell. XCOM: Photon cross sections on a personal computer. Technical report, July 1987.

[14] Nicholas Bevins, Joseph Zambelli, Ke Li, Zhihua Qi, and Guang-Hong Chen. Beam hardening in x-ray differential phase contrast computed tomography. In Norbert J. Pelc, Ehsan Samei, and Robert M. Nishikawa, editors, *Medical Imaging 2011: Physics of Medical Imaging*. SPIE-Intl Soc Optical Eng, March 2011. doi: 10.1117/12.878483.

[15] Rolf-Dieter Bippus, Thomas K?hler, Frank Bergner, Bernhard Brendel, Eberhard Hansis, and Roland Proksa. Projector and backprojector for iterative ct reconstruction with blobs using cuda. Aug. 2011. URL `http://citeseerx.ist.psu.edu/viewdoc/download?doi=10.1.1.919.2013&rep=rep1&type=pdf`.

[16] U. Bonse and M. Hart. An x-ray interferometer with long separated interfering beam paths. *Applied Physics Letters*, 7(4):99, aug 1965. ISSN 00036951. doi: 10.1063/1.1754330. URL `http://dx.doi.org/10.1063/1.1754330`.

[17] Max Born and Emil Wolf. *Principles of Optics*. Cambridge University Pr., 2002. ISBN 0521642221. URL `http://www.ebook.de/de/product/3242885/max_born_emil_wolf_principles_of_optics.html`.

[18] Stephen Boyd and Lieven Vandenberghe. *Convex Optimization*. Cambridge University Press, 2004. ISBN 0521833787. URL `http://www.ebook.de/de/product/3677442/stephen_boyd_lieven_vandenberghe_convex_optimization.html`.

[19] Bernhard Brendel, Maximilian von Teuffenbach, Peter B. No??l, Franz Pfeiffer, and Thomas Koehler. Penalized maximum likelihood reconstruction for x-ray differential phase-contrast tomography. *Medical Physics*, 43(1):188–194, Dec. 2015. doi: 10.1118/1.4938067. URL `http://dx.doi.org/10.1118/1.4938067`.

[20] Jerrold T. Bushberg, J. Anthony Seibert, and Edwin M. Leidholdt. *Essential Physics of Medical Imaging*. LIPPINCOTT RAVEN, 2011. ISBN 0781780578. URL `http://www.ebook.de/de/product/15362124/jerrold_t_bushberg_j_anthony_seibert_edwin_m_leidholdt_essential_physics_of_medical_imaging.html`.

[21] Thorsten M. Buzug. *Computed Tomography*. Springer Berlin Heidelberg, 2008. URL `http://www.ebook.de/de/product/8899158/thorsten_m_buzug_computed_tomography.html`.

[22] Michael Chabior. *Contributions to the characterization of grating-based x-ray phase-contrast imaging*. PhD thesis, TU Dresden, Sep. 2011. URL `https://core.ac.uk/download/pdf/35189083.pdf`.

[23] Michael Chabior, Tilman Donath, Christian David, Oliver Bunk, Manfred Schuster, Christian Schroer, and Franz Pfeiffer. Beam hardening effects in grating-based x-ray phase-contrast imaging. *Medical Physics*, 38(3):1189, Feb. 2011. doi: 10.1118/1.3553408.

[24] M. Costantini. A novel phase unwrapping method based on network programming. *IEEE Transactions on Geoscience and Remote Sensing*, 36(3):813–821, may 1998. doi: 10.1109/36.673674.

[25] Tim Dahmen, Holger Kohr, Niels de Jonge, and Philipp Slusallek. Matched backprojection operator for combined scanning transmission electron microscopy tilt- and focal series. *Microscopy and Microanalysis*, 21(03):725–738, jun 2015. doi: 10.1017/s1431927615000525.

[26] G. M. D'Ariano and P. Lo Presti. Quantum tomography for measuring experimentally the matrix elements of an arbitrary quantum operation. *Physical Review Letters*, 86(19):4195–4198, May 2001. doi: 10.1103/physrevlett.86.4195.

[27] P C Diemoz, M Endrizzi, C K Hagen, C Rau, A Bravin, R D Speller, I K Robinson, and A Olivo. Edge illumination x-ray phase-contrast imaging: nanoradian sensitivity at synchrotrons and translation to conventional sources. *Journal of Physics: Conference Series*, 499:012006, apr 2014. doi: 10.1088/1742-6596/499/1/012006.

[28] Tilman Donath, Franz Pfeiffer, Oliver Bunk, Christian Gr??nzweig, Eckhard Hempel, Stefan Popescu, Peter Vock, and Christian David. Toward clinical x-ray phase-contrast CT. *Investigative Radiology*, page 1, May 2010. doi: 10.1097/rli.0b013e3181e21866.

[29] I.A. Elbakri and J.A. Fessler. Statistical image reconstruction for polyenergetic x-ray computed tomography. *IEEE Transactions on Medical Imaging*, 21(2):89–99, Feb. 2002. doi: 10.1109/42.993128.

[30] H Erdogan and J A Fessler. Ordered subsets algorithms for transmission tomography. *Physics in Medicine and Biology*, 44(11):2835–2851, Oct. 1999. doi: 10.1088/0031-9155/44/11/311.

[31] Robley Dunglison Evans. *Atomic Nucleus*. Krieger Pub Co, 1982. ISBN 978-0898744149. URL `https://www.amazon.com/Atomic-Nucleus-Robley-Dunglison-Evans/dp/0898744148?SubscriptionId=0JYN1NVW651KCA56C102&tag=techkie-20&linkCode=xm2&camp=2025&creative=165953&creativeASIN=0898744148`.

[32] L. A. Feldkamp, G. Jesion, and D. J. Kubinski. Fundamental aspects of micro-CT in cone-beam geometry. In Donald O. Thompson and Dale E. Chimenti, editors, *Review of Progress in Quantitative Nondestructive Evaluation*, pages 381–388. Springer US, 1989. ISBN 978-1-4612-8097-2. doi: 10.1007/978-1-4613-0817-1_49. URL `http://dx.doi.org/10.1007/978-1-4613-0817-1_49`.

[33] Jeffrey Fessler. Statistical image reconstruction methods for transmission tomography. In *Handbook of Medical Imaging, Volume 2. Medical Image Processing and Analysis*, pages 1–70. SPIE-Intl Soc Optical Eng, 2001. doi: 10.1117/3.831079.ch1.

[34] Joseph W. Goodman. *Introduction to Fourier optics*, volume 35. Roberts & Co, 3rd ed. edition, May 2005. ISBN 978-0974707723. doi: 10.1117/1.601121. URL `http://dx.doi.org/10.1117/1.601121`.

[35] B. Goris, W. Van den Broek, K.J. Batenburg, H. Heidari Mezerji, and S. Bals. Electron tomography based on a total variation minimization reconstruction technique. *Ultramicroscopy*, 113:120–130, Feb. 2012. doi: 10.1016/j.ultramic.2011.11.004.

[36] Viktor Haase, Oliver Taubmann, Yixing Huang, Gregor Krings, Günter Lauritsch, Andreas Maier, and Alfred Mertins. Make the most of time temporal extension of the itv algorithm for 4d cardiac c-arm ct. In *Bildverarbeitung für die Medizin 2016*, pages 170–175. Springer, 2016.

[37] Dieter Hahn, Pierre Thibault, Andreas Fehringer, Martin Bech, Thomas Koehler, Franz Pfeiffer, and Peter B. Noel. Statistical iterative reconstruction algorithm for x-ray phase-contrast CT. *Scientific Reports*, 5(1), June 2015. doi: 10.1038/srep10452.

[38] Katharina Hahn, Harald Sch?ndube, Karl Stierstorfer, Joachim Hornegger, and Frédéric Noo. A comparison of linear interpolation models for iterative CT reconstruction. *Medical Physics*, 43(12): 6455–6473, nov 2016. doi: 10.1118/1.4966134.

[39] Amy K. Hara, Robert G. Paden, Alvin C. Silva, Jennifer L. Kujak, Holly J. Lawder, and William Pavlicek. Iterative reconstruction technique for reducing body radiation dose at CT: Feasibility study. *American Journal of Roentgenology*, 193(3):764–771, Sep. 2009. doi: 10.2214/ajr.09.2397.

[40] Eugene Hecht. *Optics*. ADDISON WESLEY PUB CO INC, 2016. ISBN 0133977226. URL `http://www.ebook.de/de/product/22824811/eugene_hecht_optics.html`.

[41] G T Herman. Correction for beam hardening in computed tomography. *Physics in Medicine and Biology*, 24(1):81–106, Jan. 1979. doi: 10.1088/0031-9155/24/1/008.

[42] Florian Horn, Christian Hauke, Sebastian Lachner, Veronika Ludwig, Georg Pelzer, Jens Rieger, Max Schuster, Maria Seifert, Johannes Wandner, Andreas Wolf, et al. High-energy x-ray grating-based phase-contrast radiography of human anatomy. In *SPIE Medical Imaging*, pages 97830P–97830P. International Society for Optics and Photonics, 2016. doi: 10.1117/12.2216893.

[43] D Huang, E. Swanson, C. Lin, J. Schuman, W. Stinson, W Chang, M. Hee, T Flotte, K Gregory, C. Puliafito, and al. et. Optical coherence tomography. *Science*, 254(5035):1178–1181, Nov. 1991. doi: 10.1126/science.1957169.

[44] Y. Huang, O. Taubmann, X. Huang, V Haase, G. Lauritsch, and A. Maier. A new weighted anisotropic total variation algorithm for limited angle tomography. In *2016 IEEE 13th International Symposium on Biomedical Imaging (ISBI)*. Institute of Electrical and Electronics Engineers (IEEE), Apr. 2016. doi: 10.1109/isbi.2016.7493336.

[45] J. Jahns and A.W. Lohmann. The lau effect (a diffraction experiment with incoherent illumination). *Optics Communications*, 28(3):263–267, Mar. 1979. doi: 10.1016/0030-4018(79)90316-x.

[46] Torben Haugaard Jensen, Martin Bech, Irene Zanette, Timm Weitkamp, Christian David, Hans Deyhle, Simon Rutishauser, Elena Reznikova, Jürgen Mohr, Robert Feidenhans'l, and Franz Pfeiffer. Directional x-ray dark-field imaging of strongly ordered systems. *Physical Review B*, 82(21), dec 2010. ISSN 1098-0121. doi: 10.1103/physrevb.82.214103. URL `http://dx.doi.org/10.1103/physrevb.82.214103`.

[47] Eric Jones, Travis Oliphant, Pearu Peterson, et al. SciPy: Open source scientific tools for Python, 2001. URL `http://www.scipy.org/`. [Online; accessed <today>].

[48] Peter M. Joseph. An improved algorithm for reprojecting rays through pixel images. *IEEE Transactions on Medical Imaging*, 1(3):192–196, nov 1982. doi: 10.1109/tmi.1982.4307572.

[49] Mario Juric, Željko Ivezić, Alyson Brooks, Robert H. Lupton, David Schlegel, Douglas Finkbeiner, Nikhil Padmanabhan, Nicholas Bond, Branimir Sesar, Constance M. Rockosi, Gillian R. Knapp, James E. Gunn, Takahiro Sumi, Donald P. Schneider, J. C. Barentine, Howard J. Brewington, J. Brinkmann, Masataka Fukugita, Michael Harvanek, S. J. Kleinman, Jurek Krzesinski, Dan Long, Jr. Eric H. Neilsen, Atsuko Nitta, Stephanie A. Snedden, and Donald G. York. The milky way tomography with SDSS. i. stellar number density distribution. *The Astrophysical Journal*, 673(2): 864–914, Feb. 2008. doi: 10.1086/523619.

[50] Sebastian Kaeppler, Florian Bayer, Thomas Weber, Andreas Maier, Gisela Anton, Joachim Hornegger, Matthias Beckmann, Peter A. Fasching, Arndt Hartmann, Felix Heindl, Thilo Michel, Gueluemser Oezguel, Georg Pelzer, Claudia Rauh, Jens Rieger, Ruediger Schulz-Wendtland, Michael Uder, David Wachter, Evelyn Wenkel, and Christian Riess. Signal decomposition for x-ray dark-field imaging. In *Medical Image Computing and Computer-Assisted Intervention – MICCAI 2014*, pages 170–177. Springer Nature, Sep. 2014. doi: 10.1007/978-3-319-10404-1_22.

[51] Sebastian Kaeppler, Maria Seifert, Florian Horn, Georg Pelzer, Jens Rieger, Thilo Michel, Andreas Maier, Gisela Anton, and Christian Riess. Talbot-lau x-ray phase contrast for tiling-based acquisitions without reference scanning. *Medical Physics*, mar 2017. doi: 10.1002/mp.12200.

[52] Avinash C. Kak and Malcolm Slaney. *Principles of Computerized Tomographic Imaging*. Society for Industrial & Applied Mathematics (SIAM), Jan. 2001. doi: 10.1137/1.9780898719277.

[53] O. Klein and Y. Nishina. ?ber die streuung von strahlung durch freie elektronen nach der neuen relativistischen quantendynamik von dirac. *Zeitschrift f?r Physik*, 52(11-12):853–868, nov 1929. doi: 10.1007/bf01366453.

[54] T. Koehler and B.J. Brendel. Empirical beam hardening correction for differential phase contrast ct, August 25 2016. URL `https://www.google.com/patents/US20160242726`. US Patent App. 15/031,819.

[55] Thomas Koehler, Bernhard Brendel, and Ewald Roessl. Iterative reconstruction for differential phase contrast imaging using spherically symmetric basis functions. *Medical Physics*, 38(8):4542, July 2011. doi: 10.1118/1.3608906. URL `http://dx.doi.org/10.1118/1.3608906`.

[56] Yiannis Kyriakou, Daniel Prell, and Willi A Kalender. Ring artifact correction for high-resolution micro CT. *Physics in Medicine and Biology*, 54(17):N385–N391, August 2009. doi: 10.1088/0031-9155/54/17/n02.

[57] E. Lau. Beugungserscheinungen an doppelrastern. *Annalen der Physik*, 437(7-8):417–423, 1948. doi: 10.1002/andp.19484370709.

[58] Robert M. Lewitt. Multidimensional digital image representations using generalized kaiser–bessel window functions. *Journal of the Optical Society of America A*, 7(10):1834, Oct. 1990. doi: 10.1364/josaa.7.001834.

[59] A.W. Lohmann and D.E. Silva. An interferometer based on the talbot effect. *Optics Communications*, 2(9):413–415, Feb. 1971. doi: 10.1016/0030-4018(71)90055-1.

[60] Andreas Maier, Hannes G. Hofmann, Martin Berger, Peter Fischer, Chris Schwemmer, Haibo Wu, Kerstin Mueller, Joachim Hornegger, Jang-Hwan Choi, Christian Riess, Andreas Keil, and Rebecca Fahrig. A software framework for cone-beam imaging in radiology. *Medical Physics*, 40(11): 111914, Nov. 2013. doi: 10.1118/1.4824926.

[61] A. Malecki, G. Potdevin, T. Biernath, E. Eggl, K. Willer, T. Lasser, J. Maisenbacher, J. Gibmeier, A. Wanner, and F. Pfeiffer. X-ray tensor tomography. *EPL (Europhysics Letters)*, 105(3):38002, feb 2014. ISSN 0295-5075. doi: 10.1209/0295-5075/105/38002. URL `http://dx.doi.org/10.1209/0295-5075/105/38002`.

[62] B. De Man, J. Nuyts, P. Dupont, G. Marchal, and P. Suetens. An iterative maximum-likelihood polychromatic algorithm for CT. *IEEE Transactions on Medical Imaging*, 20(10):999–1008, Oct. 2001. doi: 10.1109/42.959297.

[63] Bruno De Man and Samit Basu. Distance-driven projection and backprojection in three dimensions. *Physics in Medicine and Biology*, 49(11):2463–2475, may 2004. doi: 10.1088/0031-9155/49/11/024.

[64] Mark M. Meerschaert and Alla Sikorskii. *Stochastic Models for Fractional Calculus*. Gruyter, Walter de GmbH, 2011. URL `http://www.ebook.de/de/product/18345831/mark_m_meerschaert_alla_sikorskii_stochastic_models_for_fractional_calculus.html`.

[65] Thilo Michel, Jens Rieger, Gisela Anton, Florian Bayer, Matthias W Beckmann, J?rgen Durst, Peter A Fasching, Wilhelm Haas, Arndt Hartmann, Georg Pelzer, Marcus Radicke, Claudia Rauh, André Ritter, Peter Sievers, R?diger Schulz-Wendtland, Michael Uder, David L Wachter, Thomas Weber, Evelyn Wenkel, and Andrea Zang. On a dark-field signal generated by micrometer-sized calcifications in phase-contrast mammography. *Physics in Medicine and Biology*, 58(8):2713–2732, Apr. 2013. doi: 10.1088/0031-9155/58/8/2713.

[66] A. Michette and S. Pfauntsch. *X-Rays: The First Hundred Years*. John Wiley & Sons Inc, 1996. ISBN 0471965022. URL `https://www.amazon.com/X-Rays-First-Hundred-Alan-Michette/dp/0471965022?SubscriptionId=0JYN1NVW651KCA56C102&tag=techkie-20&linkCode=xm2&camp=2025&creative=165953&creativeASIN=0471965022`.

[67] Byung Jun Min. Unmatched projector/backprojector pair for demultiplexing in multipinhole emission computed tomography. *Optical Engineering*, 49(12):127004, dec 2010. doi: 10.1117/1.3518081.

[68] P. Modregger, F. Scattarella, B. R. Pinzer, C. David, R. Bellotti, and M. Stampanoni. Imaging the ultrasmall-angle x-ray scattering distribution with grating interferometry. *Physical Review Letters*, 108(4), jan 2012. doi: 10.1103/physrevlett.108.048101.

[69] Atsushi Momose and Jun Fukuda. Phase-contrast radiographs of nonstained rat cerebellar specimen. *Medical Physics*, 22(4):375–379, Apr. 1995. doi: 10.1118/1.597472.

[70] Atsushi Momose, Tohoru Takeda, Yuji Itai, and Keiichi Hirano. Phase–contrast x–ray computed tomography for observing biological soft tissues. *Nature Medicine*, 2(4):473–475, Apr. 1996. doi: 10.1038/nm0496-473.

[71] Atsushi Momose, Wataru Yashiro, Yoshihiro Takeda, Yoshio Suzuki, and Tadashi Hattori. Phase tomography by x-ray talbot interferometry for biological imaging. *Japanese Journal of Applied Physics*, 45(6A):5254–5262, June 2006. ISSN 0021-4922. doi: 10.1143/jjap.45.5254. URL `http://dx.doi.org/10.1143/jjap.45.5254`.

[72] Peter G. Morris. *Nuclear Magnetic Resonance Imaging in Medicine and Biology (Oxford science publications).* Oxford University Press, 1986. ISBN 978-0198551553. URL `https://www.amazon.com/Nuclear-Magnetic-Resonance-Medicine-publications/dp/019855155X?SubscriptionId=0JYN1NVW651KCA56C102&tag=techkie-20&linkCode=xm2&camp=2025&creative=165953&creativeASIN=019855155X`.

[73] Walter Munk, Peter Worcester, and Carl Wunsch. *Ocean Acoustic Tomography (Cambridge Monographs on Mechanics).* Cambridge University Press, 2009. ISBN 978-0521115360. URL `https://www.amazon.com/Acoustic-Tomography-Cambridge-Monographs-Mechanics/dp/0521115361?SubscriptionId=0JYN1NVW651KCA56C102&tag=techkie-20&linkCode=xm2&camp=2025&creative=165953&creativeASIN=0521115361`.

[74] G. Nolet. Seismic wave propagation and seismic tomography. In *Seismic Tomography*, pages 1–23. Springer Nature, 1987. doi: 10.1007/978-94-009-3899-1_1.

[75] Johan Nuyts, Bruno de Man, Jeffrey A. Fessler, Wojciech Zbijewski, and Freek J. Beekman. Modelling the physics in the iterative reconstruction for transmission computed tomography. *Physics in Medicine and Biology*, 58(12):R63–R96, June 2013. ISSN 0031-9155. doi: 10.1088/0031-9155/58/12/r63. URL `http://dx.doi.org/10.1088/0031-9155/58/12/r63`.

[76] A. Olivo, F. Arfelli, G. Cantatore, R. Longo, R. H. Menk, S. Pani, M. Prest, P. Poropat, L. Rigon, G. Tromba, E. Vallazza, and E. Castelli. An innovative digital imaging set-up allowing a low-dose approach to phase contrast applications in the medical field. *Medical Physics*, 28(8):1610–1619, aug 2001. doi: 10.1118/1.1388219.

[77] David M. Paganin. *Coherent X-Ray Optics*. OXFORD UNIV PR, 2006. ISBN 0198567286. URL `http://www.ebook.de/de/product/4907343/david_m_paganin_coherent_x_ray_optics.html`.

[78] V.Y. Panin, F. Kehren, C. Michel, and M. Casey. Fully 3-d PET reconstruction with system matrix derived from point source measurements. *IEEE Transactions on Medical Imaging*, 25(7):907–921, July 2006. doi: 10.1109/tmi.2006.876171.

[79] S Pedemonte, A Bousse, K Erlandsson, M Modat, S Arridge, B F Hutton, and S Ourselin. GPU accelerated rotation-based emission tomography reconstruction. In *IEEE Nuclear Science Symposuim & Medical Imaging Conference*. Institute of Electrical and Electronics Engineers (IEEE), oct 2010. doi: 10.1109/nssmic.2010.5874272.

[80] Georg Pelzer, Gisela Anton, Florian Horn, Jens Rieger, André Ritter, Johannes Wandner, Thomas Weber, and Thilo Michel. A beam hardening and dispersion correction for x-ray dark-field radiography. *Medical Physics*, 43(6):2774–2779, May 2016. doi: 10.1118/1.4948671.

[81] Adam Petschke and Patrick J. La Rivière. Comparison of photoacoustic image reconstruction algorithms using the channelized hotelling observer. *Journal of Biomedical Optics*, 18(2):026009, Feb. 2013. doi: 10.1117/1.jbo.18.2.026009.

[82] F. Pfeiffer, C. Kottler, O. Bunk, and C. David. Hard x-ray phase tomography with low-brilliance sources. *Physical Review Letters*, 98(10):108105, mar 2007. ISSN 0031-9007. doi: 10.1103/physrevlett.98.108105. URL `http://dx.doi.org/10.1103/physrevlett.98.108105`.

[83] F. Pfeiffer, M. Bech, O. Bunk, P. Kraft, E. F. Eikenberry, Ch. Broennimann, C. Gruenzweig, and C. David. Hard-x-ray dark-field imaging using a grating interferometer. *Nature Materials*, 7(2): 134–137, Jan. 2008. doi: 10.1038/nmat2096.

[84] Franz Pfeiffer, Timm Weitkamp, Oliver Bunk, and Christian David. Phase retrieval and differential phase-contrast imaging with low-brilliance x-ray sources. *Nature Physics*, 2(4):258–261, March 2006. ISSN 1745-2473. doi: 10.1038/nphys265. URL `http://dx.doi.org/10.1038/nphys265`.

[85] M. E. Phelps. Positron emission tomography provides molecular imaging of biological processes. *Proceedings of the National Academy of Sciences*, 97(16):9226–9233, Aug. 2000. doi: 10.1073/pnas.97.16.9226.

[86] J. Radon. Über die Bestimmung von Funktionen durch ihre Integralwerte längs gewisser Mannigfaltigkeiten. *Akad. Wiss.*, 69:262–277, 1917.

[87] Rainer Raupach and Thomas Flohr. Performance evaluation of x-ray differential phase contrast computed tomography (PCT) with respect to medical imaging. *Medical Physics*, 39(8):4761–4774, jul 2012. doi: 10.1118/1.4736529.

[88] Rainer Raupach and Thomas G Flohr. Analytical evaluation of the signal and noise propagation in x-ray differential phase-contrast computed tomography. *Physics in Medicine and Biology*, 56(7): 2219–2244, mar 2011. doi: 10.1088/0031-9155/56/7/020.

[89] Jaroslav Řeháček, Zdeněk Hradil, E. Knill, and A. I. Lvovsky. Diluted maximum-likelihood algorithm for quantum tomography. *Physical Review A*, 75(4), Apr. 2007. doi: 10.1103/physreva.75.042108.

[90] S. O. Rice. Mathematical analysis of random noise. *Bell System Technical Journal*, 24(1):46–156, jan 1945. doi: 10.1002/j.1538-7305.1945.tb00453.x.

[91] S Rit, M Vila Oliva, S Brousmiche, R Labarbe, D Sarrut, and G C Sharp. The reconstruction toolkit (RTK), an open-source cone-beam CT reconstruction toolkit based on the insight toolkit (ITK). *Journal of Physics: Conference Series*, 489:012079, mar 2014. doi: 10.1088/1742-6596/489/1/012079.

[92] André Ritter, Florian Bayer, Jürgen Durst, Karl Gödel, Wilhelm Haas, Thilo Michel, Jens Rieger, Thomas Weber, Lukas Wucherer, and Gisela Anton. Simultaneous maximum-likelihood reconstruction for x-ray grating based phase-contrast tomography avoiding intermediate phase retrieval. *arXiv preprint arXiv:1307.7912*, Jul. 2013.

[93] André Ritter, Peter Bartl, Florian Bayer, Karl C. Gödel, Wilhelm Haas, Thilo Michel, Georg Pelzer, Jens Rieger, Thomas Weber, Andrea Zang, and Gisela Anton. Simulation framework for coherent and incoherent x-ray imaging and its application in talbot-lau dark-field imaging. *Optics Express*, 22(19):23276, Sep. 2014. ISSN 1094-4087. doi: 10.1364/oe.22.023276. URL `http://dx.doi.org/10.1364/oe.22.023276`.

[94] André Ritter, Gisela Anton, and Thomas Weber. Simultaneous maximum-likelihood reconstruction of absorption coefficient, refractive index and dark-field scattering coefficient in x-ray talbot-lau tomography. *PLOS ONE*, 11(10):e0163016, Oct. 2016. doi: 10.1371/journal.pone.0163016. URL `http://dx.doi.org/10.1371/journal.pone.0163016`.

[95] W. C. Roentgen. Ueber eine neue art von strahlen. *Annalen der Physik*, 300(1):1–11, 1898. doi: 10.1002/andp.18983000102.

[96] Holger Scherl, Benjamin Keck, Markus Kowarschik, and Joachim Hornegger. Fast GPU-based CT reconstruction using the common unified device architecture (CUDA). In *2007 IEEE Nuclear Science Symposium Conference Record*. Institute of Electrical and Electronics Engineers (IEEE), 2007. doi: 10.1109/nssmic.2007.4437102.

[97] Florian Schiffers, Sebastian Kaeppler, Georg Pelzer, Andreas Wolf, Andreas Maier, Gisela Anton, and Christian Riess. Polychromatic maximum likelihood reconstruction for talbot-lau x-ray tomography. *Fully3D Proceedings*, 2017.

[98] G. Schulz, T. Weitkamp, I. Zanette, F. Pfeiffer, F. Beckmann, C. David, S. Rutishauser, E. Reznikova, and B. Muller. High-resolution tomographic imaging of a human cerebellum: comparison of absorption and grating-based phase contrast. *Journal of The Royal Society Interface*, 7(53):1665–1676, July 2010. doi: 10.1098/rsif.2010.0281.

[99] M Seifert, S Kaeppler, C Hauke, F Horn, G Pelzer, J Rieger, T Michel, C Riess, and G Anton. Optimisation of image reconstruction for phase-contrast x-ray talbot–lau imaging with regard to mechanical robustness. *Physics in Medicine and Biology*, 61(17):6441–6464, aug 2016. doi: 10.1088/0031-9155/61/17/6441.

[100] Robert L. Siddon. Fast calculation of the exact radiological path for a three-dimensional CT array. *Medical Physics*, 12(2):252–255, mar 1985. doi: 10.1118/1.595715.

[101] Emil Y Sidky, Jakob H Jørgensen, and Xiaochuan Pan. Convex optimization problem prototyping for image reconstruction in computed tomography with the chambolle–pock algorithm. *Physics in Medicine and Biology*, 57(10):3065–3091, Apr. 2012. doi: 10.1088/0031-9155/57/10/3065.

[102] A. Snigirev, I. Snigireva, V. Kohn, S. Kuznetsov, and I. Schelokov. On the possibilities of x-ray phase contrast microimaging by coherent high-energy synchrotron radiation. *Review of Scientific Instruments*, 66(12):5486–5492, Dec. 1995. doi: 10.1063/1.1146073.

[103] Jan Snyman. *Practical Mathematical Optimization*. Springer, 2005. ISBN 038729824X. URL `http://www.ebook.de/de/product/5270182/jan_snyman_practical_mathematical_optimization.html`.

[104] Thomas J. Suleski. Generation of lohmann images from binary-phase talbot array illuminators. *Applied Optics*, 36(20):4686, July 1997. doi: 10.1364/ao.36.004686.

[105] Henry Fox Talbot. Lxxvi. facts relating to optical science. no. iv. *The London and Edinburgh Philosophical Magazine and Journal of Science*, 9(56):401–407, 1836.

[106] A. Tapfer, M. Bech, I. Zanette, P. Symvoulidis, S. Stangl, G. Multhoff, M. Molls, V. Ntziachristos, and F. Pfeiffer. Three-dimensional imaging of whole mouse models: comparing nondestructive x-ray phase-contrast micro-ct with cryotome-based planar epi-illumination imaging. *Journal of Microscopy*, 253(1):24–30, 2014. ISSN 1365-2818. doi: 10.1111/jmi.12094. URL `http://dx.doi.org/10.1111/jmi.12094`.

[107] P. Thibault, M. Dierolf, A. Menzel, O. Bunk, C. David, and F. Pfeiffer. High-resolution scanning x-ray diffraction microscopy. *Science*, 321(5887):379–382, July 2008. doi: 10.1126/science.1158573.

[108] A Thompson, DT Attwood, E Gullikson, M Howells, J Kortright, A Robinson, et al. X-ray data booklet (2009). *URL http://xdb. lbl. gov*, 2009.

[109] Wim van Aarle, Willem Jan Palenstijn, Jan De Beenhouwer, Thomas Altantzis, Sara Bals, K. Joost Batenburg, and Jan Sijbers. The ASTRA toolbox: A platform for advanced algorithm development in electron tomography. *Ultramicroscopy*, 157:35–47, oct 2015. doi: 10.1016/j.ultramic.2015.05.002.

[110] A. Velroyen, A. Yaroshenko, D. Hahn, A. Fehringer, A. Tapfer, M. Mueller, P.B. Noel, B. Pauwels, A. Sasov, A.O. Yildirim, O. Eickelberg, K. Hellbach, S.D. Auweter, F.G. Meinel, M.F. Reiser, M. Bech, and F. Pfeiffer. Grating-based x-ray dark-field computed tomography of living mice. *EBioMedicine*, 2(10):1500–1506, Oct. 2015. doi: 10.1016/j.ebiom.2015.08.014.

[111] Xiaohua Wan, Fa Zhang, Qi Chu, and Zhiyong Liu. High-performance blob-based iterative three-dimensional reconstruction in electron tomography using multi-GPUs. *BMC Bioinformatics*, 13 (Suppl 10):S4, 2012. doi: 10.1186/1471-2105-13-s10-s4.

[112] Zhentian Wang, Nik Hauser, Gad Singer, Mafalda Trippel, Rahel A. Kubik-Huch, Christof W. Schneider, and Marco Stampanoni. Non-invasive classification of microcalcifications with phase-contrast x-ray mammography. *Nature Communications*, 5, May 2014. doi: 10.1038/ncomms4797.

[113] B. E. Warren. *X-Ray Diffraction*. Dover Publications Inc., 1991. ISBN 0486663175. URL `http://www.ebook.de/de/product/3303133/b_e_warren_x_ray_diffraction.html`.

[114] Thomas Weber, Florian Bayer, Wilhelm Haas, Georg Pelzer, Jens Rieger, Andr? Ritter, Lukas Wucherer, Jan Matthias Braun, J?rgen Durst, Thilo Michel, and Gisela Anton. Investigation of the signature of lung tissue in x-ray grating-based phase-contrast imaging.

[115] Thomas Weber, Peter Bartl, Florian Bayer, Juergen Durst, Wilhelm Haas, Thilo Michel, Andre Ritter, and Gisela Anton. Noise in x-ray grating-based phase-contrast imaging. *Medical Physics*, 38 (7):4133, 2011. doi: 10.1118/1.3592935. URL `http://dx.doi.org/10.1118/1.3592935`.

[116] Thomas Weber, Georg Pelzer, Jens Rieger, André Ritter, and Gisela Anton. Report of improved performance in talbot-lau phase-contrast computed tomography. *Medical Physics*, 42(6Part1):2892–2896, may 2015. doi: 10.1118/1.4921022.

[117] Timm Weitkamp, Ana Diaz, Christian David, Franz Pfeiffer, Marco Stampanoni, Peter Cloetens, and Eric Ziegler. X-ray phase imaging with a grating interferometer. *Optics Express*, 13(16):6296, Aug. 2005. doi: 10.1364/opex.13.006296.

[118] Timm Weitkamp, Christian David, Christian Kottler, Oliver Bunk, and Franz Pfeiffer. Tomography with grating interferometers at low-brilliance sources. In Ulrich Bonse, editor, *Developments in X-Ray Tomography V*. SPIE, aug 2006. doi: 10.1117/12.683851.

[119] Wikipedia, the free encyclopedia. The wavelengths and photon energies of x-rays and a few applications of x-rays., 2013. [Online; accessed Marc 07, 2017 at `https://en.wikipedia.org/wiki/X-ray#/media/File:X-ray_applications.svg`].

[120] Wikipedia, the free encyclopedia. Bremsstrahlung produced by a high-energy electron deflected in the electric field of an atomic nucleus., 2017. [Online; accessed Marc 09, 2017 at `https://commons.wikimedia.org/wiki/File:Bremsstrahlung.svg`].

[121] S. W. Wilkins, T. E. Gureyev, D. Gao, A. Pogany, and A. W. Stevenson. Phase-contrast imaging using polychromatic hard x-rays. *Nature*, 384(6607):335–338, Nov. 1996. doi: 10.1038/384335a0.

[122] Martin J. Willemink, Pim A. de Jong, Tim Leiner, Linda M. de Heer, Rutger A. J. Nievelstein, Ricardo P. J. Budde, and Arnold M. R. Schilham. Iterative reconstruction techniques for computed tomography part 1: Technical principles. *European Radiology*, 23(6):1623–1631, Jan. 2013. doi: 10.1007/s00330-012-2765-y.

[123] Andreas Wolf. Untersuchungen zu einer iterativen ct-rekonstruktion in der gitterbasierten roentgenbildgebung. Master's thesis, FAU Erlangen-Nuremberg, 2016. URL `http://www.ecap.physik.uni-erlangen.de/publications/pub/2016_Wolf_Master.pdf`.

[124] W. Yashiro, Y. Terui, K. Kawabata, and A. Momose. On the origin of visibility contrast in x-ray talbot interferometry. *Optics Express*, 18(16):16890–16901, July 2010. ISSN 1094-4087. doi: 10.1364/oe.18.016890. URL `http://dx.doi.org/10.1364/oe.18.016890`.

[125] Wataru Yashiro and Atsushi Momose. Effects of unresolvable edges in grating-based x-ray differential phase imaging. *Optics Express*, 23(7):9233, apr 2015. doi: 10.1364/oe.23.009233.

[126] Wataru Yashiro, Patrik Vagovič, and Atsushi Momose. Effect of beam hardening on a visibility-contrast image obtained by x-ray grating interferometry. *Optics Express*, 23(18):23462, Aug. 2015. doi: 10.1364/oe.23.023462. URL `https://doi.org/10.1364%2Foe.23.023462`.

[127] I Zanette, M Bech, A Rack, G Le Duc, P Tafforeau, C David, J Mohr, F Pfeiffer, and T Weitkamp. Trimodal low-dose x-ray tomography. *Proceedings of the National Academy of Sciences*, 109(26): 10199–10204, 2012.

[128] Andrea Zang. Ueber die erkennbarkeit fein verteilten mikrokalks in der interferometrischen mammographie. Master's thesis, FAU Erlangen-Nuremberg, 2013. URL `http://www.ecap.physik.uni-erlangen.de/publications/pub/2016_Wolf_Master.pdf`.

[129] Gengsheng Lawrence Zeng. *Medical image reconstruction: A conceptual tutorial / Gengsheng Lawrence Zeng*. Springer, 2010. ISBN 978-3642053672. doi: 10.1007/978-3-642-05368-9. URL `http://dx.doi.org/10.1007/978-3-642-05368-9`.

[130] G.L. Zeng and G.T. Gullberg. Unmatched projector/backprojector pairs in an iterative reconstruction algorithm. *IEEE Transactions on Medical Imaging*, 19(5):548–555, may 2000. doi: 10.1109/42.870265.

[131] Shu-Ang Zhou and Anders Brahme. Development of phase-contrast x-ray imaging techniques and potential medical applications. *Physica Medica*, 24(3):129–148, Sep. 2008. doi: 10.1016/j.ejmp.2008.05.006.

[132] Wei Zhou, Keivan Majidi, and Jovan G. Brankov. Analyzer-based phase-contrast imaging system using a micro focus x-ray source. *Review of Scientific Instruments*, 85(8):085114, aug 2014. doi: 10.1063/1.4890281.